Politecnico di Torino

Politecnico di Torino

Master's Degree Course in Materials Engineering
A.y. 2020/2021
Master's Degree Session of October 2021

Joining of porous alloys by glass ceramics for energy applications

Supervisors:
Prof. Federico Smeacetto
Prof.sa Milena Salvo
Dr. Fabiana D'Isanto
Prof. Sebastian Molin

Candidate:
Umberto Dal Col

Table of Contents

Riassunto

1 Introduzione

Un vetro ceramico è un materiale ottenuto da vetri inorganici che hanno avuto tempo di formare dei cristalli, sono composti da una matrice vetrosa e una o più fasi cristalline e si collocano tra le categorie di vetri inorganici e i ceramici[1].
Un vetro è composto da tre componenti:

- Formatori di reticolo: costituiscono l'ossatura del reticolo
- Modificatori di reticolo: non sono in grado di vetrificare ma interrompono il reticolo. Si differenziano dai formatori per la minor forza di legame.
- Intermedi: non formano reticolo ma in quantità limitate possono farne parte[2].
- Additivi: ad esempio Y_2O_3, ZnO, PbO, TiO_2, ZrO_2.

Un vetro è un materiale amorfo che non ha potuto cristallizzare in tempo prima di irrigidirsi, non ha ordine a lungo raggio e alcuna periodicità. Non possiede una temperatura di fusione definita, ma piuttosto rammollisce in intervallo più o meno esteso di temperatura, identificato come transizione vetrosa (Tg). Lo spettro a raggi x è caratterizzato da una banda bassa e allargata invece di picchi definiti dei materiali cristallini[3]. Due teorie descrivono la formazione dei vetri, la prima è strutturale ovvero alcuni costituenti formano reticoli disordinati con energia simile a quella dei reticoli ordinati. La seconda è la teoria di Zachariesen secondo cui il vetro si forma quando la velocità di raffreddamento è superiore a quella di cristallizzazione per sostanza in questione.
Al fine di ottenere un vetroceramico è fondamentale riscaldare ad una temperatura adeguata per un tempo sufficiente affinché avvenga la nucleazione e la crescita delle specie cristalline. Inoltre, la velocità della cristallizzazione deve essere sufficientemente elevata[3].
I due fattori principali su cui si basa lo sviluppo di una vetroceramica sono la composizione e la microstruttura. La composizione permette la nucleazione interna e favorisce la lavorabilità del vetro. La presenza della fase cristallina è in grado di impartire proprietà uniche e combinazioni delle stesse non riscontrabili in altre classi di materiali. Tra queste si annoverano tenacità elevate, proprietà elettriche, magnetiche e perfino diversa biocompatibilità tra matrice e fase cristallina. Le stesse proprietà ottiche sono estremamente variabili[1].
Un modo per promuovere la ceramizzazione di un vetro si basa sulla sinterizzazione e cristallizzazione del vetro finemente macinato. Questa seconda modalità è la tecnica con cui si ottengono i vetroceramici trattati nel presente elaborato. Si tratta di un approccio vantaggioso: la cristallizzazione ha luogo nel sito di maggior energia, ossia sulle imperfezioni superficiali delle polveri. Le tecniche utilizzabili sono lo slip-casting, la pressatura, l'estrusione o tape-casting.
Per quanto riguarda l'utilizzo commerciale, il vetroceramico da fritta è stato utilizzato in un primo momento come saldatura per sigillare le lampadine dei televisori e successivamente per produrre substrati multistrato co-sinterizzati di componenti elettronici, biomateriali e impianti dentali.
Altre applicazioni delle vetroceramiche si riscontrano nell'ambito della produzione di energia. Una di queste, approfondita di seguito, riguarda le celle a combustibile ad ossidi solidi (SOFC) in cui i vetroceramici fungono da sigillanti tra i vari componenti del dispositivo[1].

1.1 Celle a combustibile, definizione e funzionamento base

Oggigiorno le celle a combustibile sono una potenziale soluzione per i motori a combustione interna che così risultano essere più puliti, silenziosi, efficienti e durevoli[4].
Una cella a combustibile è un reattore che converte, attraverso una reazione spontanea di ossidoriduzione, energia chimica in energia elettrica e calore [5]. I componenti principali di una cella a combustibile sono: elettrolita, catodo e anodo. Una rappresentazione schematica di una singola cella a combustibile è mostrata nella Figura 1.

1.2 Caratteristiche di funzionamento

Le prestazioni della cella a combustibile si basano sulla tensione di cella, parametro che è funzione della densità di corrente o della curva di polarizzazione.
La tensione è espressa con la seguente equazione:

$$E = E_{eq} - E_L - \eta_{act} - \eta_{iR} - \eta_{diff}$$

dove E_{eq} rappresenta il potenziale all'equilibrio, E_L la caduta di tensione dovuta a perdite nell'elettrolita (particolarmente rilevanti in celle ad alta temperatura). η_{act} indica il sovrapotenziale per attivare reazioni più lente che, per celle ad idrogeno, si riscontrano tutte al catodo, η_{iR} le perdite ohmiche e η_{diff} il potenziare necessario a superare gli ostacoli dovuti alla diffusione ed è principalmente funzione della geometria.

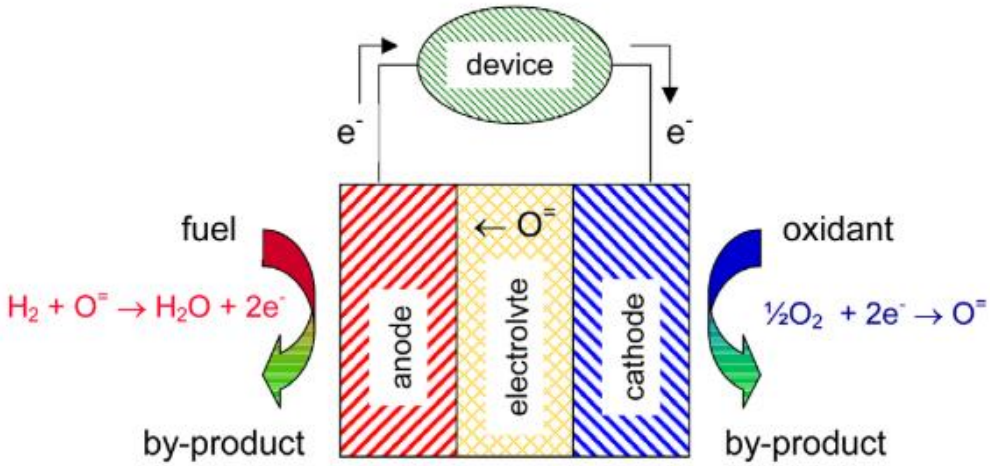

Figura 1: schema di una singola cella combustibile [5].

L'efficienza è direttamente proporzionale al sovrapotenziale applicato, ma raggiunge il massimo a basse densità di corrente. Efficienze elevate con alte densità di corrente sono invece ottenibili quando l'elettrocatalisi al catodo avviene più velocemente come succede su substrati porosi e la diffusione di specie gassose ed elettroni è lenta[5]. Più celle insieme costituiscono una stack, e permettono di aumentare la tensione generata[4].

1.3 Tipologie

Le celle a combustibile possono essere di diversi tipi, i principali sono elencati di seguito.

1- Le PEMFC sono utilizzate prevalentemente per i sistemi di trasporto, ma anche come fonte di energia residenziale e per i dispositivi portatili. I vantaggi principali di questi sistemi sono: elevata densità di potenza, avviamento molto rapido che lo rende adatto al settore automobilistico, assenza di corrosione e bassa temperatura di esercizio [4].
2- Le celle a combustibile ad acido fosforico (PAFC) hanno lo stesso funzionamento delle PEMFC, ma tollerano una maggiore concentrazione di monossido di carbonio e funzionano a 200°C. Gli svantaggi di tali celle riguardano l'alto costo, le basse densità di corrente, i fenomeni di corrosione e i tempi di avviamento più lunghi [4].
3- Le celle alcaline funzionano in modo simile alle PEMFC e alle PAFC. Sono migliori delle prime in termini di cinetica, ma non sono utilizzabili se è presente anidride carbonica [4].
4- Le celle a combustibile a carbonato fuso (MCFC) utilizzano Ni come catalizzato e, in virtù delle temperature operative di circa 650°C possono effettuare il reforming interno. Lo ione CO_3^{2-} è direttamente coinvolto nella reazione di ossidazione dell'idrogeno.

5- Le SOFC offrono efficienze maggiore rispetto ai motori a combustione interna o ai sistemi di generazione di energia più convenzionali. Tuttavia, l'utilizzo di massa della tecnologia è limitato da alcuni fattori: le elevate temperature di esercizio riducono la durata delle celle, accelerando il degrado e la corrosione. Inoltre, rappresentano un ostacolo per quanto riguarda la sicurezza, la miniaturizzazione e la riduzione dei costi [4].

1.4 Materiali costitutivi e classificazione delle SOFC

Analizzando in dettaglio le SOFC, queste sono composte da: elettrolita, catodo, anodo, interconnettore e sigillante.

-ELETTROLITA

L'elettrolita ha tra le proprie caratteristiche un'elevata conducibilità ionica, stabilità meccanica ed una notevole resistività elettrica. Richiede inoltre resistenza in ambienti ossidanti e riducenti [10]. Si tratta di materiali ceramici con strutture quali fluorite, perovskite, brownmillerite e apatite[6]. Uno degli elettroliti più utilizzati è la zirconia, ma uno dei suoi limiti è dato dal costo elevato e dalla difficoltà di sinterizzarizzazione con alta densità. Anche la ceria è un materiale per elettroliti molto usato, in quanto permette un'ottima conduttività e bassa energia di attivazione[7].

-CATODO

Il catodo è caratterizzato da un'alta conducibilità elettronica, compatibilità chimica e termomeccanica con l'elettrolita e l'interconnettore, buona stabilità in atmosfera ossidante; deve essere caratterizzato da un valore di coefficiente didilatazione termica vicino a quello degli altri componenti e porosità sufficiente a permettere un efficace trasporto di ossigeno. Un requisito fondamentale è l'alta attività catalitica per la riduzione dell'ossigeno [10]. La perovskite $La_{1-x}Sr_xCoO_{3-\delta}$ (LSC) è stata la prima ad essere utilizzata in una cella a combustibile [8]. La peculiarità data dal trasporto simultaneo di ioni ed elettroni comporta che le perovskiti siano un materiale adatto per le SOFC anche per applicazioni a temperature basse[9].

-ANODO

L'anodo richiede un'elevata porosità, notevole conducibilità elettronica, elevata attività catalitica e compatibilità con i componenti in termini di dilatazione termica. Nella prima generazione di SOFC, il platino, la grafite, gli ossidi di ferro o altri metalli di transizione erano gli elementi preferiti, ma presentavano problemi di degradazione, corrosione e diverso coefficiente di espansione termica (CET) con l'elettrolita. Ni/YSZ è ormai da tempo il materiale prediletto in quanto presenta una buona conduttività mista ionico/elettronico. Nonostante ciò, esistono alcuni inconvenienti: uno di questi è dato dal fatto che la corrente tende ad agglomerare, diminuendo così l'efficienza delle reazioni[10], [11]. Un ulteriore problema deriva dall'avvelenamento da zolfo che è possibile superare tramite l'utilizzo di perovskiti come $Sr_{1-x}La_xTiO_3$ (LST), $SrTiO_3$ drogata con yttria, $La_{1-x}Sr_xVO_3$ (LSV), $La_{1-x}Sr_xCr_{1-y}Mn_yO_3$ (LSCM) [12]–[15]. Combustibili idrocarburici come metano ed etano sono ossidabili grazie alla ceria[10].

-INTERCONNETTORE

Gli interconnettori agiscono come barriera fisica di protezione del catodo dall'ambiente riducente della cella, godono di eccellente conducibilità elettrica in condizioni operative e sono caratterizzati da stabilità dimensionale, microstrutturale, chimica. È fondamentale che abbiamo coefficiente di dilatazione simile ai componenti con cui è in contatto. Gli interconnettori possono essere suddivisi in due classi: ceramici e metallici. I materiali a base di perovskite $LaCrO_3$ sono i materiali ceramici di interconnessione più utilizzati[16].

Gli interconnettori metallici hanno il difetto di essere soggetti ad ossidazione e la crescita continua dello strato di ossido determina l'aumento della resistività nel tempo. Pertanto, è necessario trovare un equilibrio tra conduttività e resistenza alla corrosione. Gli interconnettori metallici sono

solitamente realizzati con acciai inossidabili ferritici; risultano facili da lavorare ed il costo è relativamente basso. Durante la vita operativa sono soggetti alla vaporizzazione del cromo, che provoca l'avvelenamento del catodo, la riduzione del potenziale della cella e del suo funzionamento[17]. Un sistema di interconnettore-rivestimento adeguato può rappresentare una possibile soluzione. A tal proposito, gli studi si sono concentrati su rivestimento con spinelli di tipo $(Mn, Co)_3O_4$ [18].

-SIGILLANTI
Il sigillante ha le seguenti funzioni e requisiti: tenere insieme i diversi componenti della cella, evitare la fuoriuscita o la miscelazione di ossidante o combustibile nella cella, il coefficiente di dilatazione termica deve essere simile a quello degli altri componenti, deve resistere a temperature operative per lunghi periodi di tempo (fino a 10000h) ed essere stabile per diversi valori di pressione parziale di O_2. È necessaria inoltre ottima resistenza ai cicli termici e la non reattività con i componenti con cui è in contatto[19]. Si dividono in 2 tipologie: a compressione e rigidi. I primi prevedono che il materiale di isolamento sia compresso tra due superfici, rendendole in grado di scorrere l'una rispetto all'altra senza perdere l'ermeticità[20]. Le giunzioni a compressione sono ulteriormente suddivisibili 2 sottotipi: metalliche e a base mica[21]. Le giunzioni di tipo rigido sono più economiche di quelle a compressione, raggiungono l'ermeticità attraverso il legame chimico con la superficie. Appartengono a questa categoria i vetroceramici e le leghe brasanti[22]. Per i vetroceramici il legame chimico è ottenuto attraverso la formazione di una zona di transizione, in cui i legami metallici vengono progressivamente sostituiti da quelli ionico-covalenti; il legame chimico forte si ottiene una volta raggiunta la saturazione della superficie con ossidi metallici. In caso di superficie preossidata, lo strato di ossido si dissolve nella matrice vetrosa all'interfaccia. Per superfici non ossidate l'ossido è la conseguenza di reazioni redox tra il metallo e il vetro, seguita poi dalla dissoluzione dell'ossido nel vetro[19].

Le SOFC possono essere classificate in base a 2 criteri: la geometria e l'elemento che conferisce integrità meccanica. Due diverse geometrie sono possibili: planari e tubolari. Le prime sono attualmente quelle che hanno subito maggiore sviluppo, sono più facili da produrre e più efficienti di quelle tubolari[23]. Queste ultime garantiscono migliore tenuta ai gas ma minor potenza per percorsi di corrente elettrica molto lunghi. Alcune celle inoltre posso operare in maniera inversa, ovvero utilizzare l'energia elettrica in ingresso per produrre idrogeno da acqua. Assumono il nome di elettrolizzatori a ossidi solidi (SOEC) e possono essere prodotte con le attuali tecnologie SOFC[24]. Elettrolita, catodo, anodo, interconnettore sono i componenti che, se utilizzati in maggior spessore possono supportare la cella. Le celle elettrolita-supportate sono quelle con maggior resistenza meccanica. Ma come nel caso di catodo e anodo si tratta di componenti ceramici, necessitano di temperature elevate per avere sufficiente conducibilità,comportano maggiori costi e sono più fragili. L'uso di leghe porose come elementi strutturali permette di ridurre le temperature di esercizio, i costi e aumentare la robustezza delle celle. Il supporto poroso aumenta la complessità e aggiunge parametri di flusso dei gas alle caratteristiche di funzionamento delle celle, dette metallo supportate (MSOC).

1.5 MSOC

Le celle metallo-supportate sono tra le tecnologie più promettenti per sistemi ausiliari (APU) in aerei, treni e camion pesanti o veicoli a trazione elettrica in generale, secondo quanto sostenuto dal dipartimento dell'energia statunitense (U.S. DOE). Queste celle sono più resistenti agli shock e alle vibrazioni, conducibilità e stabilità migliori, accensioni più rapide e minor costo dei materiali. Uno dei principali limiti è la vita utile, ritenuta ancora insufficiente ad impeghi di larga scala[25].

La rapida variazione di temperatura tra accensione e spegnimento è in realtà un beneficio. Con riscaldamenti e raffreddamenti rapidi, il supporto metallico (con CET maggiore) annulla la differenza di espansione per il creep a cui è sottoposto. Nel raffreddamento l'elettrolita è in compressione, e permane in questo stato se raffreddato e riscaldato abbastanza in fretta fino alle temperature operative. Cicli lenti invece non fanno altro che indurre uno stato di tensione neutra a temperature lontane da quelle di esercizio [26].

1.6 Supporti

I supporti sono realizzati in acciaio inox per le stesse ragioni che li rende adatti all'uso come interconnettori. Il contenuto di cromo varia dal 10,5 al 26% massimo per evitare la formazione di fare sigma infragilente. Altri elementi aggiunzioni sono Al, Ti, Ni, Mo e Si. Come per gli interconnettori la rottura dello strato di ossido va evitata a tutti i costi. La crescita dell'ossido è direttamente proporzionale alla temperatura, abbassandola è possibile allungare considerevolmente la vita utile del componente. Con temperature di 650-700°C un supporto può operare per 50000h prima che l'ossido diventi così spesso da fratturarsi [26].

1.7 Elettroliti

LSGM è uno degli elettroliti più usati, il suo impiego operativo è stato spinto fino a 400°C ma tende a reagire con vapori di cromo. L'ossido di gadolinio e cerio (CGO) permette di ridurre le temperature fino a 600°C, sinterizza fino a massima densità e non subisce ritiro. Un altro materiale di rilevanza è la zirconia stabilizzata con yttria (YSZ), che si è dimostrata un materiale durevole per le applicazioni MSOC; tuttavia per fare il reforming è necessaria una temperatura di almeno 650°C. Inoltre deve essere presenti in spessori rilevanti (30-70µm) affinché sia impenetrabile ai gas. Temperature troppo elevate ne comportano l'ossidazione e il fallimento prematuro. È possibile co-sinterizzarla su altri elementi della cella come sistema per ridurre i costi produttivi. Con la deposizione umida è possibile ridurre lo spessore necessario a soli 10-20µm e per temperature di 650-700°C esibisce resistenze sufficientemente basse[26].

1.8 Catodo

Sono state inizialmente usate LSM e $Ln_{1-x}Sr_xCo_{1-y}Fe_yO_{3-\delta}$ (LSCF) depositate per plasma-spray, ma alcuni problemi ne ostacolano l'uso di successo. Il primo decompone in atmosfere riducenti, il secondo sinterizza a temperature tali da indurre forte vaporizzazione del cromo. Una possibile alternativa è sinterizzare catodi di YSZ porosa su altri elementi della cella, quali il supporto o elettrolita, e solo successivamente introdurre precursori del catalizzatore tramite infiltrazione, senza indurre ulteriori stress termici. LSM infiltrata si è dimostrata molto più resiliente all'avvelenamento da cromo[26].

1.9 Anodo

Inizialmente sono stati usati anodi convenzionali in Ni-YSZ, ma con la temperatura si assisteva all'ingrossamento del grano metallico, diminuendo la conducibilità. Anche la diffusione di Fe e Cr ne porta ad una diminuzione e formano ossidi isolanti. Una possibile soluzione deriva dall'impiego di barriere alla diffusione tra anodo e supporto [26].
Come per il catodo è possibile infiltrare la YSZ con il catalizzatore, il nickel è soggetto a ingrossamento del grano e calo rapido delle performance. La ceria dopata con samario (SDC) si è

dimostrata più stabile ma meno conduttiva. L'aggiunta di rame ha la capacità di aumentare la conducibilità della SDC.

1.10 Sigillanti

Sono utilizzabili un'ampia gamma di tipologie di sigillanti, data la natura metallica del supporto. Sono stati usati con successo leghe brasanti, saldature, crimpature, guarnizioni o leghe attive. Supporti porosi con bordi solidi sono stati usati dalla Ceres Power per le proprie MSOC e sigillate con metodi convenzionali quali saldatura laser o guarnizioni a compressione. Queste tecniche di giunzione si sono rivelate resistenti al ciclaggio termico senza mostrare fuoriuscite di gas. Le paste ceramiche sono state usate per la produzioni di celle metallo-supportate unicamente a scopo dimostrativo [26].

1.11 Sviluppi recenti

Negli ultimi anni la ricerca ha proseguito, ma solo la Ceres Power è riuscita a produrre una tipologia di MSOC con prontezza tecnologica (TRL) di livello 8. Anche la ricerca sui supporti metallici non si è fermata; leghe di Ni-Fe sono state prodotte per riduzione in-situ all'anodo rendendole promettenti per celle di dimensioni ridotte. Il principale limite è dato dalla bassa resistenza a cicli redox. Ulteriori test si sono concentrati su leghe quali NI-Al e Ni-Mo. Gli acciai ferritici 430L sono ancora quelli più convenienti, in termini di costo, prestazioni e compatibilità con gli altri componenti della cella. Sono soggetti ad impoverimento di cromo, di conseguenza le barriere alla diffusione sono ancora un requisito fondamentale e le tecnologie produttive attuali difficilmente si adattano alla produzione su scala.
Altre innovazioni giungono dalle configurazioni; sono state infatti testate MSOC simmetriche, che usano il supporto metallico poroso su entrambi gli elettrodi, questi ultimi sono separati da un sottile strato di elettrolita. I primi sono realizzati da YSZ porosa infiltrata da LSC o SDCN e l'elettrolita è in YSZ. La cella ha dimostrato una stabilità considerevole, le principali cause di fallimento sono imputabili all'avvelenamento da Cr e ingrossamento del grano. Il contatto indiretto tra supporto e catalizzatore ne ha accelerato la degradazione rispetto alle configurazioni convenzionali.
Nel 2020, uno studio pilota ha concentrato lo sviluppo di MSOC sull'ottimizzazione dei materiali più convenzionali, prima singolarmente poi insieme. La cella risultante è in grado di operare a 650-800°C e generare una potenza di 3,13 Wcm^{-2}, 0,7 V al 800°C e una densità di corrente di 2,8 Acm^{-2} a 650°C, stabilendo il record di potenza delle MSOC.
La cella è cosi composta: catodo in LSC sinterizzato in-situ, elettrolita in YSZ spesso 2µm e anodo da 22µm in Ni/GDC. La performance di quest'ultimo è stata aumentata da strati intermedi di Ni/YSZ tra l'anodo e il supporto. Questi strati sono caratterizzati da un gradiente di porosità, in modo da rendere la transizione tra il supporto e l'anodo il più graduale possibile. Il supporto è costituito da una lega Fe-Cr da 300µm. Test preliminari in condizioni di laboratorio hanno messo in funzione la cella per 1000h con una miscela di alimentazione 50/50 idrogeno e vapore dimostrando di essere promettenti sulla stabilità a lungo termine.
L'attrattiva principale è far lavorare le celle a 600°C, conseguentemente rinunciando alla possibilità di fare reforming e abbassando l'efficienza, e anche l'attivazione del catodo può risentirne. Sistemi di sicurezza quali barriere alla diffusione, e un contenuto di cromo maggiore per lavoro ad alta temperatura possono aumentare i costi, rendendo necessario un bilanciamento.

2 Giunzione di leghe porose: stato dell'arte

Attualmente i vetroceramici sono stati usati come giunzioni su supporti porosi di celle metallo-supportate solo per quelle realizzate da Udomsilp et al. [25] precedentemente discusse. Non sono stati resi noti i dettagli e non esistono altri esempi in letteratura. Il vetroceramico usato è analizzato nel lavoro di Gross et al. [27], si tratta di un vetro a base $BaO-CaO-SiO_2$ con granulometria media 10-13µm caricato con polveri di ZrO_2 monoclina da 15µm di taglia. Dallo studio è emerso che la presenza della zirconia sopprime la cristallizzazione del vetro già per contenuti del 10%. La transizione vetrosa si sposta a temperature più elevate e si riduce l'espansione termica (la massima riduzione si ottiene per il 20% di ZrO_2). Lo spessore delle giunzioni realizzate con la pasta di vetro caricata è direttamente proporzionale al contenuto di zirconia. I cristalli del vetroceramico crescono a partire dalle particelle ceramiche solo per lunghi trattamenti di cristallizzazione. Tutte le giunzioni si sono dimostrate impermeabili ai gas, indipendente dalla quantità di zirconia nella matrice vetrosa. La bassa velocità di cristallizzazione conseguente, può potenzialmente permettere al vetroceramico di riparare autonomamente eventuali danni o fratture nella propria struttura[27].

3 Procedure sperimentali

3.1 Materiali

Le due leghe sono di composizione simile. La prima è un acciaio inox ferritico Fe22Cr già usata in precedenti lavori di Koszelow et al. È un prodotto sperimentale denominato MW2 prodotto dalla Hoganas AB, la composizione è indicata in Tabella 1. Si presenta sotto forma di lamierino poroso spesso 0,4 mm ottenuto tramite processo di tape-casting con sinterizzazione a 1250°C in atmosfera di puro idrogeno. Il volume libero si attesta al 30% circa di quello totale [28].
La seconda lega è un lamierino denso di Crofer 22 APU spesso 0,3 mm, la composizione è data in Tabella 2.

Tabella 1: composizione della lega porosa MW2 (%wt)) [28].

Fe	**Cr**	**Mn**	**Si**	**Ni, Cu, Mo**
Bal.	22	0,23	0,08	<0,03

Tabella 2: composizione del Crofer 22 APU (%wt)[29].

Fe	**Cr**	**C**	**Mn**	**Si**	**Cu**	**Al**	**S**	**P**	**Ti**	**La**
Bal.	20-24	0,03	0,3-0,8	0,50	0,50	0,50	0,02	0,05	0,03-0,20	0,04-0,20

Per la realizzazione delle giunzioni sono stati usati due tipi di vetro: il primo è a base sodio denominato V10, il secondo GC2 e contiene bario. Sono stati ottenuti per fusione in crogiolo di Pt-Rh a 1600°C e 1500°C rispettivamente, per 1 ora [30]. La colata è avvenuta su piastra di ottone e lasciata raffreddare. I vetri sono stati poi macinati in macinatore a sfera di zirconia e la polvere ottenuta è stata setacciata per selezionare una dimensione inferiore a 25µm. Quest'ultime polveri sono state utilizzate per produrre uno slurry di vetro da depositare sui substrati.

3.2 Metodi ed attrezzature

Le giunzioni sono state realizzate a partire da lamierini quadrati di MW2 e Crofer di dimensioni approssimative 10x10 mm^2.
La pasta di vetro consisteva di uno slurry di etanolo e polvere di vetro (30-70% rispettivamente) depositato manualmente sul substrato inferiore con una spatola. Successivamente è stato aggiunto il

secondo substrato in modo da formare una struttura a sandwich. Qualora la configurazione lo prevedeva è stato posizionato un peso sulla giunzione di circa 15g. Sono state prodotte e caratterizzate morfologicamente diverse configurazioni, e la migliore è risultata quella ottenua con Crofer preossidato su MW2, con peso di 15g sulla giunzione.
Per l'osservazione al SEM i campioni sono stai lucidati fino a carte da 4000grit, parallelamente allo spessore. Il SEM usato è un JCM-6000Plus, Jeol (Japan) e unitamente a micrografie, sono state effettuate analisi quantitative con EDS.
La microscopia riscaldante è stata utilizzata per avere informazioni sul comportamento del vetro in termini di sinterizzazione, in funzione della temperatura. Un pellet di polvere di vetro (di diametro e altezza 3mm) è stato posizionato su un substrato (Crofer e MW2) di 8x10 mm^2 e sottoposto a trattamento termico da temperatura ambiente fino al fusione del vetro, rilevato automaticamente dallo strumento. Un campione di giunzione GC2 è stato anche sottoposto a CT scan per visualizzare la struttura interna al campione. Il macchinario utilizzato è stato costruito da IKTS Fraunhofer con le seguenti caratteristiche: massima tensione di lavoro 300kV, detector da 400x400 mm^2 e risoluzione di 9 µm (ridotte a 5 in condizioni ottimali).

Le giunzioni GC2 sono state sottoposte ad invecchiamento termico (700°C per 500h) con lo scopo di sottoporle a test meccanici di trazione, così da confrontarle con giunzioni non invecchiate. Questi trattamenti sono stai effettuati alla Hertfordshire University, Hatfield UK.
Le giunzioni sono state testate con una prova di trazione ASTM C633-01 modificata, sono stati incollati a dei cilindri di afferraggio in acciaio tramite Araldite® 2015, in modo analogo a quanto fatto da *Baino et al*.[31]. La resistenza della resina si attesta a 22MPa, come dichiarato dal produttore[32], e si è rivelata più che sufficiente per lo scopo. Le giunzioni sono state interposte ai 2 afferraggi per reticolare sono stati inseriti in stufa a 85°C per 1 ora. La velocità di deformazione durante la prova di trazione è stata di 0,5 mm/min. Le superfici di frattura sono state poi metallizzate e osservate al SEM.

4 Risultati e discussioni

4.1 Giunzioni con vetro V10

Il primo campione è stato realizzato usando l'MW2 sopra al lamierino in Crofer ricoperto della pasta di vetro non setacciato, sopra la giunzione è stato poi posizionato un peso di allumina. Il trattamento termico utilizzato è stato di 850°C per 1h con velocità di riscaldamento di 5°C/min. Dal momento che i substrati di lega porosa non erano ancora stati raddrizzati, la deformazione degli stessi non ha permesso un contatto efficiente con il vetroceramico, evidenziando aree piuttosto estese di distacco. L'interfaccia tra Crofer e il vetroceramico era stata lievemente distaccata e riempita di particelle di abrasivo. Lo strato vetro ceramico era compatto, la porosità ben distribuita e contenuta in dimensione, di forma irregolare. Anche l'interfaccia tra il vetro e il la lega porosa presentava grandi zone di mancata adesione in cui particelle estranee si sono accumulate.

Per studiare meglio e capire l'affinità del vetroceramico sui diversi substrati sono stati realizzati dei semplici rivestimenti su tre diversi substrati: Crofer preossidato, Crofer non modificato e lega porosa (rispettivamente campioni 2, 3 e 4) col medesimo trattamento del campione 1. Da questo punto in poi il vetro è stato setacciato a 25 µm. Tutti i campioni hanno riscontrato ritiro del vetro lasciando quindi una parte dei substrati completamente privi di rivestimento. Questo fenomeno è stato riscontrato in misura minore sulla lega MW2, è probabile che questo effetto sia dovuto al fatto che non ci fosse un lamierino superiore che forzasse il vetro ad aderire.
Il vetro ceramico ha formato in ogni campione un'ottima interfaccia e la preossidazione ha dato risultati leggermente migliori rispetto alla lega non ossidata.

Il vetro ceramico V10 ha una transizione vetrosa a 610°C la principale fase cristallina è l'Augite, un monosilicato di magnesio e alluminio che inizia a formarsi 800°C, e una massima velocità di cristallizzazione a 840°C.
Sui precedenti tre substrati è stata effettuata un'analisi al microscopio riscaldante per quantificare il ritiro al variare del substrato. Si è evidenziata una maggior tendenza del vetro a cristallizzare sul Crofer preossidato, validata dal minor angolo di contatto tra tutti i campioni. Per quanto riguarda l'MW2 vi è una forte riduzione dell'area della sezione, molto probabilmente dovuta all'intrusione del vetro nei pori che ha provocato un incurvamento della lega verso la massa di vetroceramico.
Due nuovi campioni, 5 e 6, sono stati realizzati in modo analogo il campione uno, la differenza tra i due risiede nella preossidazione del Crofer nel campione 5. In questo caso la miglior interfaccia è stata quella tra vetro ceramico e il Crofer mentre l'interfaccia con la lega porosa si mostrava, per la maggior parte della giunzione, distaccata. Nel vetro ceramico non sono state riscontrate differenze dal campione 1. Il campione 6 presentava invece una situazione opposta; l'interfaccia migliore era quella in contatto con l'MW2, con i maggiori pori infiltrati dal materiale di giunzione, mentre l'interfaccia con il Crofer risultava lievemente distaccata lungo tutta la sezione osservata e occupata da particelle di abrasivo.
Il campione 7 è stato realizzato preossidando entrambi i substrati metallici e posizionando la lega porosa in posizione superiore. Nel campione 8 solo il Crofer è stato preossidato e costituiva lo strato superiore della giunzione. Per questi due campioni anche il carico è stato modificato, portandolo a 15 g/cm^2 (che verrà usato per tutte le successive giunzioni) con l'uso di un blocco di Crofer. Inoltre, da questo momento in poi tutti i lamierini di MW2 utilizzati sono stati raddrizzati. Per entrambe le giunzioni l'interfaccia con la lega porosa ha dato risultato soddisfacente solo in alcuni punti; in corrispondenza dei pori più grandi interfaccia non era presente. la mancata adesione più significativa è stata riscontrata all'estremità della giunzione n° 7, è possibile ipotizzare che sia dovuto al rilascio di tensioni residue nella lega, è da escludere inoltre che sia dovuta all'occlusione dei pori da parte dello strato di ossido durante la preossidazione[28]. Dove il vetroceramico ha aderito ad entrambi le leghe è possibile notare la presenza di pori più grandi del normale, probabilmente dovuti al materiale mancante. Il campione numero otto è quello che ha riscontrato la migliore adesione ma è stata anche notata la presenza di una porosità e dimensione media maggiore proprio a metà dello strato vetroceramico. Il campione 8 è visibile in *Figura 2*.
I lavori successivi si sono concentrati sulla rimozione della porosità a metà giunzione, una delle strategie tentate è stata quella di formare giunzioni con la lega porosa già pre-rivestita (trattata a 850°C per 1h in aria).
Il campione n° 9 è stato quindi prodotto ponendo l'MW2 già rivestito sopra il Crofer preossidato e rivestito di pasta di vetro, e in seguito giuntato in forno. Mentre l'interfaccia con l'MW2 è stata soddisfacente il vetro ceramico nel posto durante la produzione della giunzione ha avuto un'adesione preferenziale al vetro ceramico del rivestimento, lasciando porzioni estese di Crofer non rivestite. Inoltre l'adesione si è dimostrata essere inferiore rispetto ai campioni precedenti.

A questo punto è stata modificata la temperatura massima di trattamento, portandola a 900°C, alla quale dalla microscopia riscaldante risultata una bagnabilità del vetroceramico sull'MW2 migliorata. È stato anche ipotizzato che la conseguente diminuzione di viscosità permettesse una maggiore fuoriuscita dei gas e un maggiore effetto del peso in Crofer sulla giunzione.

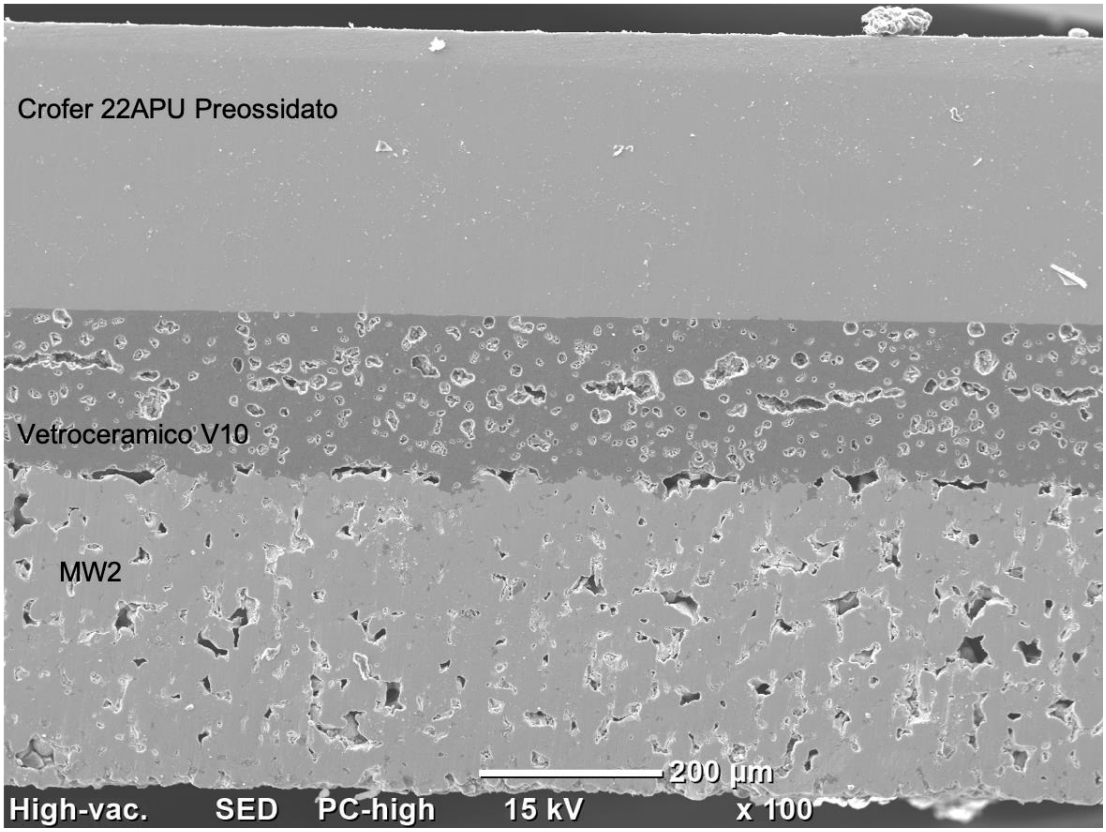

Figura 2:Immagine SEM del campione 8, ottenuto per trattamento a 850°C, 1h a 5°C/min, in aria..

Il campione 10 (Crofer preossidato su MW2, trattato a 900°C per 1h in aria) ha subito la rottura lungo l'interfaccia con la lega porosa durante la lucidatura e la stessa configurazione e trattamento sono state riproposte nel campione 11. L'adesione ai substrati metallici non ha subito variazioni significative se confrontate con il campione 8, che ha rappresentato fino a questo punto della sperimentazione i migliori risultati. La porosità tuttavia è stata ritenuta ancora troppo elevata e quella a metà spessore ancora presente.

4.1.1 Trattamenti in Argon

Per valutare l'influenza dell'atmosfera di trattamento sull'adesione e sviluppo dei pori alcune giunzioni sono state prodotte sotto flusso di Ar. La configurazione e trattamento per il campione 12 sono gli stessi dell'11. La giunzione risultava con uno spessore di circa 350µm, il vetroceramico ha infiltrato efficacemente l'MW2 fino a profondità di 50µm per la quasi totalità dell'interfaccia, anche quella con il Crofer è stata ritenuta soddisfacente. Nel vetroceramico, oltre ai pori diffusi ed irregolari, è possibile indentificare due linee di porosità in prossimità dei substrati metallici, e in aggiunta, alcuni vuoti grandi e tondeggianti. Le due linee di porosità sono molto probabilmente dovute all'elevato spessore della giunzione. Il campione 13 era identico al 12, tuttavia la lega porosa è stata degassata in Ar durante la giunzione del campione 12. I risultati sono stati analoghi, con l'eccezione di un minor spessore e conseguentemente una sola linea di porosità. L'adesione con l'MW2 è stata ottima, mentre quella con il Crofer si è rivelata insoddisfacente. Alcune zone non erano entrate in contatto con il vetroceramico, probabilmente a causa della deposizione irregolare della pasta di vetro.

4.1.2 Trattamenti in vuoto

Si è provato a questo punto ad effettuare trattamenti in vuoto per i campioni successivi, con l'obbiettivo di ridurre la porosità nello strato vetroceramico. Il campione 14 è stato il primo di questa serie. È stato realizzato con Crofer preossidato su MW2, in forno a vuoto a 900°C per 1h. Il

vetroceramico è stato riscontrato fino alla profondità di 160µm nelle cavità del poroso, e la relativa interfaccia è stata ottima. Una grande variazione ha coinvolto la porosità; meno vuoti, più grandi e di forma irregolare. Alcuni di questi erano in contatto, dunque nemmeno la porosità allungata lungo la giunzione è stata rimossa. L'interfaccia con il Crofer è risultata completamente staccata e occupata da detriti e bave metalliche. Il campione 15 ha ribaltato questa configurazione; i pori si sono ingranditi e localizzati in prossimità dell'MW2. L'interfaccia con il Crofer tuttavia non ha subito variazioni. In parallelo al campione 15 sono stai realizzati semplici rivestimenti di Crofer preossidato e MW2, infine una giunzione di solo Crofer preossidato. Quest'ultima è risultata molto sottile, il vetroceramico è stato completamente denso e privo di vuoi di dimensione rilevanti. Nei rivestimenti l'adesione è stata ottima, ma la porosità, seppur minore del campione 15 è stata comunque presente. Il trattamento è stato nuovamente modificato, con l'inserimento di uno step aggiuntivo in fase di riscaldamento di 1h a 500°C, con la speranza che potesse permettere al gas intrappolato nel vetroceramico di effondere. Il campione 16 ha utilizzato il trattamento precedentemente menzionato mantenendo la configurazione Crofer preossidato su MW2, è stata realizzata una giunzione Crofer-Crofer (preossidati) per confronto. I risultati di adesione hanno dato risultati analoghi al campione 14, la differenza più sostanziale è la presenza di un maggior numero di pori di dimensioni leggermente più contenute. La giunzione Crofer/Crofer è rimasta adesa al peso a causa dell'eccesso di vetroceramico, durante la rimozione in substrato inferiore ha subito il distacco. Le osservazioni SEM hanno restituito risultati comparabili alla giunzione Crofer-Crofer già studiata in precedenza.

L'ultimo tentativo con il sistema V10 è stato quello di giuntare i due substrati (poroso e denso) già rivestiti di vetroceramico. La temperatura è stata riportata a 850°C, lo step a 500°C eliminato e il trattamento eseguito in aria. Sulla lega porosa rivestita è stata depositata altra pasta di vetro e poggiato sopra Il Crofer preossidato e rivestito. La giunzione ottenuta presentava spessore considerevole, e i due substrati non erano allineati. A causa del ritiro il vetroceramico di giunzione non ha creato un'interfaccia continua con i rivestimenti. Anche in questi ultimi è stato possibile riscontrare le medesime porosità allungate, inizialmente osservate nel campione 8. È stata formulata l'ipotesi che la presenza sia influenzata dallo spessore dello strato di vetro depositato. Inoltre sembra che temperature minori favoriscano la formazione di porosità più piccole e distribuite, mentre temperature maggiori portino meno pori, ma più grandi e irregolari.

Diversi studi hanno riportato la presenza di reazioni redox tra il vetro e il substrato metallico, dove il primo si riduce e il secondo si ossida [33], [34]. In studi di bagnabilità in vuoto a 1000°C di un vetro disilicato di sodio, si sono formate bolle all'estremità della goccia di vetro. Alcuni metalli, quali Cr, reagiscono con l'ossido di sodio e silice per dare cromia e vapori di Na e SiO[33]. Maggiore compatibilità con la dimensione dei pori riscontrati nei campioni è stata ritrovata in letteratura per giunzione di leghe NI-Cr con vetro Si-Al-Li a 1000°C in Ar. Si sono osservati nel bulk dei vetroceramici vuoti considerevoli. Dopo aver rilevato la presenza di idrogeno è stato ipotizzato che l'acqua adsorbita sulle particelle di vetro, reagisse con le specie metalliche ossidandole e producendo idrogeno, rimasto poi intrappolato nel vetroceramico [34]. È verosimile pensare che la porosità allungata sia dovuto a reazioni redox, specialmente per le giunzioni trattate in argon. Si può quindi supporre che queste reazioni possono essere avvenute per i campioni in questione anche in vuoto e in aria.

4.2 Giunzioni con vetro GC2

Non è stato possibile evidenziare nessun margine di miglioramento con il sistema V10, si è deciso quindi di utilizzare un diverso sistema vetroso: l'GC2, che richiede un trattamento di giunzione di 950°C per 1h. L'GC2 possiede una temperatura di transizione vetrosa a 677°C e una massima cristallizzazione a 833°C. La fase cristallina principale è la Sanbornite ($BaSi_2O_5$), il CTE del vetroceramico è 11.4 $x10^{-6}$ K^{-1}.

Per il campione 20 è stata usata la configurazione di maggior successo dai test con il V10. Un riferimento Crof/crof (preossidati) è stato trattato in parallelo. L'GC2 ha mostrato una porosità ben distribuita e, a differenza del V10, tondeggiante. Il campione 20 (illustrato in *Figura 3*) non presentava alcuna porosità allungata a metà giunzione, ma solo dei pori più grandi della media a contatto con l'MW2. Le interfacce con entrambe le leghe sono risultate ottime, e l'infiltrazione in quella porosa efficace e costante.

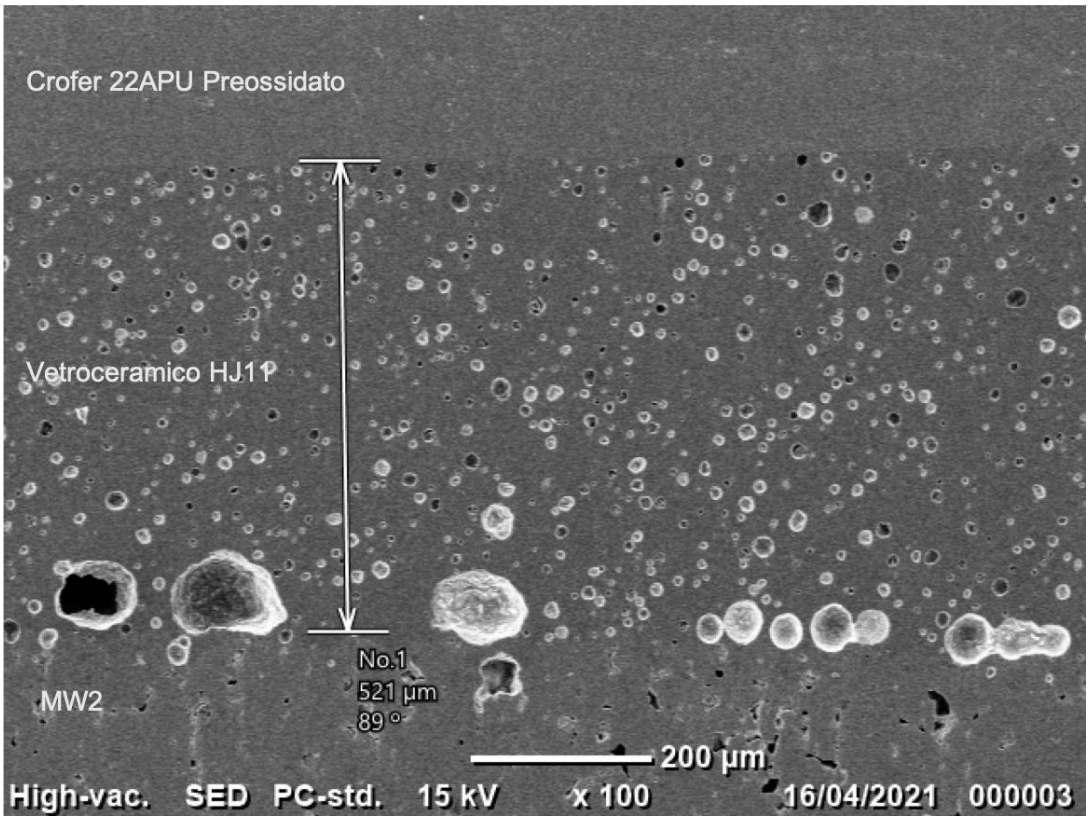

Figura 3: Immagine SEM del campione 20, ottenuto per trattamento a 900°C, 1h a 5°C/min, in aria.

I confronti da microscopio riscaldante tra il V10 e l'GC2 sulla lega porosa hanno evidenziato come quest'ultimo abbia sinterizzato maggiormente, e tendeva a ritirare in modo costante, senza aumenti di sezione dovuti alla cristallizzazione.

Dall'analisi morfologica della sezione trasversale dei campioni HSM V10 e GC2 è emerso che il vetro V10 è risultato più poroso dell'GC2, infiltrandosi in misura maggiore nell'MW2. Sulla lega porosa all'interfaccia con il vetroceramico V10, si è formato uno strato di ossido molto evidente. Inoltre, la faccia inferiore della lega presentava uno strato costituito da ossido di ferro quasi puro e molto spesso. Tale spessore, che non si è osservato nel vetro GC2, è probabilmente dovuto ad un'ossidazione precedente alla giunzione ad esempio ad un riscaldamento durante il taglio. L'osservazione della sezione della ha rivelato, in profondità alla giunzione, la presenza di cromato di bario ($BaCrO_4$). Questo composto si forma in presenza di O_2 per reazione di specie volatili di cromo con l'ossido di bario[35]. È indesiderato poiché a causa della CET maggiore del vetroceramico, può indurre stress termomeccanici nella giunzione[36]. La porosità della lega potrebbe essere il motivo per cui è possibile ritrovarlo anche a grande distanza dalle estremità della giunzione.

Le ultime prove sulle giunzioni GC2 sono state condotte includendo la variazione della posizione e dell'atmosfera del substrato. Nel campione 21 l'MW2 è stato posizionato superiormente, in questa configurazione si sono formati grossi pori all'interfaccia con la lega porosa e occasionalmente al Crofer. Il campione 22 (Crofer preossidato su MW2) è stato trattato in argon. È stata osservata l'insorgenza di pori grossi e omogeneamente distribuiti, accompagnata da un'ottima adesione ai substrati con infiltrazione fino a 50 µm di vetro in MW2. La presenza di vuoti è diretta conseguenza dal trattamento in Ar, e sarebbe deleteria per la resistenza meccanica.

I campioni che hanno fornito i migliori risultati in termini di adesione ai substrati, dimensione e distribuzione della porosità sono stati quelli di tipo 20 e rappresentano il miglior compromesso tra risultati ottenuti e complessità di realizzazione.

4.3 Analisi CT scan

Dall'analisi CT scan (in *Figura 4*) è possibile notare come gran parte delle porosità si localizza appena sopra l'interfaccia vetroceramico/MW2. Questi vuoti scompaiono man mano che ci si allontana dall'MW2. Nella meta superiore (in prossimità dell'interfaccia vetroceramico /Crofer) è stato rilevato un vuoto di grandi dimensioni che molto probabilmente si è generato a causa dell'aria intrappolata durante la deposizione.

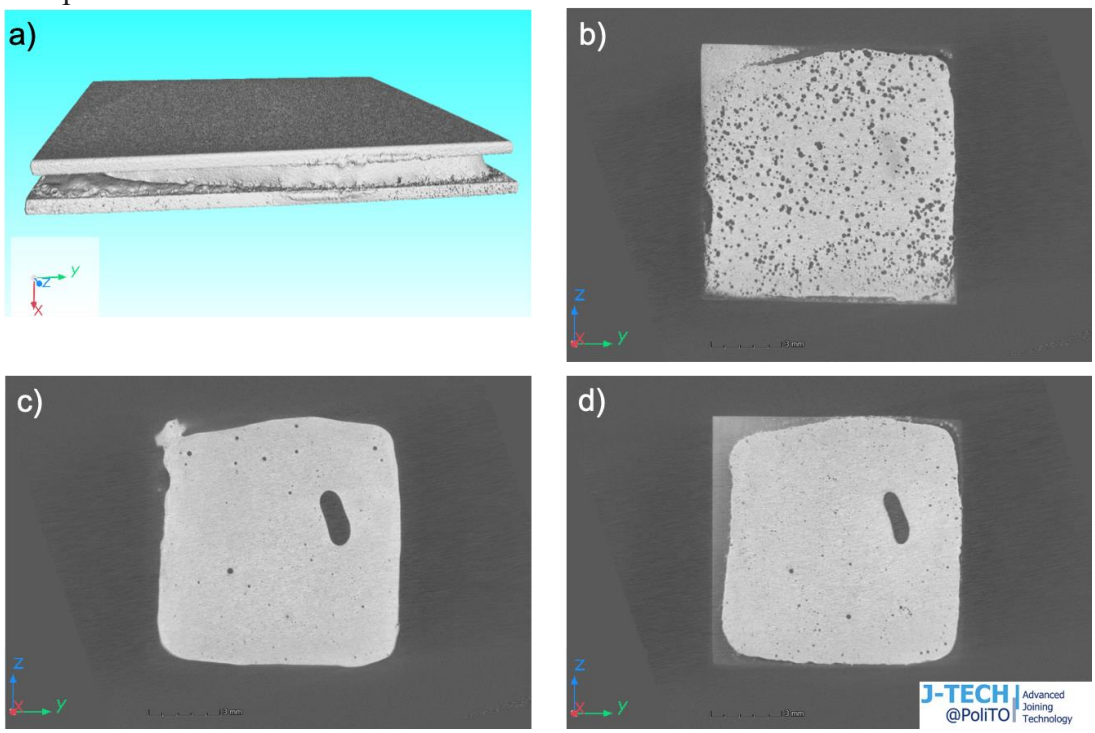

Figura 4: a) Ricostruzione tipo 20 tramite tomografia computerizzata, e sezioni a diverse altezze a partire dalla base della lega porosa. a) sopra l'MW2, b) a meta giunzione, c) in prossimità del Crofer.

4.4 Prove di trazione

Sono state eseguite prove di trazione ATSM C633-01 modificata sui campioni tipo 20. Tre giunzioni di tipo 20 sono state utilizzate, la cui resistenza si è attestata su valori di 7,4±0,5 MPa. Si è osservato che al Crofer rimaneva adeso la quasi totalità del vetroceramico, particolarmente evidente in un campione il 20-3 ($\sigma = 6{,}87\ MPa$). I risultati sono stati leggermente inferiori a quelli indicati da *Greven et al.*[37] per giunzioni di leghe bulk.

Le analisi SEM dei campioni hanno mostrato che il vetro ha coperto i substrati MW2 anche sui bordi esterni. Piccole porosità risultano evidenti sulle superfici di frattura. La frattura è di tipo adesivo sulla maggioranza dai campioni, mentre parzialmente coesiva su uno soltanto. Sulle superfici di frattura del campione 20-3 si è osservato la presenza di $BaCrO_4$, sia sul lato Crofer sia sulla superficie di frattura MW2. Il cromato di bario può essere la causa della minore resistenza del campione alla prova di trazione, unitamente alla porosità. Tuttavia, non è chiaro quale dei due abbia più influenza sulla resistenza.

Sono stati effettuati test sui campioni invecchiati che hanno coinvolto tre campioni tipo 20.

Il solo invecchiamento ha portato la resistenza delle giunzioni a 7,7±2,9 MPa, riducendo quindi solo parzialmente la resistenza media rispetto ai campioni non invecchiati.

5 Conclusioni

Due giunzioni sono state oggetto di osservazione in laboratorio. Inizialmente né Crofer né l'MW2 hanno dato buone adesioni in contemporanea. La pre-ossidazione del substrato denso ha migliorato la bagnabilità e la conseguente interfaccia, ma solo se veniva posizionato superiormente alla giunzione. Contrariamente l'adesione con l'MW2 peggiorava.
La configurazione che ha permesso un'adesione affidabile è stata ottenuta posizionando Crofer preossidato sulla parte superiore e MW2 sulla parte inferiore, ed utilizzando un carico di 15 g/cm^2. Tale configurazione ha dato origine, in modo sorprendente, ad una "cintura di pori" al centro del vetroceramico, potenzialmente deleteria per la resistenza a trazione. Sono stati effettuati dei tentativi per eliminarla, per esempio con un trattamento sottovuoto o in argon. Il rivestimento e i trattamenti in vuoto o argon non hanno dato giunzioni sufficiente solide. Nemmeno tentativi di fluidificare maggiormente il vetro, come aumentare la temperatura massima, o dare più tempo ai gas per evacuare il vetro, aggiungendo uno step nel riscaldamento, non hanno dato i risultati sperati. Un'altra variabile che agisce sulla formazione dei pori è lo spessore delle giunzioni, quando molto spesse era molto più probabile riscontrare una o più linee di porosità.
Poiché i risultati della giunzione con V10 non sono stati soddisfacenti, sono stati effettuati dei test su un secondo vetro, contenente Ba.

I campioni GC2, prodotti nella configurazione di maggior successo (Crofer preossidato sopra MW2, carico di 15 g/cm^2), hanno prodotto da subito una giunzione più efficacie. I pori sono risultati in quantità inferiore e più regolari rispetto al V10. Inoltre, l'infiltrazione era consistente ed il legame del vetro con l'interfaccia MW2 si è dimostrato ottimo. Ciò nonostante, sono apparsi pori di dimensioni maggiori proprio all'interfaccia con l'MW2. Qualora trattate in Argon la giunzione GC2 ha generato risultati complessivi ottimi in termini di adesione, ma pessimi per dimensione della porosità, cresciute notevolmente. La causa dei pori potrebbe risiedere nella reazione redox tra l'acqua adsorbita sulle polveri di vetro con le specie metalliche alle interfacce. Tale reazione produce, infatti, ossidi metallici e idrogeno che, accumulandosi, formano bolle all'interno del vetroceramico. All'interno dei pori del MW2 infiltrato è stato identificato del cromato di bario, sia ai bordi sia al centro della sezione della giunzione, diversamente da altri esempi noti in letteratura. La presenza al centro è dovuta, molto probabilmente, al maggior contatto con l'ossigeno nell'aria risultante dalle aperture nella lega MW2. Nonostante la persistenza di pori in prossimità della lega porosa, il campione 20 (Crofer preox. su MW2, GC2, trattato a 900°C, 1h, in aria) ha rappresentato il miglior compromesso risultati/complessità di realizzazione ed è stato selezionato per i test. In seguito a prove di trazione, è apparso evidente, tramite scansione CT della giunzione GC2, che le fratture si originano e si propagano appena sopra la lega MW2. Del cromato di bario è stato trovato sulla superficie di frattura interfaccia meno resistente. Pertanto, per capire se è la "cintura di pori" o la formazione di $BaCrO_4$ ad impattare in modo più deleterio sulla resistenza, occorre effettuare ulteriori studi. La crescita del cromato di bario con la permanenza ad alte temperature può aver introdotto micro cricche, che si sono propagate facilmente in fase di prove meccaniche.
Per far fronte alle lacune di vetro sotto la piastra superiore, è preferibile effettuare una deposizione meccanica invece che manuale. La formazione di $BaCrO_4$, invece, è un limite intrinseco del sistema lega-vetroceramico che può solo essere contenuto.
Ulteriori test e su un maggior numero di campioni sono necessari per stabilire una migliore configurazione e chiarire i meccanismi di frattura in funzione dei trattamenti di invecchiamento delle giunzioni. Questa tesi rappresenta uno dei primi tentativi di giunzione di leghe porose e leghe bulk utilizzando i vetroceramici.

6 Bibliografia

[1] W. Holand and G. H. Beall, *Glass-Ceramic Technology*. Newark: John Wiley & Sons, Incorporated, 2019.

[2] A. K. Varshneya and J. C. Mauro, *Fundamentals of Inorganic Glasses*. San Diego: Elsevier, 2019.

[3] M. Salvo and F. Smeacetto, "Materiali Vetrosi." Dipartimento di Scienza Applicata e Tecnologia, Politecnico di Torino, Italy, 2018.

[4] N. Russo, "' Fuel Cells and H2 Generation ,'" 2020, p. 0.

[5] S. M. Haile, "Fuel cell materials and components," *Acta Mater.*, vol. 51, no. 19, pp. 5981–6000, 2003, doi: 10.1016/j.actamat.2003.08.004.

[6] E. Ivers-Tiffée, A. Weber, and D. Herbstritt, "Materials and technologies for SOFC-components," *J. Eur. Ceram. Soc.*, vol. 21, no. 10, pp. 1805–1811, 2001, doi: https://doi.org/10.1016/S0955-2219(01)00120-0.

[7] J. Molenda, K. Świerczek, and W. Zajac, "Functional materials for the IT-SOFC," *J. Power Sources*, vol. 173, no. 2 SPEC. ISS., pp. 657–670, 2007, doi: 10.1016/j.jpowsour.2007.05.085.

[8] H. H. Möbius, "On the history of solid electrolyte fuel cells," *J. Solid State Electrochem.*, vol. 1, no. 1, pp. 2–16, 1997, doi: 10.1007/s100080050018.

[9] S. Skinner, "Recent Advances in Perovskite-Type Materials for SOFC Cathodes," *Fuel Cells Bull.*, vol. 4, pp. 6–12, 2001, doi: 10.1016/S1464-2859(01)80254-6.

[10] S. Park, J. M. Vohs, and R. J. Gorte, "Direct oxidation of hydrocarbons in a solid-oxide fuel cell," *Nature*, vol. 404, no. 6775, pp. 265–267, 2000, doi: 10.1038/35005040.

[11] A. Atkinson *et al.*, "Advanced Anodes for High-Temperature Fuel Cells," *Nat. Mater.*, vol. 3, pp. 17–27, 2004, doi: 10.1038/nmat1040.

[12] M. Gong, X. Liu, J. Trembly, and C. Johnson, "Sulfur-tolerant anode materials for solid oxide fuel cell application," *J. Power Sources*, vol. 168, no. 2, pp. 289–298, 2007, doi: https://doi.org/10.1016/j.jpowsour.2007.03.026.

[13] O. A. Marina, N. L. Canfield, and J. W. Stevenson, "Thermal, electrical, and electrocatalytical properties of lanthanum-doped strontium titanate," *Solid State Ionics*, vol. 149, no. 1, pp. 21–28, 2002, doi: https://doi.org/10.1016/S0167-2738(02)00140-6.

[14] S. Zha, P. Tsang, Z. Cheng, and M. Liu, "Electrical properties and sulfur tolerance of La0.75Sr0.25Cr1−xMnxO3 under anodic conditions," *J. Solid State Chem.*, vol. 178, no. 6, pp. 1844–1850, 2005, doi: https://doi.org/10.1016/j.jssc.2005.03.027.

[15] S. Wang, M. Liu, and J. Winnick, "Stabilities and electrical conductivities of electrode materials for use in H 2 S-containing gases," *J. Solid State Electrochem. - J SOLID STATE Electrochem*, vol. 5, pp. 188–195, 2001, doi: 10.1007/s100080000142.

[16] T. Nakamura, G. Petzow, and L. J. Gauckler, "Stability of the perovskite phase LaBO3 (B = V, Cr, Mn, Fe, Co, Ni) in reducing atmosphere I. Experimental results," *Mater. Res. Bull.*, vol. 14, no. 5, pp. 649–659, 1979, doi: https://doi.org/10.1016/0025-5408(79)90048-5.

[17] N. Mahato, A. Banerjee, A. Gupta, S. Omar, and K. Balani, "Progress in material selection for solid oxide fuel cell technology: A review," *Prog. Mater. Sci.*, vol. 72, pp. 141–337, 2015, doi: 10.1016/j.pmatsci.2015.01.001.

[18] Y. Larring and T. Norby, "Spinel and Perovskite Functional Layers Between Plansee Metallic Interconnect (Cr-5 wt {\%} Fe-1 wt {\%} Y[sub 2]O[sub 3]) and Ceramic (La[sub 0.85]Sr[sub 0.15])[sub 0.91]{MnO}[sub 3] Cathode Materials for Solid Oxide Fuel Cells," *J. Electrochem. Soc.*, vol. 147, no. 9, p. 3251, 2000, doi: 10.1149/1.1393891.

[19] F. Smeacetto, "Glass ceramics for energy conversion devices." "Ceramici avanzati" Course of study, Politecnico di Torino, 2018.

[20] R. N. Singh, "Sealing Technology for Solid Oxide Fuel Cells (SOFC)," *Int. J. Appl. Ceram. Technol.*, vol. 4, no. 2, pp. 134–144, 2007, doi: https://doi.org/10.1111/j.1744-7402.2007.02128.x.

[21] Y.-S. Chou and J. Stevenson, “Novel Silver/Mica Multilayer Compressive Seals for Solid-Oxide Fuel Cells: The Effect of Thermal Cycling and Material Degradation on Leak Behavior,” *J. Mater. Res.*, vol. 18, pp. 2243–2250, 2003, doi: 10.1557/JMR.2003.0313.
[22] J. W. Fergus, “Sealants for solid oxide fuel cells,” *J. Power Sources*, vol. 147, no. 1–2, pp. 46–57, 2005, doi: 10.1016/j.jpowsour.2005.05.002.
[23] B. Timurkutluk, C. Timurkutluk, M. D. Mat, and Y. Kaplan, “A review on cell/stack designs for high performance solid oxide fuel cells,” *Renew. Sustain. Energy Rev.*, vol. 56, pp. 1101–1121, 2016, doi: 10.1016/j.rser.2015.12.034.
[24] F. Smeacetto, “Solide oxide cells materials.” “Ceramici avanzati” Course of study, Politecnico di Torino, 2018.
[25] D. Udomsilp *et al.*, “Metal-Supported Solid Oxide Fuel Cells with Exceptionally High Power Density for Range Extender Systems,” *Cell Reports Phys. Sci.*, vol. 1, no. 6, 2020, doi: 10.1016/j.xcrp.2020.100072.
[26] M. C. Tucker, “Progress in metal-supported solid oxide fuel cells: A review,” *J. Power Sources*, vol. 195, no. 15, pp. 4570–4582, 2010, doi: 10.1016/j.jpowsour.2010.02.035.
[27] S. M. Gross, T. Koppitz, J. Remmel, J. B. Bouche, and U. Reisgen, “Joining properties of a composite glass-ceramic sealant,” *Fuel Cells Bull.*, vol. 2006, no. 9, pp. 12–15, 2006, doi: 10.1016/S1464-2859(06)71320-7.
[28] D. Koszelow, M. G. Makowska, F. Marone, J. Karczewski, P. Jasinski, and S. Molin, “Corrosion Science High temperature corrosion evaluation and lifetime prediction of porous Fe22Cr stainless steel in air in temperature range 700-900 ° C.”
[29] N. J. Magdefrau, L. Chen, E. Y. Sun, and M. Aindow, “Effects of alloy heat treatment on oxidation kinetics and scale morphology for crofer 22 APU,” *J. Power Sources*, vol. 241, pp. 756–767, 2013, doi: 10.1016/j.jpowsour.2013.03.181.
[30] A. G. Sabato *et al.*, “Effect of electric load and dual atmosphere on the properties of an alkali containing diopside-based glass sealant for solid oxide cells,” *J. Power Sources*, vol. 415, no. October 2018, pp. 15–24, 2019, doi: 10.1016/j.jpowsour.2019.01.051.
[31] F. Baino and C. Vitale-Brovarone, “Wollastonite-containing bioceramic coatings on alumina substrates: Design considerations and mechanical modelling,” *Ceram. Int.*, vol. 41, no. 9, pp. 11464–11470, 2015, doi: 10.1016/j.ceramint.2015.05.111.
[32] S. Tecnica, “Araldite ® 2015,” no. April 2007, pp. 1–6, 2015.
[33] A. P. Tomsia, Z. Feipeng, and J. A. Pask, “Reactions and Bonding of Sodium Disilicate Glass with Chromium,” Berkeley, California 94720, 1985.
[34] L. D. Haws, D. P. Kramer, W. E. Moddeman, G. W. Wooten, and M. Research Corporation, “High Strength Glass-Ceramic to Metal Seals,” MOUND Miannisbung, Ohio ^45342, 1986.
[35] Z. Yang, K. S. Weil, D. M. Paxton, and J. W. Stevenson, “Selection and Evaluation of Heat-Resistant Alloys for SOFC Interconnect Applications,” *J. Electrochem. Soc.*, vol. 150, no. 9, p. A1188, 2003, doi: 10.1149/1.1595659.
[36] C. W. P. T. PISTORIUS and M. C. PISTORIUS, “Lattice constants and thermal-expansion properties of the Chromates and selenates of lead, strontium and barium:,” *Zeitschrift für Krist. - Cryst. Mater.*, vol. 117, no. 1–6, pp. 259–272, 1962, doi: doi:10.1524/zkri.1962.117.16.259.
[37] B. Cela Greven *et al.*, “Torsional shear strength of novel glass-ceramic composite sealants for solid oxide fuel cell stacks,” *Int. J. Appl. Ceram. Technol.*, vol. 15, no. 2, pp. 286–295, 2018, doi: 10.1111/ijac.12819.

1 Introduction

Solid Oxide Cells (SOCs) have attracted a great interest in the last years, as they offer a viable energy production, with significant power and efficiencies if compared to conventional electrolysers for stationary users.
They are a proven system providing high power outputs for several thousand hours. However, they present some critical issues such as the long start-up times, the high operating temperatures.
Metal supported solid oxide cells, or MSOC in short, utilize a porous metal sheet to provide greater toughness, lower operating temperature and faster start-ups. The greater flexibility, resistance and potentially lower costs are particularly interesting for mobile systems or emergency power unit on board of planes for example. In building stacks critical role is played by the sealant and no record of porous alloy joining via glass-ceramic was found in literature. Previous studies focused on porous-to-porous or porous-to-bulk joining uniquely for ceramic substrates. It is of particular technological interest the study of glass-ceramic bonding of porous metals to other porous or bulk alloys, apart from substrates and electrodes for fuel cells applications include gas separation membranes.

The aim of this study is to manufacture, characterize and mechanically test a porous to bulk alloy joining via glass-ceramic; namely and an experimental porous alloy sheet and Crofer 22APU, a well-established interconnect alloy for fuel cells. The first chapter focuses on the glass-ceramics class of material, with an overview of its developmental history, manufacturing and fields of application. The attention then shifts to fuel cells; their basic working principles along with types and materials of the SOFC type. Metal-supported cells will be explained in greater details; components, materials and latest developments. Chapter two analyses the state of the art of porous-to-bulk substrate joining via glass-ceramics, whether of metal or ceramic. The third chapter explains in detail the materials and the procedures used to manufacture and analyse the joints. The fourth chapter illustrates and explains the results obtained. It is divided into two different sections, each dedicated on the work focused on a particular glass system. The first is concentrated on the characterization only via SEM and EDS microscopy. Tensile mechanical tests on pre and post-aging samples and CT scan were carried out on the best configuration obtained with the second glass. The fifth chapter is dedicated to the conclusions and overview of the results.

1.1 Glass-ceramics: definition, history and key concepts

A glass-ceramic is a material originated from inorganic glasses which have the ability to nucleate and grow crystals. Composed of one or more crystalline phases in a glass matrix, they sit between inorganic glasses and ceramics. Crystals grown from the matrix, alter its composition and impart unique properties[1].

A glass is an amorphous solid that has been obtained from a progressive cooling of a liquid unable to crystallize. It is characterized by long range disorder and no periodicity, it does not melt at a specific temperature. Instead it features a glass transition temperature T_g, above which progressively softens, its X-Ray diffraction spectrum presents a broad and shallow band instead of sharp defined peaks[2].

Main glass components are:

- Network formers: form the backbone of the glass network and usually constitute the major component. The most common formers are SiO_2, GeO_2, TeO_2, P_2O_5.
- Network Modifiers: they are not able to vetrify but interrupt the amorphous reticle lowering the melting temperature. They differentiate from network formers by the strength of the bonds

being higher in the latter. The most common modifiers are alkali oxides (e.g. Li_2O, Na_2O, K_2O) and alkali-earth oxides (e.g. MgO, CaO, BaO, SrO).

- Intermediates: cannot form a network as charge balance is required (e.g. Al_2O_3) in limited quantities are integrated into the network of another oxide former[3].
- Additives: substances added to alter characteristics, for example: refractive index, ease of nucleation (Y_2O_3, ZnO, PbO, TiO_2, ZrO_2 just to name a few).

Two main theories describe glass formation: a structural theory, Zachariasen's random network theory and a kinetic theory. The former states that some constituents can form a glass if can form random 3-D network with internal energy similar to its crystalline counterpart. The latter instead states that a glass is formed when the cooling rate is greater than its crystallization speed[3].

Glasses are characterized by intrinsic thermodynamic instability and tend to evolve into more stable configurations when are given the right conditions. In order to obtain a glass-ceramic, nucleation and growth of crystal species is needed and promoted by heating at a sufficient temperature for enough time where the crystallization rate is sufficiently high; an example of heat-treatment to obtain a glass ceramic is represented *Figure 1.1*[3].Nucleation can be homogeneous or heterogeneous, the first one starts in the bulk of the material while the other at surface imperfections [3]. Growth of the crystals presupposes the stability of the same; a critical size must be achieved, otherwise the devitrification cannot occur [3]. There is a great variability in the composition, in order to achieve different properties and to be very finely tuned for the desired application. Most of the G-C (glass-ceramics) microstructure cannot be obtained in any other way, constituting special morphologies function of the growth mode.

The two most important factors in development of a glass-ceramic are composition and microstructure. The former determines the capability to produce a glass and its workability, and ultimately weather the nucleation can happen internally or by surface defects. By adding for example, a nucleating agent into the glass bulk composition it's possible to improve internal nucleation. Composition also plays a major role in the crystalline structure, chemical and physical properties like hardness, thermal expansion and behaviour in aggressive means. Microstructure is greatly dependent on the thermal treatment and plays the determining role in mechanical and optical properties by promoting or diminishing the characteristic of the crystals[1].

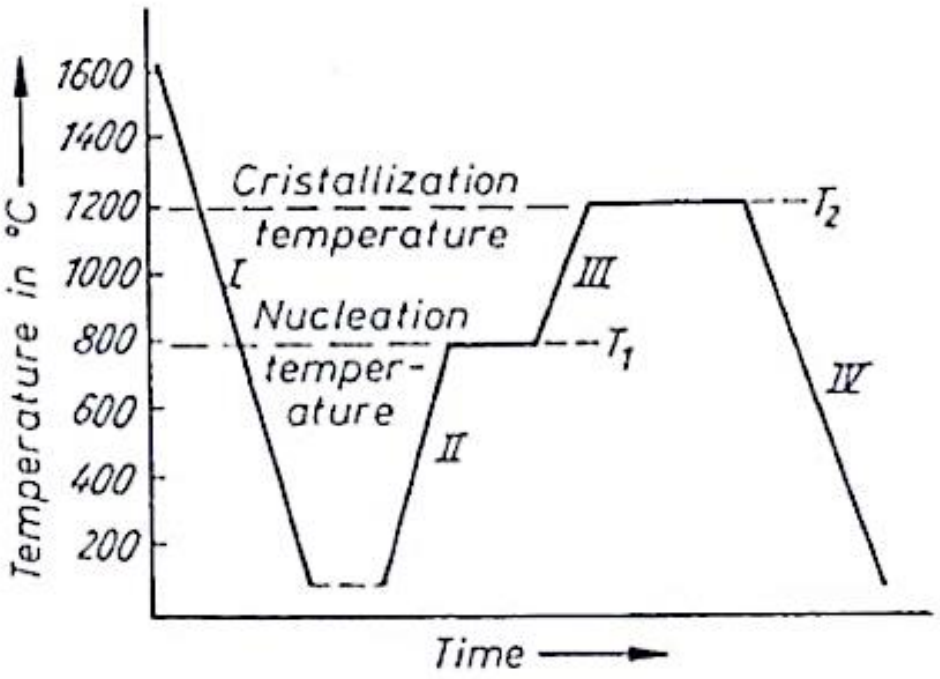

Figure 1.1: example of heat treatment to obtain a glass ceramic. I)primary forming, II)nucleation phase, III)Growth phase, IV) Cooling [2].

The nature of the crystalline phase, glass phase and the interface between the two is responsible for the varying chemical resistance amongst the G-C: it is possible to have a very high chemical resistance or absorbability, or a combination of the two; glass is absorbable and the crystal phase imparts chemical resistance. As a result, biocompatible glass-ceramics with great durability have been used in medicine and particularly in dentistry. Crystals present cleavage planes and, where they meet grain boundaries. These features of the crystalline solid allow greater mechanical properties and tenacity, crack can deflect, branch unlike in glassy solids. Greater variability in properties of crystalline ceramics is evident for example in sapphire, extremely hard, or soft like mica, some can have low or even negative thermal expansion coefficients or other unusual luminescent, dielectric or magnetic properties. Glass-ceramics can have varying optical properties: from opaque to very high transparency, depending on glass phase content, to visible and IR fluorescence and practically any colour can be obtained. They are also capable to be machined as the primary shaping and G-C forming, polished, and controlled for abrasion behaviour and roughness. As for mechanical properties can exhibit flexural strengths of 500 MPa and K_{IC} greater than 3 $MPa \bullet m^{1/2}$, no other material provides such mechanical properties along with translucency, no shrinking, pore development and production versatility. They are relevant as insulators and micro-electronics, furthermore they have been shown to exhibit ion conductivity and superconductivity. Piezoelectricity or optical polarization can be imparted to the G-C by orientating the crystals in the matrix[1].

This category of materials was first discovered in the mid-1950s by glass chemist Dr. S.D Stookey while trying to precipitate silver particles in lithium silicate glass to obtain permanent photographical images. Such glasses where chosen in virtue of lithium content that imparted the best chemical durability amongst the alkali silicate ones. Silver precipitation occurred once the glass was heated above the glass transition temperature at 450°C after being irradiated with UV light. By accidentally heating the glass at 850°C for several hours instead of a pool of molten glass he found a white material without shape change. Even when dropped the now treated glass emitted a metal like sound indicating unusual strength. He recalled that lithium aluminosilicate crystals (β-spodumene) had very low thermal expansion coefficient. By uniformly nucleating such crystals he could produce very high thermal shock resistant glass materials. Silver particles or other colloidal methods were not suitable for the precipitation, but inspiration came with the opal thermometer glasses used at the time. They

are obtained by precipitating high refractive index crystals with Zinc sulphide or titanium oxide nucleating agents giving a distinct white opaque colour. By adding TiO_2 particles to the aluminosilicate glass melt the results were completely successful. This discovery led to the production and commercialization of high strength and thermal shock resistant glass for rocket cones and cookware[1].

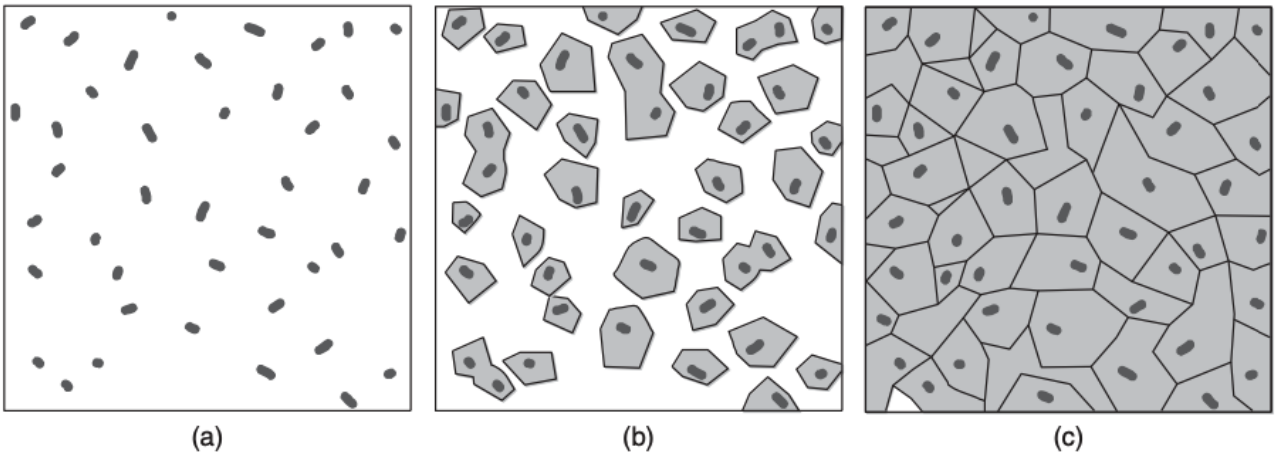

Figure 1.2:Formation of a glass-ceramic. a) formation of nuclei b) growth c) final microstructure.[1]

Nucleation starts at lower energy sites such as surfaces, and when this happens, crystallization proceeds from the external surface to the core in a well oriented direction, where they meet a weak plane arises. The core has not yet crystallized and as it flows in response to the devitrification it can cause significant distortion. By internal nucleation of glass and due to the uniform crystallization at high viscosities the glass turns into a ceramic without any shape change.

Another way to obtain the ceramization of a glass without resorting to nucleating agent is the sintering and crystallization of finely ground glass; this is the technique through which the G-C treated in this work is obtained. It consists in milling a quenched glass, called a frit, into powders generally ranging in the size of 3-25 μm particles; than they are used to produce a slurry and deposited on the substrate for firing. The G-C if formed by the sintering and subsequent crystallization of the powders, this yields very similar results to the devitrification of bulk glasses. This approach allows for some advantages compared to the body crystallized G-C. In this case crystallization starts at the site of highest energy, namely the surface imperfections of the powders, already evenly distributed along the ground glass without the need of nucleating agents and their optimal dispersion. As *Figure 1.3* c*)* shows the result are similar to bulk glass ceramics shown in *Figure 1.2 c)*. techniques such as slip casting, pressing, extruding or tape casting can be used. The low viscosity before the crystallization allows the G-C to be applied on ceramics or metals. Conventional ceramic production The frit-derived G-C were first commercially used as solder to seal television bulbs and it was later used to produce cofired multilayer substrates in electronic packaging, biomaterials and dental restoration[1].

There are three main application in energy production field in which glass ceramics are employed: the first one is the more efficient use of solar energy. It is possible to create a luminescent solar collector. It is constituted by a thin sheet of transparent mullite G-C doped with Cr^{3+} ions. The doping agent converts the absorbed light into IR by luminescence. The rays so produced are reflected in the air pocket and concentrated as 2D waveguide reaching the photovoltaic silicon strips fixed at the G-C edge. Second one is the production of components for batteries. They are so composed: anode, cathode and electrolyte. Some of these components are organic hence flammable, like cathodes and electrolytes. It is possible to substitute these components with G-C with the same functions. A promising alternative to conventional cathodes in lithium batteries is based on $LiFePO_4$-GC. Some advantages include high resistance to charge-discharge cycles, absence of rare and harmful elements, and greater conductivity when produced via solid state reaction. Li/air batteries feature porous carbon

cathode, lithium anode and Pt catalyst. Alternative G-C electrolytes have been developed featuring conductivities between $1x10^4$ to $3x10^{-4}$ S/cm depending on the production method [1].

The last energy application involves solid oxide fuels cells (SOFC) where glass-ceramics are applied as sealants between the components of the device, but this will be explained in the following section.

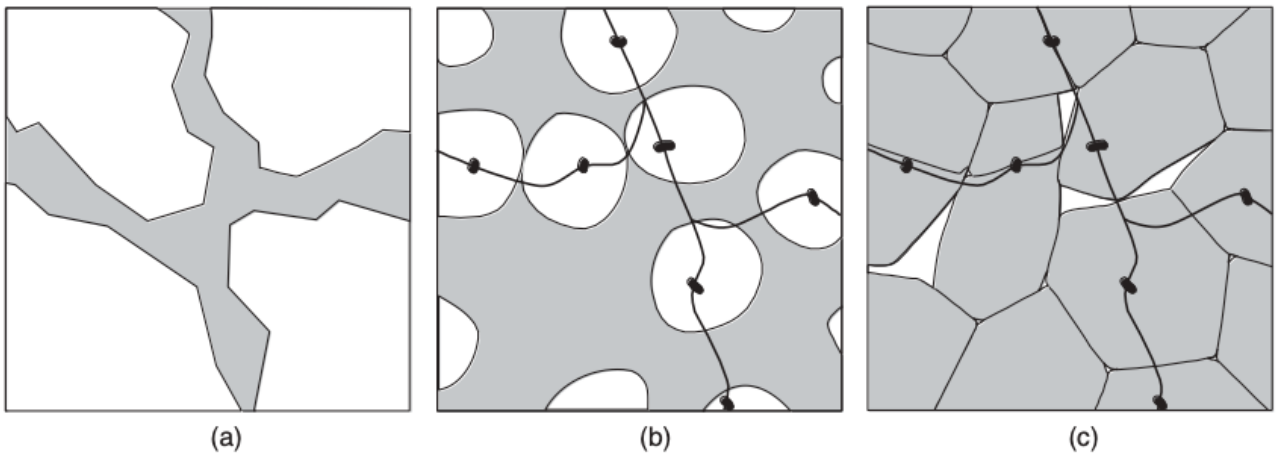

Figure 1.3:from powdered glass to glass-ceramic. a)powder compact b) densification and initial crystallization c) frit-derived glass-ceramic [1].

1.2 Fuel Cells

Fossil fuels generate a great quantity of greenhouse gasses. The progressive increase of the emission limits and lowering of the fossil fuel resources are pushing the scientific world toward alternative and cleaner energy production methods. These alternative energy sources could play a major role in reducing geopolitical, supply chain and social problems. Fuel cells have risen as a potential solution to internal combustion engines for cleaner, silent (as no moving parts are present), more efficient and more durable power system[4].

1.2.1 Definition and basic functioning

A fuel cell is a reactor that converts, through a spontaneous red-ox reaction, chemical energy into electrical energy and heat[5]. The main components of a fuel cell are: an electrolyte, a cathode and anode. They are often referred as membrane electrode assembly (MEA) or simply single-cell fuel cell, an example is shown in *Figure 1.4*.

Hydrogen is conveyed at the anode while the oxidant at the cathode. Non-direct combustion happens as the fuel and the oxidant are separated by the electrolyte. At the cathode oxygen is reduced to O^{2-} by electrons produced with the oxidation of the fuel (in this case H_2) happening at the anode. Here, water is produced and constitutes a by-product and must be removed. An electrical circuit allows for electrons to flow from the anode to the cathode. Aside from separating the gas flows the electrolyte conducts ions; depending on the electrolyte positive or negative ions can be transported.In the case of ion conduction for hydrogen fuel the reaction are as follows:

Cathodic reaction: $\frac{1}{2}O_2 + 2e^- \rightarrow O^{2-}$

Anodic reaction $H_2 + O^{2-} \rightarrow H_2O + 2e^-$

Complete reaction: $\frac{1}{2}O_2 + H_2 \rightarrow H_2O$.

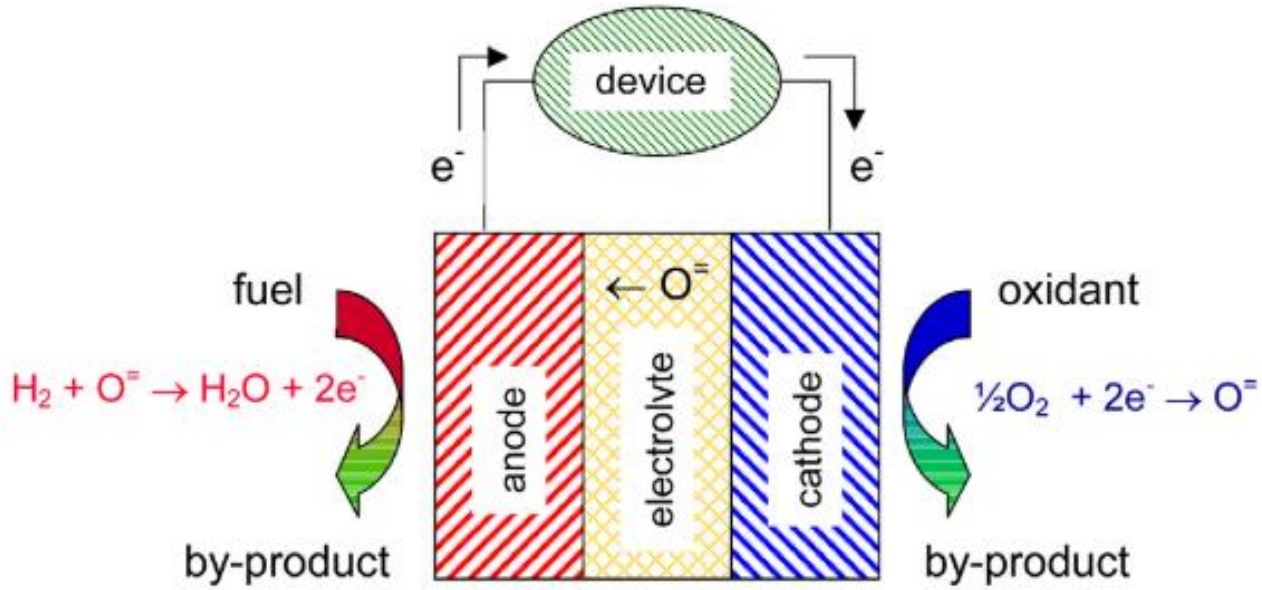

Figure 1.4: schematic of a fuel cell [5].

For proton conduction:

Cathodic reaction: $\frac{1}{2}O_2 + 2H^+ + 2e^- \rightarrow H_2O$

Anodic reaction $H_2 \rightarrow 2H^+ + 2e^-$
The complete reaction remains the same. The external electrical circuit allows for electron flow to balance the ion movement in order to sustain the reaction [5].

1.2.2 Functioning characteristics

The parameter that indicates the performance of the cell is the voltage, it's a function of current density or polarization curve indicated in *Figure 1.5*.
The voltage can be measured and expressed by the following equation.

$$E = E_{eq} - E_L - \eta_{act} - \eta_{iR} - \eta_{diff}$$

E_{eq} is the potential of the cell at the equilibrium, E_L the tension loss due to the electrolyte losses, η_{act} the overpotential needed for slow reaction at the electrodes to occur, η_{iR} are the losses due to ohmic resistance of the cell and η_{diff} the overpotential to overcome diffusion barriers.

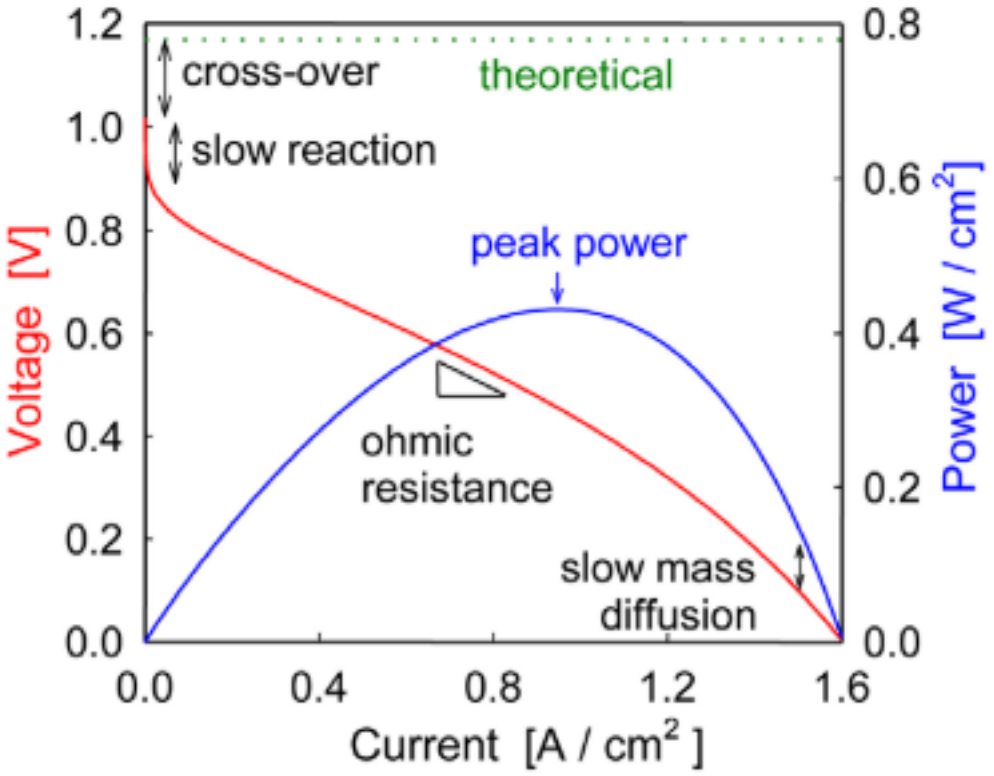

Figure 1.5:schematic of polarization curve of a fuel cell [5].

- E_{eq}: it is calculated from the Nerst potential, requiring the partial pressures of the species in the reaction. It is then defined as:

$$E_{eq} = -\Delta G/nF$$

Where ΔG is the Gibbs free energy of the reaction, *n* the number of electrons exchanged and F the Faraday constant equal to F=96,485 C•mol^{-1}. However, they are not measured but obtained by comparison with the standard cell potential[5]:

$$E°(T) = -\Delta G°(T)/nF$$

ΔG° being the standard Gibbs free energy of the reaction for the production of H_2O and equal to -237,1kJ•mol^{-1}, so the standard potential is 1,23 V [6].
The potential of a cell in non-standard condition is obtained from the Nerst equation knowing that:

$$\Delta G = \Delta G°(T) + RT \ln \frac{P_{H_2} P_{O_2}^{1/2}}{P_{H_2O}}$$

With R the universal gas constant 8,314 J•(mol K)$^{-1}$, the temperature T in Kelvin and the product of the partial pressures elevated to the stoichiometric constants of the reagents divided by the partial pressures of the products as the argument of the ln.
The equilibrium potential of the cell can be calculated with the following equation:

$$E_{eq} = -\frac{\Delta G°(T)}{nF} - \frac{RT}{nF} \ln \frac{P_{H_2} P_{O_2}^{1/2}}{P_{H_2O}} = E°(T) - \frac{RT}{nF} \ln \frac{P_{H_2} P_{O_2}^{1/2}}{P_{H_2O}}$$

- E_L : is the potential loss due to gas leaks through the membrane of electrolyte fractures, typical of high temperature cells where reaction kinetics at the electrodes are fast.

- η_{act} : slow electrode reactions require ad additional voltage that can be estimated as:

$$\eta_{act} \cong \frac{RT}{\alpha nF} \ln\left(\frac{I_0}{I}\right)$$

Where α is the transfer coefficient, I_0 the current equally exchanged at the equilibrium and I the current in non-standard conditions. Regardless of the electrolyte for all hydrogen cells the slowest reactions occur at the cathode and it's responsible for the majority of the activation losses. They decrease at the increase of temperature and could even amount to zero in case of higher temperature cells. The anode could also limit the reaction kinetics only in case of hydrocarbon or non-pure hydrogen fuels.

- η_{iR} : the single cell components are characterized by specific resistivities per unit surface indicated by the term R define as area specific resistance (ASR). The ohmic losses assume the value of I•R.
- η_{diff} : this term is a function of the geometry of the cell but above all on the velocity of the reagents are able to reach the site of the reaction and the products to leave it. By increasing the absorbed current the products tend to accumulate and cathode and anode see a lower concentration of oxidizer and fuel respectively. To counter this diffusion phenomena an overpotential is needed to overcome the slow diffusion effects on the reaction kinetics [5], [7].

Efficiency is inversely proportional to the applied overpotential but reaches its maximum at low current densities. High energy densities and efficiencies can be obtained when gas diffusion, electron transport are slow and cathode electrocatalysis, being rate limiting, is fast especially for bulk diffusion though porous electrodes[5]. To increase the output voltage multiple MEA are stacked into larger assemblies[4].

1.2.3 Types of fuel cells

Different types of fuel cells are shown in *Table 1.1*. Hydrogen fuel cells convert chemical energy into electrical energy and heat, generally have efficiencies from 40% to 80% in the heat is recovered.

Table 1.1:Parameters of the different types of fuel cells[8].

FC Type	Electrolyte	Transported Ion	Fuel	Operating temperatures [°C]	Efficiency
PEM-FC	Polymer membrane	H^+	Pure H_2, CH_3OH or hydrocarbons	50 - 80	40-50%
Alkaline-FC	KOH	OH^-	Pure H_2, idrazine	50 -200	50-55%
MC-FC	Nitrates, sulphates, carbonates	CO_3^{2-}	H_2, CO, natural gas, propane	630 - 650	50-60%
SOFC	Ceramic (YSZ, doped perovskites)	O^{2-}	Natural gas, propane	600 - 1000	45-60%

Since no infrastructure for H_2 distribution exist, different expedients have been used. By feeding the cell with natural gas and produce hydrogen in-situ via hydrocarbon reforming, the process is carried out by the cell itself. This however requires higher operating temperatures.

- PEMFC specifically have a Nafion®-based membrane. The electrodes are composed of finely dispersed 30%wt Pt particles (20-40 Å) on non-porous conductive carbon powders. The requirement for platinum is as high as 0,25mg/cm^2. A single MEA can produce up to 1,16v output. The lack of any mechanical step allows greater efficiency compared to internal combustion engines, 40-50% compared to the 25% maximum of a diesel engine. Common use is for transportation systems, but are also considered for residential energy source and for portable devices; in this case methanol is the energy source as it's supplied in simple cartridges, making it safer and easily transported. The main advantages of these systems are: high power density, a very fast start-up making it suitable in the automotive sector, no corrosion and low operating temperature[4]. The latter property implies the need for significant amount of noble metals like Pt to carry out electrocatalysis reactions. Especially formulated Pt-alloys could be used instead for impure hydrogen fuels in H_2/air fuel cells. Impure hydrogen is usually the result of steam reformate and contains a variable amount of CO that at low temperature could poison the catalyst, negatively impacting the performance. In case of direct-methanol cells a 50:50 Pt/Ru catalyst mix is used in virtue of the ability for Ru to oxidize adsorbed CO. The requirement for significant amounts of noble metal catalysts, consequently high costs and very low CO tolerance constitute the major drawbacks.

- Phosphoric acid fuel cells (PAFC) have the same functioning of PEMFC, but tolerate greater concentration of carbon monoxide and operate at 200°C. Phosphoric acid adsorbed on SiC constitute the electrolyte and lower Pt concentrations are required. The main problems are the great cost, low current densities, corrosion phenomena and longer start-up times.

- The working of an Alkaline FC is identical to the ones previously mentioned, the difference lies in the transported ion (OH^-) and the electrolyte, composed of KOH. They provide better kinetics than PEMFC, operate at lightly higher temperatures and no peroxides are formed. Since the oxidizing gas is supplied with air it is possible to have CO_2, that reacts with the electrolyte progressively lowering the power output. This makes them impractical whenever carbon dioxide is present.

- Molten carbonate fuel cells (MCFC) like SOFC can perform internal reforming, Ni is used as a catalyst. Hydrocarbons are mixed with steam at about 650°C and fed at the anode: hydrogen is produced with the energy provided by the fuel cell. The transported ion CO_3^{2-} takes directly part in the reaction at the anode and is reformed at the cathode. The anode is composed of Ni and Cr while the cathode of Ni and Li.
  Anodic reactions:

$$H_2 + CO_3^- \rightarrow H_2O + CO_2 + 2e^-$$

$$CO + CO_3^- \rightarrow 2CO_2 + 2e^-$$

  Cathodic reaction:

$$\frac{1}{2}O_2 + CO_2 + 2e^- \rightarrow CO_3^-$$

  As hydrogen is produced, it is oxidized, shifting the reforming and the water gas equilibrium towards H_2 and CO_2 production[4].

  Internal reforming: $CH_4 + H_2O \leftrightarrow 3H_2 + CO$

  Water-gas shift: $CO + H_2O \leftrightarrow H_2 + CO_2$

- SOFC have a greater efficiency than internal combustion engines or more conventional power generation systems, as *Figure 1.6* shows. They have the highest operating temperatures (600-1000°C), necessary for the electrolyte material to sufficiently conduct ions. This makes it possible to tolerate lower purity fuels unlike lower temperature equivalents. Hydrogen, hydrocarbon fuels can be used and utilized by the cell to perform the reforming process. Higher kinetics resulting from the operating temperature give these systems the highest efficiencies of all fuel cells[9] especially when considering the possibility the recover the produced heat for further power generation[4]. SOFC are employed on the commercial market as stationary generators with powers ranging from 1kW to 1MW[10] along with some sporadic applications for portable devices with miniature cells[11]. Several factors impede the mass use of the technology mainly due to materials limitations[12]. Siemens-Westinghouse fabricated a 100kW SOFC showing incredible reliability successfully operating for more than 20000h without any significant degradation[5]. The high operating temperatures aggravate the cell lifetime, accelerating degradation and corrosion, while posing a significant obstacle towards safety, miniaturization and lowering costs. Greater effort is being placed towards the development of lower temperature SOFC, so called intermediate temperature cells IT-SOFC operating at 600 to 700°C, in order to alleviate such problems. A major challenge is represented by the need for a new type of electrolyte with conductivities comparable to high temperature SOFC[12]. Lower temperature also pave the way for use of metals, less expensive than ceramics, for non-electrochemical elements of the cell [5], [13].

Solid oxide fuel cell will be further explained in the following chapter with particular emphasis on the metal supported variety.

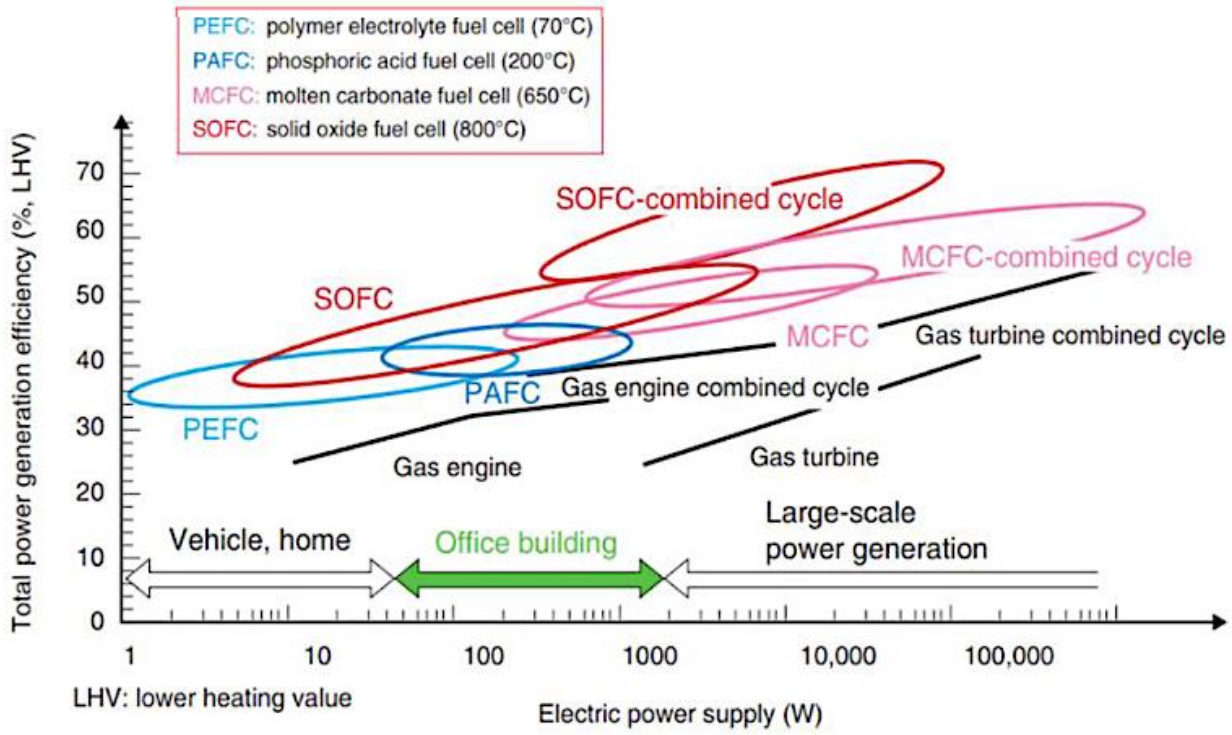

Figure 1.6:Efficiency as a function of electric power supplied by different types of fuel cell[14].

1.3 SOFC materials and classifications

In this section the components and materials that constitute a SOFC are discussed in detail.

- Electrolyte

Requirements:

- High ionic conductivity
- High electronic resistivity
- Impermeability to gas
- Chemical stability in anodic and cathodic conditions
- Mechanical stability[15]

These are ceramic materials with fluorite, perovskite, brownmillerite and apatite-type structures [16]. One of the most used electrolytes are derived from ZrO_2. Zirconia is a polymorphic ceramic: monocline, tetragonal and cubic fluorite at high temperature. By appropriately doping it is possible to stabilize the cubic structure at room temperature. Zr^{+4} ions are too small to maintain the cubic structure. Undoped zirconia is non-stoichiometric and oxygen deficient. Rare-earth elements stabilize the fluorite structure concentrating the vacancies near the Zr ions. At 1200°C zirconia works as an electrolyte with pressures ranging from 10^6 to 10^{-31} atm. Yttrium-stabilized zirconia (YSZ) has lower intervals of pressures but high ionic conductivities [12] (10^{-1} S cm^{-1} at 1000°C [5]). Along with CaSZ, YSZ is perfectly suitable for SOFC electrolyte. Their main limit is the insufficient conductivity at 600-700°C. Only 11% of Sc_2O_3-ZrO_2 is capable of exhibiting 0,15 S cm^{-1} at 800°C, it is however costly and difficult to sinter to density [17].
Another established electrolyte material with fluorite structure is represented by doped ceria, specifically GDC (gadolinium doped CeO_2) and SDC (samarium doped CeO_2). These two elements give higher conductivity lowering the activation energy[12]. The main limit of ceria-based materials is the high electronic conductivity in reducing atmospheres and when the grain structure is very fine there is also an increase in electron conductivity[18]. Ion conduction can be increased an order of magnitude by alternating different conductors like GDC/SDC with CeO_2 [12].
Perovskites ceramics are based on $LaGaO_3$ and have very high oxygen conductivity, particularly $La_{0.9}Sr_{0.1}Ga_{0.8}Mg_{0.2}O_{3-\delta}$ (LSGM) featuring conductivity some orders of magnitude higher than YSZ[19]. Under operating conditions tend to react with Ni containing anodes, this problem can be mitigated by layering it with SDC [20].

- Cathode

Requirements:

- High electronic conductivity; ≥100 S cm^{-1} in oxidizing atmosphere
- Little to no difference in CTE (coefficient of thermal expansion) with other components of the cell such as electrolyte or interconnects
- Chemical compatibility with electrolyte and interconnects
- Sufficient porosity to provide fast diffusion of O_2 gas
- High oxygen ion conductivity
- High catalytic activity in oxygen reduction reaction
- Good stability in oxidizing atmosphere[15].

$La_{1-x}Sr_xCoO_{3-\delta}$ (LSC) perovskite was the first of its kind to operate in a fuel cell [21], it was shortly followed by $La_{1-x}Sr_xMnO_3$ or LSM in short, that has since been used for conventional YSZ-SOFC working at 1000°C. This and its derivatives present tetragonal or rhombohedral lattice distortion responsible for electron transport; ionic transport is possible via oxygen vacancies instead. The simultaneous ion and electron transport attribute make the perovskites desirable for SOFC also for lower temperature applications. In this sense LSM is a pure and high electronic conductor, property lacking at lower temperatures[22].

Three steps happen at the cathode:

1. Adsorption of oxygen at the cathode active sites
2. Surface diffusion towards the three-phase boundary
3. Reduction of adsorbed oxygen and incorporation of the same in the lattice [23].

The mixed ion/electron conduction is an advantage as shown in *Figure 1.7*; if the cathode cannot

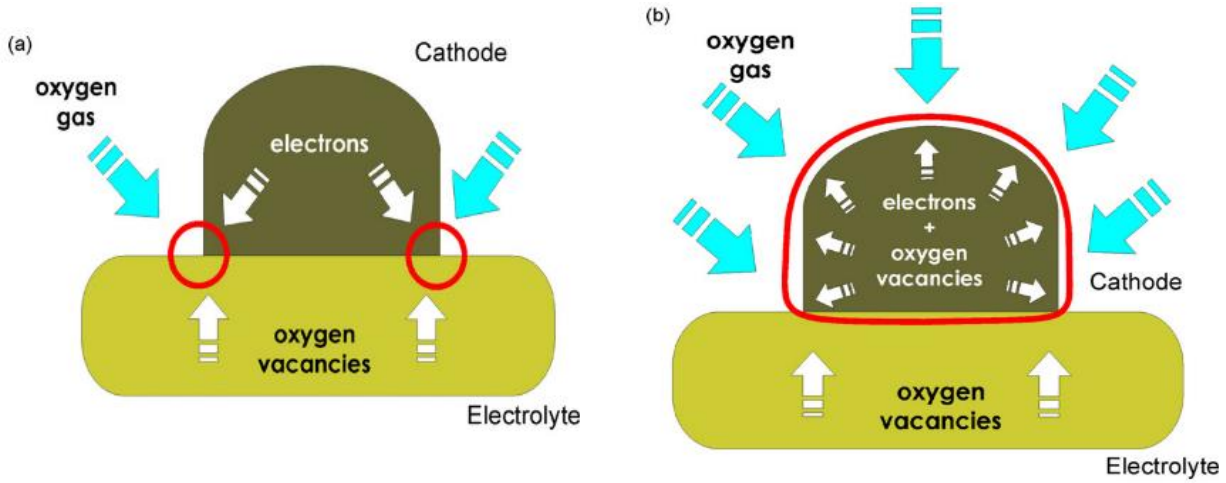

Figure 1.7 :schematic of reactions at cathode-electrolyte interface. a) pure electronic conductivity of the cathode b) mixed ion/electron conduction[9].

conduct ions, the reduction is possible only at the interface with the electrolyte, forming a single dimension triple phase boundary (TPB). However, when this possibility arises like for example by using perovskite materials, very flexible in structure by nature, ionic transport is made possible. This avoids the bottle neck created by pure electron conduction and lowers the activation potential, consequently making this material suitable for lower temperature applications. High mixed conduction is obtained by altering the chemical composition. In this case two processes in competition occur: the reaction at the TPB and the incorporation of reduced oxygen at the O_2 vacancies, which can then diffuse at the electrolyte enhancing the process [23]. In order to boost performance mixed ionic and electrical conducting (MIEC) cathodes, high surface area have been developed [7].

Particularly indicated for intermediate-temperature SOFC (600-700°C) are the perovskites belonging to the following two groups:

- $Ln_{1-x}Sr_xCo_{1-y}Fe_yO_{3-\delta}$, (LSCF) where Ln: La, Sm, Nd, Gd or Dy;
- $Ln_{1-x}A_xM_{1-y}Mn_yO_{3-\delta}$, where Ln: La, Nd or Pr; A refers to Ca/ Sr and M refers to the 3d metals, Mn excluded[24], [25].

LSCF materials, which are derived from $LaCoO_{3-\delta}$, have high conductivities (up to 650 S cm^{-1} at 800°C) but too high CTE mismatch. Some variations have more suitable expansion coefficients but insufficient conductivity [26].

- Anode

Requirements:

- High porosity for easy gas diffusion
- High electronic conductivity
- High catalytic activity
- High SSA
- Little to no CTE mismatch with the electrolyte to minimize stresses[15].

Platinum, graphite, iron oxides or other transitions metals were the chosen material in the early generation of SOFC, but they discarded due to corrosion, degradation, CTE mismatch with the electrolyte and reaction occurring only at the TPB. Ni/YSZ has now been for long time the material identified as better choice; it features good mixed ionic/electron conductivity (the former imparted by the zirconia) and the capability of promoting the reaction in all the anode internal volume. This is a cermet, YSZ is percolated with 30% Ni, an excellent catalyst for oxidation of H_2 and steam reforming. The material has some drawbacks, current tends to make it agglomerate decreasing the efficiency of reactions. Nickel has the capability of cracking higher hydrocarbon leading to carbon deposits, lowering the anode efficiency [27], [28]. For fuels different from H_2, sulphur is a common additive that gives odour, it can poison the catalyst and reduce the overall efficiency of the cell. However, the damage is reversible depending on the operating conditions[29], [30]. To address sulphur poisoning metal oxide, perovskites were developed like $Sr_{1-x}La_xTiO_3$ (LST), Y-doped $SrTiO_3$, $La_{1-x}Sr_xVO_3$ (LSV), $La_{1-x}Sr_xCr_{1-y}Mn_yO_3$ (LSCM) and pyrochlore such as $Gd_{2(}Ti_{2-x}Mo_{x)}O_7$. They show resistance to sulphur, but also a series of drawbacks like: lower electrical conductivity than Ni cermet, lower fuel oxidation, lower catalytic activity and non-compatibility with other cell components [31]–[34].
Ceria is capable to oxidize hydrocarbon fuels like methane, ethane, n-butane and it is compatible with other adjoint cell components. One con is that at low oxygen partial pressures suffers from lattice expansion and reduction of the ceria from Ce^{4+} to Ce^{3+}. Heavy doping with Sm^{3+} and Gd^{3+} could counter this effect with a slight reduction in conductivity [27]. Cu/CeO_2 composite anode obtained by wet impregnation has been demonstrated to perform direct oxidation of hydrocarbons in SOFCs at 700 and 1000°C producing just water and CO_2 [35].

- Interconnect

Requirements:

- Work as physical barrier to protect electrode from reducing environment of the fuel side
- Excellent electrical conductivity in operating conditions
- Adequate dimensional, microstructural, chemical and phase stability at about 800°C
- CTE comparable to the other cell elements at operating temperatures.

There are two main classes of interconnects: ceramic and metallic.
Ceramic interconnects are derived from semiconductor oxides fairly stable in air, increase conductivity with temperature raise and compatible with other cell components making them suitable for applications above 800°C. In fact, conductivity becomes insufficient for temperature below 600°C[36].
The most used ceramic interconnect material are perovskite $LaCrO_3$-based materials, a p-semiconductor in oxidizing atmosphere, stable in low oxygen partial pressures up to 10^{-16} atm at 1000°C [37] and with 1 $S \bullet cm^{-1}$ of conductivity[38]. The CTE is also compatible with YSZ electrolytes and compatible with other cell components[39]. By substituting La with Ca or Sr cation an improvement of conductivity ensues, if the objective is to alter the CTE, is possible to substitute Cr with Ni or Cu in order to find the best combination for the application[40].

Metallic interconnects suffer of oxidation, the oxide scale formed during the high temperature operation has inherently low conductivity contrasting the otherwise excellent one of the metals. Another problem is the continuous growth of the scale during electron conduction leading to increase of resistivity over time. Hence, a balance of conductivity and corrosion resistance must be reached[36].
Ferritic stainless steels are usually the go-to alloy: easy to process, form, relatively low cost and the bcc structure matches the other ceramic component's CTE[41]. When exposed to oxidizing and reducing atmospheres, they form an iron rich spinel oxide Fe_2O_3. Other elements present like Cr and Al get preferentially oxidized at high temperature and form a passive protection limiting

further damage[42]. While Al_2O_3 oxide is insulating, Cr_2O_3 is semiconducting up to 800°C making Cr-containing steels preferable[17], [43], [44].
There are three common features to these alloys; firstly, a high chromium content exploited as reservoir for long-term stability. Secondly manganese to ensure the formation of an outer mixed $MnCr_2O_4$ scale to reduce Cr volatility[45], and lastly rare earth elements such as La or Zr that have been shown to improve scale adherence[43]. The area surface resistance ASR is of great importance as the interconnect must provide electrical contact between the electrodes, the generally accepted value is no greater than 100 $m\Omega \cdot cm^{-2}$ during the service life[45].
Chromia scale is formed by diffusion at the interface of Cr from the alloy, causing porosity at the oxide-alloy interface and possibly spallation (scale crack) when growth becomes relevant.
Chromium vaporization is a major issue of the ferritic steels during operation, leading to poisoning of the cathode and reduction of the cell potential and its functioning[36].
The main reactions that lead to volatile species are the following:

$$2Cr_2O_3(s) + 3O_2(g) \leftrightarrow 4CrO_3(g)$$

$$2Cr_2O_3(s) + 3O_2(g) + 4H_2O \leftrightarrow 4CrO_2(OH)_2(g)$$

$$Cr_2O_3(s) + O_2(g) + H_2O(g) \leftrightarrow 2CrO_2OH(g)$$

Volatile chromium from the interconnects is reduced at the TBP and the deposited products can block electrode surface and reduce performance, a schematic example is given in *Figure 1.8* [46], [47].

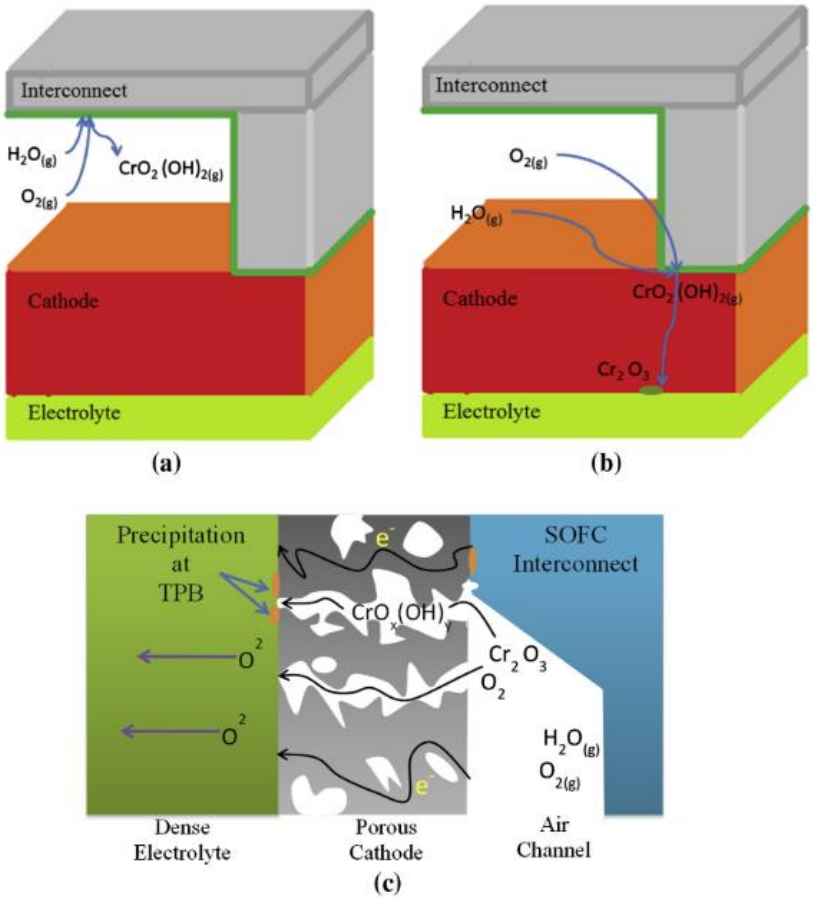

Figure 1.8:cromium poisoning representation a) at the interconnect b) at the electrolyte/cathode interface and c) at the triple-phase boundary.[36]

A possible viable solution is represented by an interconnect-coating system, and in order to correctly work it needs of:

- low Cr-diffusion and transport coefficient,
- excellent conductivity,
- chemical microstructural and phase stability,
- CTE matching with other cell components at the operating temperature,
- have high temperature strength, creep and spallation resistance,
- simple and economical manufacturing[36].

Research is focusing on $(Mn,Co)_3O_4$ spinel coating on ferritic stainless-steels[48], [49]: this system has shown to have sufficiently low ASR and excellent compatibility of CTE and electron conduction[50].

- Seals

Function of seals is to: prevent the mixing or leaking of oxidant or fuel in the stack, provide electrical insulation and mechanical bonding between the components[45].
The CTE must match with other materials of the cell, must resist operational temperatures above 700°C for long time (up to 10000h), maintaining stability over a wide range of water and oxygen partial pressures at 800°C. Further requirements are: provide low sealing temperatures (850-950°C), cause no alteration to other cell materials. Thermal cycle resistance between room and temperature constitute a necessary requirement [12], [45].
There are two types of seals: compressive and rigid. The first are composed of sealing material compressed between two surfaces that can slide relative to each other while keeping hermeticity[51]. The expansion coefficient is not critical as it is kept in compression by an external load. They can be further dived into metallic and mica-based compressive seals. During heating and cooling different CTE can cause distortion and require blocking any opening that could cause leaks. The ductility of metal coupled with the compression is the main advantage they bring to the table, enabling to close of any opening in the sealing surface during expansion/contraction cycles. Being oxidation and scaling the major problem noble metals like Pt, Au, Ag are common choices[52] although very expensive. Mica-base seals are composed un parallel sheet of silicate tetrahedra, they do not bond well to other components and are prone to leaking, but accommodate for large thermal expansion[52]–[54].
Rigid seals, contrary to compressive types, are cost-effective and achieve gas-tightness via chemical bonding to the surfaces. In this category we find glass, glass-ceramics and brazing alloys [55].
Glass-ceramics were among the first and still very relevant sealants for cell stacks: they are usually inexpensive and easily applied to sealing surfaces as paste or by tape casting, they have great wetting behaviour and provide electrical insulation. One of the most important features is the possibility to tune the formulation in order to obtain CTE comparable to the components to be joined, reducing thermal stresses.
A glass ceramic is selected based on its thermal and thermo-mechanical characteristics:

- glass transition temperature T_g
- thermal expansion coefficient CTE
- softening temperature T_s; determined by the viscosity and gives a measurement of the flow characteristics.

Usually glass softens below 1000°C, and it is unable to maintain a hermetic and durable seal due to the low viscosity. It also allows oxygen and fuel leaks. It then easily undergoes deformation due to creep and viscous flow phenomena. The formation of crystals in the amorphous phase, thus yielding a glass ceramic, gives it much higher stability; it must be noted however that full crystallization renders the glass-ceramic too brittle and non-suitable for a sealant as no plastic deformation can occur.
Chemical bonding is obtained with the formation of transitional zone where metal bonding is gradually substituted by ionic-covalent bonding; once saturation of the glass interface with

metal oxide is achieved, a strong chemical bond is formed. In case of pre-oxidized metal surface, the oxide layer dissolves into the glass at the interface, whereas in case of non-oxidized surfaces the oxide is formed by redox reaction between the metal and the glass, then dissolution of the same into the glass up to interface saturation [45].

SOFCs are produced in two main cell geometries:

- planar; easier to produce and can reach greater power than tubular configuration. A schematic representation is given by *Figure 1.9*.
- Tubular: easier gas tight seal but power limited by long current path [9].

The planar is currently the configuration with more development push. These is also the possibility for some SOFCs to operate in reverse mode, that is electrical power is used to electrolyze steam for hydrogen generation. Such devices are called solid oxide electrolysis cells (SOEC), their main advantage is the possibility to be built using the existing SOFC technology [8].

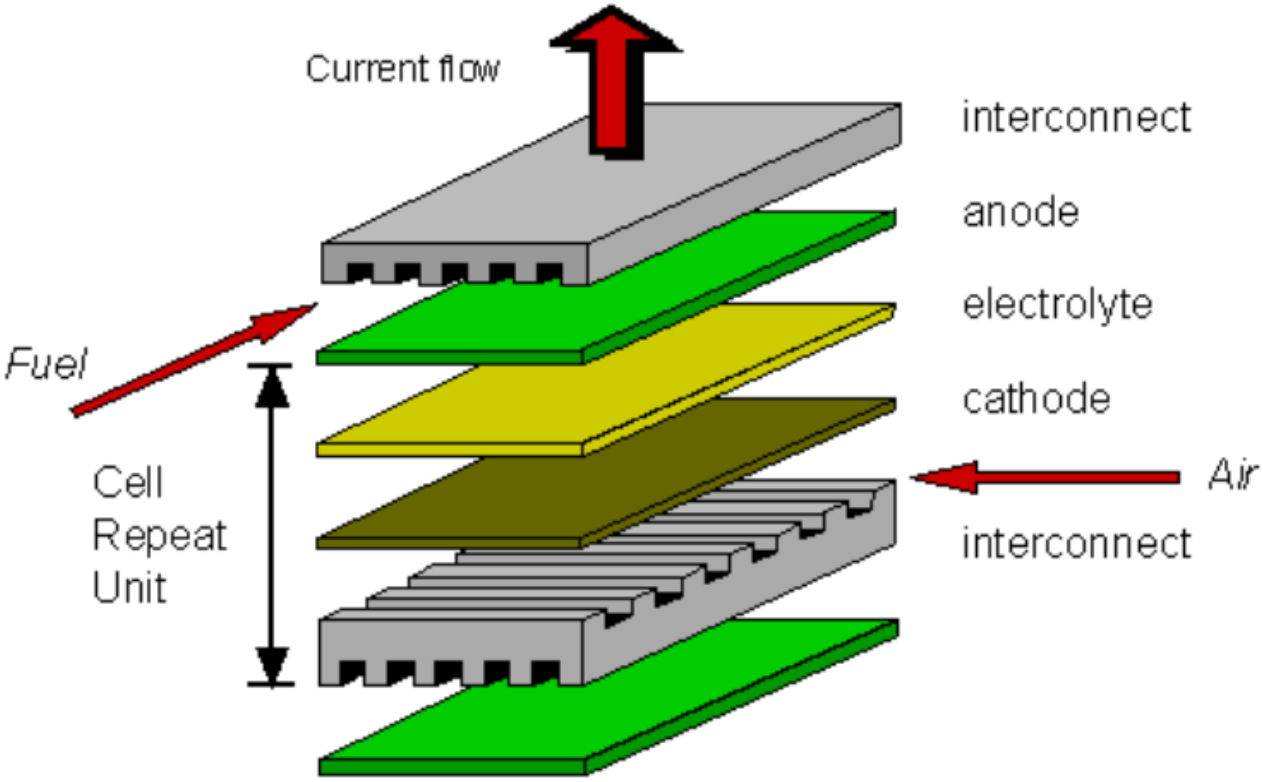

Figure 1.9:Schematic of a single SOFC cell in planar configuration.[8]

Another criterion for SOFC classification is based on the type of component that gives mechanical support; it can be electrode, cathode, anode, porous metal or interconnect supported, each with its specific peculiarity[9]. The supporting element is simply thicker in order to give mechanical integrity, thus implying larger volume of this component[12]. Electrolyte supported cells (ESCs) are the most mechanically resistant [9]; the electrolyte is between 100µm-1mm thick and this implies the use of higher temperature in order to minimize ohmic losses. CSCs (cathode supported cells) and ASCs (anode supported cells) were developed to reduce electrolyte thickness (usually below 50µm) and consequently lowering the operating temperatures[56]. For example: by using the anode as a support in YSZ-supported cells, it is possible to reduce the electrolyte thickness thus allowing lower operation temperatures, in this case going from about 1000°C of YSZ supported cell to 800°C of Ni-based ASCs. These anodes however do suffer from the cyclic oxidation/reduction of Ni and the associated volume change can mechanically damage the cell stack and lower service-life[9]. CSCs films are thin but operate at higher temperature to avoid limitations from the cathode [57], while ASCs are the most common[9]. In all these cases the supporting element is a cermet or ceramic, so inherently

fragile and expensive. MSOCs (metal supported solid oxide cells) instead are tougher [57], equally as strong as ESCs [9], the components are thick no more than necessary and the support is cheap, robust porous metal and the active layers are applied onto it [57]. Complexity consequently increases, as another component is added and the flow characteristic are greatly determined by the support itself. The details of porous metal supported cell will be discussed in the following section. Another possible support for a cell is constituted by the interconnect[56]. All these different types are schematically resumed in *Figure 1.10*.

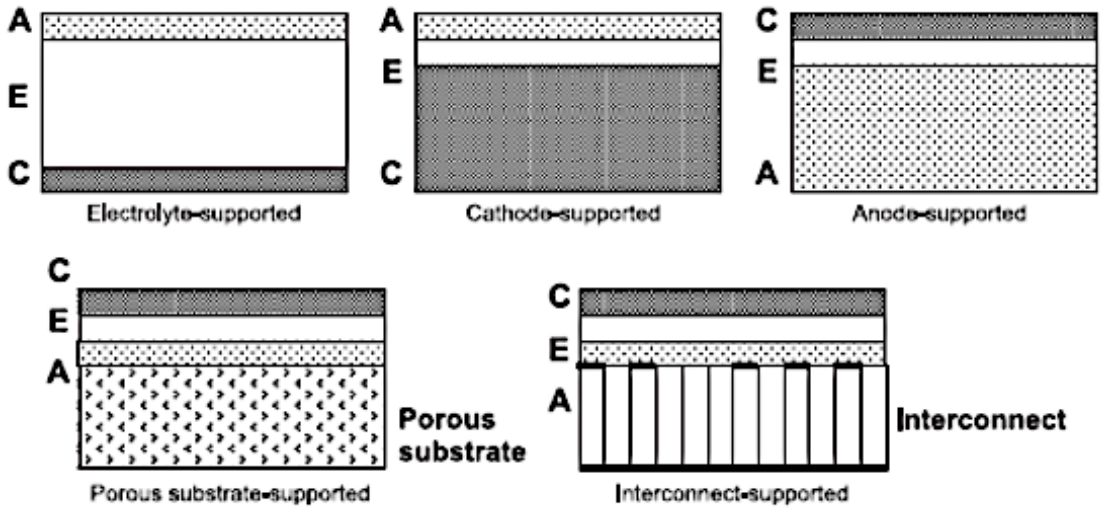

Figure 1.10: possible supports for planar SOFC cells[15].

1.4 Metal-supported SOFC

Renewable energy is a source of clean energy in order to reach goals of CO_2 reduction and limit the global warming phenomena. Electrical mobility can surely impact the 24% CO_2 emissions from transportations, but problems with power grids and the huge pressure to satisfy such high energy demand could limit the intervention.
Systems powered by SOFC at 500-800°C have remarkable fuel flexibility, to the point that the lack of H2 distribution grid is not relevant; it is possible to use a wide variety of fuels and perform the reforming. These systems are very resilient to CO and high levels can be tolerated. They combine the effectiveness of electrical vehicles with the convenience of liquid fuels. High efficiency electrochemical processes mirror the lower CO_2 emissions, and particulate-free emissions.
Metal supported SOFC are the most promising alternative to be applied as auxiliary power units (APU) in planes, trains, heavy trucks and ships or battery powered vehicles in general, as indicated by the U.S. Department of Energy (DOE). The same authority established guidelines for range-extender systems such as fast start-ups, fuel flexibility, high efficiency, high power output and long service life.
MSOC have high thermal conductivity, mechanical stability and fast start-ups resistance, very good resistance to vibrations and shocks (relevant for mobile systems), with lower material costs. Reaching the prolonged lifetime is still a challenge [58].
Rapid thermal cycling may be viewed as a condition to be avoided however, it is actually beneficial. CTE of the metal support is higher than the ceramic element of the cell. By minimizing the heating/cooling time the CTE mismatch vanishes at the operating temperature, due to creep of the metal substrate. During cooling the electrolyte is held in compression; if cooled and reheated quickly enough the electrolyte remains in compression as operating temperature is reached.

Otherwise if cooling is slow, stress in the cell is continuously relaxed and the new "zero-stress" state is reached at temperatures lower than the operation one. Quick heating and cooling are essential to maintaining the integrity at the operating temperature [57].

1.4.1 Support types

One of the metals used was Ni, but has some critical issues: great CTE mismatch with common electrolytes, low redox tolerance and susceptivity to sulphur limit its utility. Ni-Fe supports were tested, as iron and other alloying elements limit the expansion coefficient difference, yet problems associated to sulphur, coking and redox cycles remain. It is however easily obtained from Fe_2O_3 and Ni green powders sintered almost to density during the SOFC start-up. The densification opens porosity channels that allow fuel transport.
Ferritic SS are the go-to material for porous supporting applications. As with the interconnects, the main reasons are the fact they possess bcc structure, low cost, easy of forming, semi-conductive scale, CTE match to common electrolytes, and low oxidation rates.
The chromium content ranges between 10.5% to 26% maximum as it could lead to the formation of particularly brittle sigma phase. Other alloying elements include: Ni, Mo, Si, Ti, Al. The same reasoning on scale formation for SOFC interconnects holds true for metal supports, and spallation (the cracking of the oxide scale) must be avoided at all costs, as it would cause disconnection of the active area. Aluminium improves the passivating features of the scale and SiO_2 has a positive effect as it improves the adhesion between scale and metal interface. However, Al and Si must be avoided as the reduction in conductivity is too high. Manufacturing is varied: from laser drilling of a sheet yields smooth and well-defined surfaces holes and tape casting is another suitable process. In any case particular attention must be put in pore and hole sizes to allow optimal diffusion of gases in active layers.
While chromia is fairly conductive with respect to other oxides, like aluminum oxide [17], [43], [44], there is a difference in conductivity when formed in anodic condition and cathodic conditions. Oxide scale formed at the anode, in presence of moisture exhibits higher resistivity than the one formed in air. Similar results are obtained in H_2 atmosphere, hydrogen dissolution in the oxide may increase defects in the structure. It comes as a problem when temperatures reach 500-600°C such as in GDC-based (gadolinium doped ceria) MSOC[59].
Oxide growth is a strong function of the temperature, hence by lowering the temperature longer duration can be reached, for example: at 650-700°C a support can operate for 50000h before the oxide becomes so thick that spallation becomes inevitable. However, lower temperature put a limit on the maximum power output [57].

1.4.2 Electrolytes and electrodes challenges

- Electroytes

Strontium- and magnesium- doped lanthanum gallate (LSGM) has been used on Ni substrate with success and it is a good ion conductor to temperatures as low as 400°C, but tends to react with chromia and Cr vapours. GDC allows reduction to 600°C the operating temperature, since it can be sintered to full density there is no shrinkage in operation and was capable of producing a peak power of 0.5 W/m^2 at 600°C[60].
YSZ is another viable ceramic with great longevity and moderate cost, but it requires temperatures >650°C where reforming can occur. When deposited via plasma-splay near dense layers are possible, but thicknesses must be between 30-70µm to ensure the gas tightness. The required high temperatures lead to premature failure and rapid oxidation. Co-sintered YSZ is a lower cost alternative and several production methods have been tested: wet or colloidal deposition, including dip coating, tape casting, aerosol spraying and spin coating.

Manufacturing consists in the deposition of porous green layer with particles and additives, then burn-out of the latter and sintering at 1200-1400°C to full density. The resulting shrinkage is 10-25% and must be well matched to the electrolyte to avoid risk of cracks or incomplete densification. By using a wet deposition, electrolyte thickness can be reduced to 10-20μm for low resistance at 650-700°C[61]. Such cells have functioned for over 2000h, even when fuel and air are switched to perform redox cycles making this temperature interval the most desirable for ferritic SS [57].

- Cathodes

LSM and LSCF have been used as MSOC cathode by plasma spray, both for the cathode and electrolyte. Some problems arise; in order to prevent oxidation of the substrate during manufacturing, sintering must be performed in reducing atmosphere and T<900°C. Both materials require higher sintering temperatures and LSCF is susceptible to Cr vapours, whereas LSM tends to decompose in reducing atmosphere or vacuum, making it unsuitable for the role. One solution comes from an unconventional manufacturing method, that is sintering a porous catalyst-free YSZ anode with the support, electrolyte and other cell components. After the main assembly is complete, the catalyst is introduced by infiltrating salt precursors of the same in the porous cathode. This prevents the catalyst from the exposure to high temperatures; it does not bear any mechanical stress and CTE mismatch stress does not influence the assembly. Infiltrated LSM was found to be resistant to Cr poisoning after several hundred hours of operation where conventional LSM and YSZ cathode fail within a couple of hours [57].

- Anode

Initial effort in MSC production led to the use of conventional Ni-YSZ anodes from ASC and ESCs. By processing at temperatures higher the 900°C Ni is reduced causing the reduction of the TPB and coarsening of the Ni particles and consequent conduction loss. Furthermore, the metal support can assume austenitic structure from Ni diffusion, lowering the oxidation resistance. Fe and Cr diffusion in the Ni particles also cause loss of conduction and lower catalytic activity as insulating oxides such as chromia, $NiCr_2O_3$ are formed. A possible solution is the use of diffusion barrier layer (DBL) [57] about 1-2μm thick [62] at the interface, with the usual requirement of CTE match, stability, gas and electron transport capability. Ni diffusion is blocked by Cu-YSZ cermet DBL, but unsuccessful with Fe and Cr, nor prevented the coarsening of the Ni particles.
Similarly, to cathodes, anodes can also be infiltrated with catalyst. Ni can be infiltrated into YSZ anodes, but wetting is poor and coarsening rapidly decreases performance. SDC was also used as catalyst infiltration, being more stable but also less conductive. Since the catalyst forms a thin layer on the anode current must traverse it. This comes as a limit due to low electronic conductivity. Copper can be added to improve such aspect. Infiltration offers greater construction and manufacturing flexibility and paves way for higher performance [57].

- Seals

MSOFC have greater flexibility in terms of seals and due to the metal nature of the support, it is possible to use conventional brazing, welding, or reactive seals via compression or crimping. Ceramic pastes of glass seals were used only for lab demonstrations. Ceres Power achieved sealing by using solid contour porous-metal supports that is conventionally joined with laser welding or via compression gasket[63]. Active braze alloys containing Ti have also been tested, such alloys wet all the components of the cell; support, electrodes and electrolyte. Al_2TiO_5 is also added to better match the CTE of the components. Both braze and conventional metal-metal seals have proven their worth in rapid thermal cycling without leakage [57].

1.5 Latest developments

Over the last years progress has continued. Only Ceres Power was able to produce a marketable stack with technology readiness level (TLR) of 8[63]. Other consortia were able to follow different production pathways like thermal and plasma spray, tape casting, infiltration, dip-coating and sol-gel. Plasma spray has been used to produce high density electrolyte that is considered to be the main limiting step for the cost-effective production, but it is incapable to produce sub-micron layers of electrolytes and anode. Tape casting and screen printing are always possible, but present problems in deposition, densification and in manufacturing of thin films while limiting costs.
DBLs are still a common requirement for MSOFC, and have been produced with complex vacuum techniques, such as PVD, not easily adapted to mass production. These do not prevent just diffusion of Fe and Cr from the substrate into Ni anode particles, but also YSZ reaction with LSCF cathodes, inexpensive and thin depositions have been carried out, but still need development. Work on other metal substrates continues: Ni-Fe alloys can be formed in situ via reduction at the anode, they are promising for small size cells but inconvenient for redox resistance [57]. Other alloys tested involve Ni-Al and Ni-Mo. Ferritic steels (430L, Crofer alloys) are still the preferred supports and see the most efforts. 430L is the most inexpensive material that matches the CTE of the ceramics, but it is not as resistant to Cr loss as Crofer and requires conductive protective coatings [62].
Lately experiments tested the viability of symmetric structure MSOCs [64]. They are composed of two porous stainless-steel supports, YSZ electrolyte and LSM or SDCN (samarium doped ceria and nickel oxide) infiltrated-YSZ electrodes have shown considerable durability. A cross-section is provided by *Figure 1.11 (a,b)* and a detail of the infiltrated anode in *Figure 1.11 (c)*. LSM anode and SDCN (samarium doped ceria and nickel) anode cells, when subjected to 200 fast thermal and 20 redox cycles, exhibited very low impact to the performance. LSM/SDCN and SDCN/SDCN operated for 1200h at 700°C, exhibiting minimal electrical resistance increase, while maintaining seal. Polarization at the electrodes increased causing diminishing performance of the cell, LSM/SDCN cell showed faster degradation than SDCN electrode cells. Cr poisoning and coarsening were discovered to be the main failure reasons. Intimate contact between catalysts and metal support induces faster deterioration with respect to other configurations.

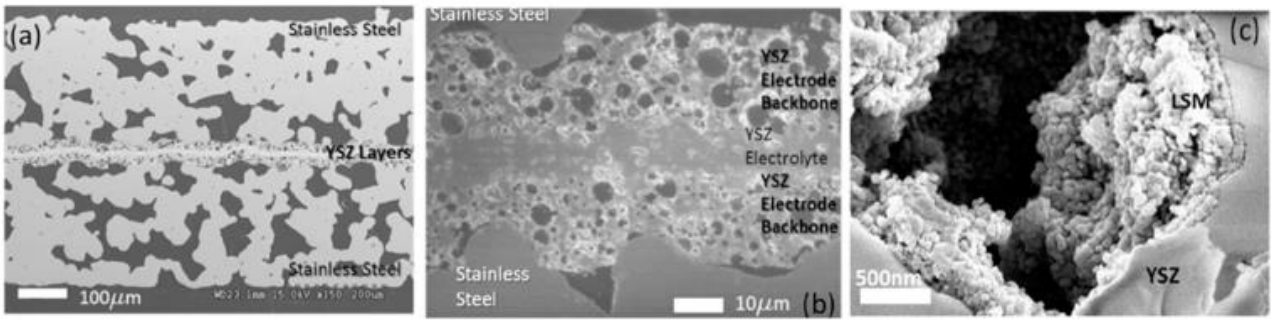

Figure 1.11: SEM image of (a,b) symmetric-structured MSOFC after sintering and before infiltration of the catalyst (c) close-up of LSM infiltrated YSZ pore [64].

The seal used was a commercial sealing Schott glass (GM31107). Glass was deposited by paste consisting of glass powder with terpineol ink onto the joining surface, heated to 200°C long enough to remove the ink and heated up to 700°C in air for 1h in order to be consolidated. The general composition is Ba, Si, Ca oxides, no Na or K in contained as it has been shown to accelerate the deposition of Cr in the cathode. After the tests yellow-green colour was found on the seal, corresponding to $BaCrO_4$, produced on the side in contact with air. It is undesirable as its formation depletes Ba from the glass and Cr from the oxide [64].
At the moment the progress toward the optimization in cell engineering as most of the materials are already well known [62]. In 2020, a pilot study focused on theoretical electrochemical simulations, electrochemical studies on cell components and manufacturing experience to produce an optimized MSOFC cell [58]. Efforts were concentrated on well-established materials and improving them first

singularly, then together. The combined results led to the realization of a metal-supported cell operating at 650-800°C, capable of a power density of 3.13 Wcm^{-2} and 0.7 V of voltage at 800°C, current density of 2.8 Acm^{-2} at 650°C, setting the record as the most powerful MSOFC and one of the highest amongst SOFCs. The results also satisfy many of the DOE requirements for mobile transportation systems[58].
The cell is so composed: LSC ($La_{0.58}Sr_{0.4}CoO_{3-\delta}$) cathode sintered in-situ to achieve best electrochemical performance, YSZ electrolyte 2µm thick, 22 µm thick Ni/GDC anode. The anode performances were increased by interposing between it and the support two Ni/YSZ 65/35 inter and base-layer. They are composed of varying fractions of powders in the 5-6µm to 15-18µm range respectively and do not take part in the reaction; their function is to increase anode volume and smoothen the porosity transition from the support to the active layer. The supports are 300µm thick ferric oxide dispersion-strengthened Fe-Cr alloy. A schematic representation of the cell is given in *Figure 1.12*. It was found to outperforms even the most advanced ASCs with 1µm thin electrolyte, proving that the approach is successful [58].

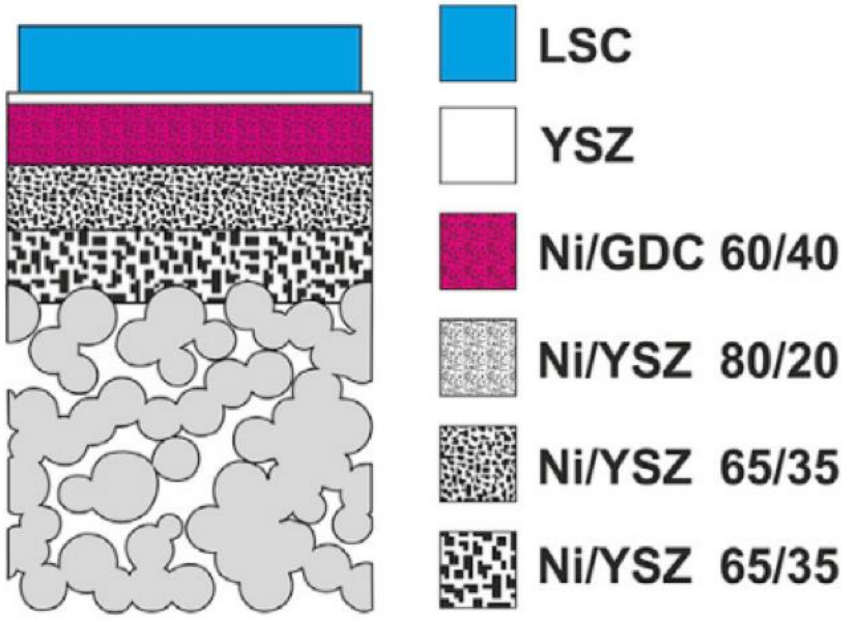

Figure 1.12: schematic section of the structure of the highest power output metal-supported fuel cell, Ni/cermet proportion given in wt% [58].

Manufacturing was carried out with a un-sintered cathode on the assembly between two YSZ frames using a glass sealant [58]. The glass sealant is composed of a glass matrix made of BaO, CaO and SiO_2 and 20 wt% of dispersed zirconia particles[65]. The initial heating melts the glass and seals the cell, at 850°C for 10h crystallization of glass and activation of cathode happen [65]. The advantage of Ni/GDC in cell anode is that coarse Ni structure with small GDC particles were proven quite resistant to coarsening and redox cycling at 700°C. Later analysis showed low Cr concentration and low oxidation, so resistant to coarsening. A new degradation phenomenon was discovered with cermet anodes when operated in electrolysis mode for dwells above several thousand hours: depletion and agglomeration of Ni from the active zone was observed, but the reasons remain unknown. Preliminary trials operated the cells for 1000h in lab-conditions with 50/50 hydrogen/steam fuel mix and show promise for long-term stability. Results show slight oxidation of metal support of pore walls and at GDC interface DBL initial oxidation of Ni particles close to barrier.
Diffusion of Fe and Cr in Ni was also reported, likely the reason for scale formation. Data suggests that diffusion already occurred during anode sintering, the DBL reduced but did not stop the diffusion [58].
In conclusion MSOFC main attractive points are the possibility to work at 600°, this temperature may not be suitable for total nor partial reforming at the anode, hence lowering efficiencies. Furthermore,

cathode activation may prove challenging. Due to redundancies like DBL substrate coatings, higher Cr content in steel for higher temperature operation can drive up the costs, so a balance point must be achieved [62], but the results obtained by Udolmsilp et al. and their approach takes the commercially viable and available MSOFC a step closer[58].

2 Porous alloy joining: state of the art

In discussing the joining of porous alloys to bulk substrates, it is useful to resume the knowledge gained until know on the subject. Apart from the work carried-out by Udomsilp et al.[58] on their high performance MSOFC in which a glass-ceramic seal was used onto porous metal substrates, no other literature was found, and the details of the afore mentioned work are still undisclosed. For this reason, this chapter is going to concentrate on glass-ceramic joining of porous to bulk or porous to porous substrates, whether metal or ceramic.

While no details of the joint were shared it is appropriate to analyse the glass sealant system used by Udomsilp et al., first described by Gross et al. [65].
The use of composite glass materials as sealants is not new and they have been used in the past for halogen lamps production and more recently for higher temperature applications. The glass matrix is obtained by double-melting and grinding in agate ball mill, in acetone a BaO-CaO-SiO_2 glass (exact composition show in *Table 2.1*) to median particle size of 10-13µm.[65] The so obtained Glass H is relatively low in silica, resembling an invert glass, the additives lower the viscosity and improve wetting.

Table 2.1: Composition of glass H (adapted from[65]*).*

Component	**BaO**	**SiO_2**	**CaO**	**Additives**
%wt	48.2	29.8	6.1	Al_2O_3, B_2O_3, V_2O_5, ZnO

The ceramic filler consists in monocline zirconia ground to medial particle size of 15µm, it was added and mechanically agitated to the glass in 10, 20 and 30 %wt to verify which formulation yielded the best CTE results and microstructure on a test joint; a sandwich of ferritic stainless-steel plates and glass. The steel is so composed: 23 wt% Cr, 0.4 wt% Mn, 0.16 wt% Ni, 0.12 wt% Al, 0.1 wt% Si, rest being iron. The sealant powder was formed into a paste and deposited on the polished and cleaned plate to the circumference. The 25 cm^2 sandwich was loaded with 400g, heated in resistance air furnace. The heating rate is 2 °C/min to 800°C for 20 to 60h, a second treatment at 850°C for 20h and a dwell of 60h at 800°C, the cooling rate is identical to heating.
In DTA tests the crystallization of the matrix represented by the peak at 780° effectively disappears even with just 10% zirconia, and the softening temperature shifts at progressively higher temperatures; therefore, the filler suppresses the crystallization even with small amounts. In dilatometry tests the CTE shows a shift at 550°C at 10% and moves to 640°C for the higher filler concentration. Particularly interesting is the decrease of CTE of the composite when compared to the unloaded glass; this can be explained by the lower expansion coefficient of monocline zirconia with respect to the glass. However, the lower shift in the curve belonged to the 20% ZrO_2 composites whereas comparatively higher values are from 10% and 30% samples, clearly visible in *Figure 2.1*. This finding still has no explanation. Samples sintered at a slightly higher temperature for shorter time showed a glassy behaviour.
From cross-section observations different composites yielded different joint thicknesses, the greater the content of filler the greater the thickness. Glass H joints were subjected to 2°C/min heating/cooling and 850°C for 10h; the resulting microstructure showed a network of needle-like crystals of Celsian, Ca-Ba silicates and binary Ba silicates.
In the composite joints, zirconia does not perform as a nucleating agent, the crystals grow un-oriented. A comparison of the microstructure obtained with different heat treatments for 20% ZrO_2 composite is exemplified in *Figure 2.2*; in *Figure 2.2 (a)* the bright cloudy particles are zirconia particles, no nucleation on the surface is present. In *Figure 2.2 (b)* greater crystallization led to the predominant formation of Ba silicates (light grey). *Figure 2.2 (c)* shows a glass matrix similar to *Figure 2.2 (a)* and contrary to before, needle crystals originate from the zirconia particles. Overall the adhesion is good regardless of the filler percentage, the joints were also tested for He leakage and were all gas-

tight. The low crystallization rate imparted by the filler particles could potentially lead to self-healing of small-cracks [65].

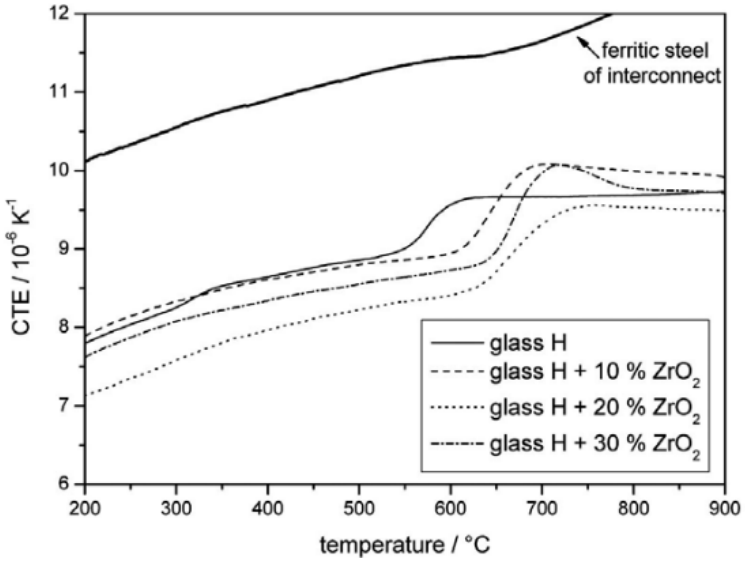

Figure 2.1: Thermal expansion coefficients as function of the temperature on sintered glass H samples at 850°C for 60h and a comparison of ferritic steel [65].

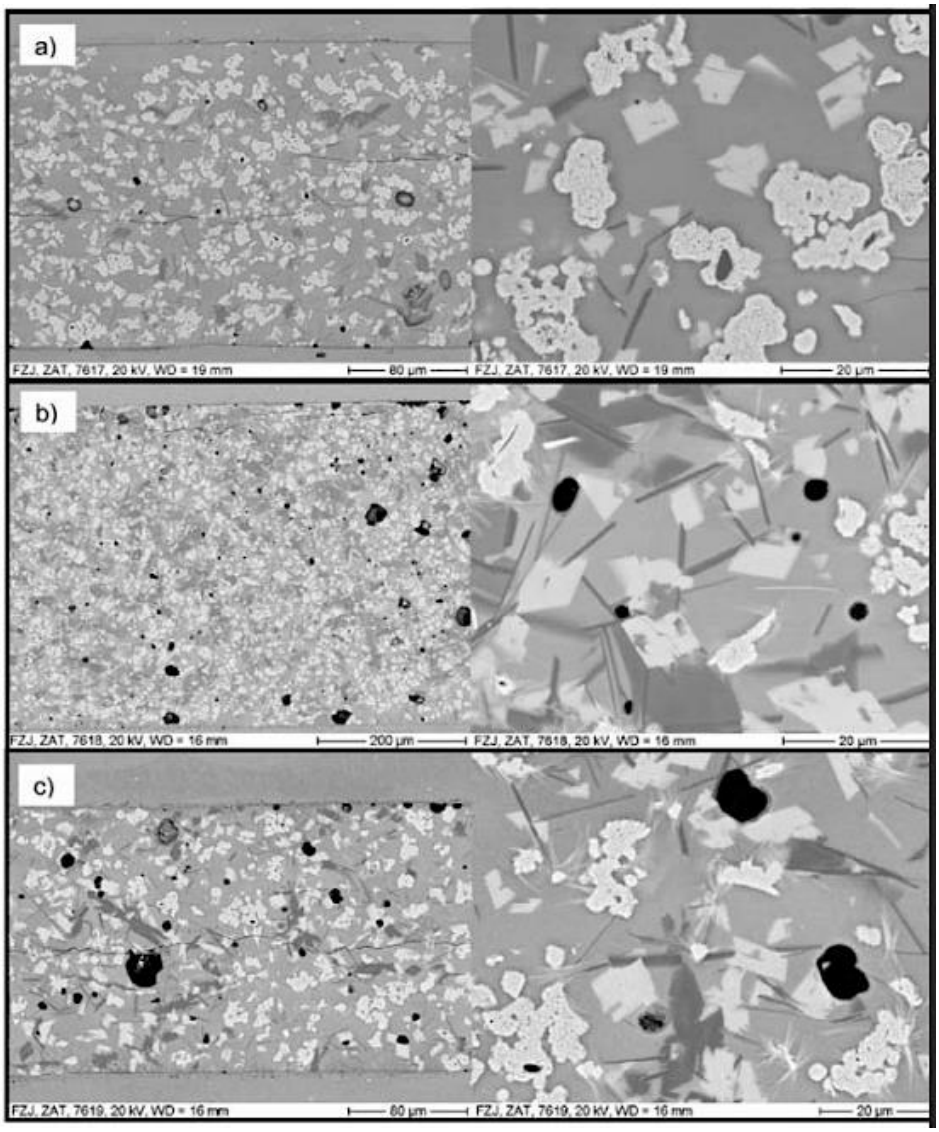

Figure 2.2:SEM images of glass H+20% zirconia after different heat treatments, a) 20h at 800°C, b) 60h at 800°C, c) 20h at 850°C then 60h at 800°C. A magnification is shown on the right for each image.[65]

2.1 Porous to dense ceramic joining

Several records of dense to porous ceramic substrates joining exist. Alumina and silicon nitride substrates were joined with different glass-ceramic systems, the major results are explained in the following section.

2.1.1 Alumina substrates

A study focused on joining of porous alumina tubes to a bulk alumina sleeve using a glass-ceramic, a CAS-based system adequately modified to lower the crystallization temperature in order to avoid alteration of pore distribution and increasing wettability. The glass system composition (in %wt) is 20.7% CaO, 13.3% Al_2O_3, 55% SiO_2, 5% TiO_2, 4% Li_2O, 1% Na_2O, 1% K_2O. Titanium is added to promote crystallization and the rest of the additives (Li, Na, K) for better wettability. After melting and subsequent zirconia ball-milling the glass was sieved to 10µm. Discs of bulk glass were cut and not milled, but laid on the porous alumina in a muffle furnace to evaluate the penetration of the glass after 20 min at each temperature. Infiltration of the glass increases as the temperature raises,

indicating that is possible to improve wettability (*Figure 2.3* shows penetration depth δ varying with treatment temperature). Crystallization temperatures ranged from 790 to 1120°C.

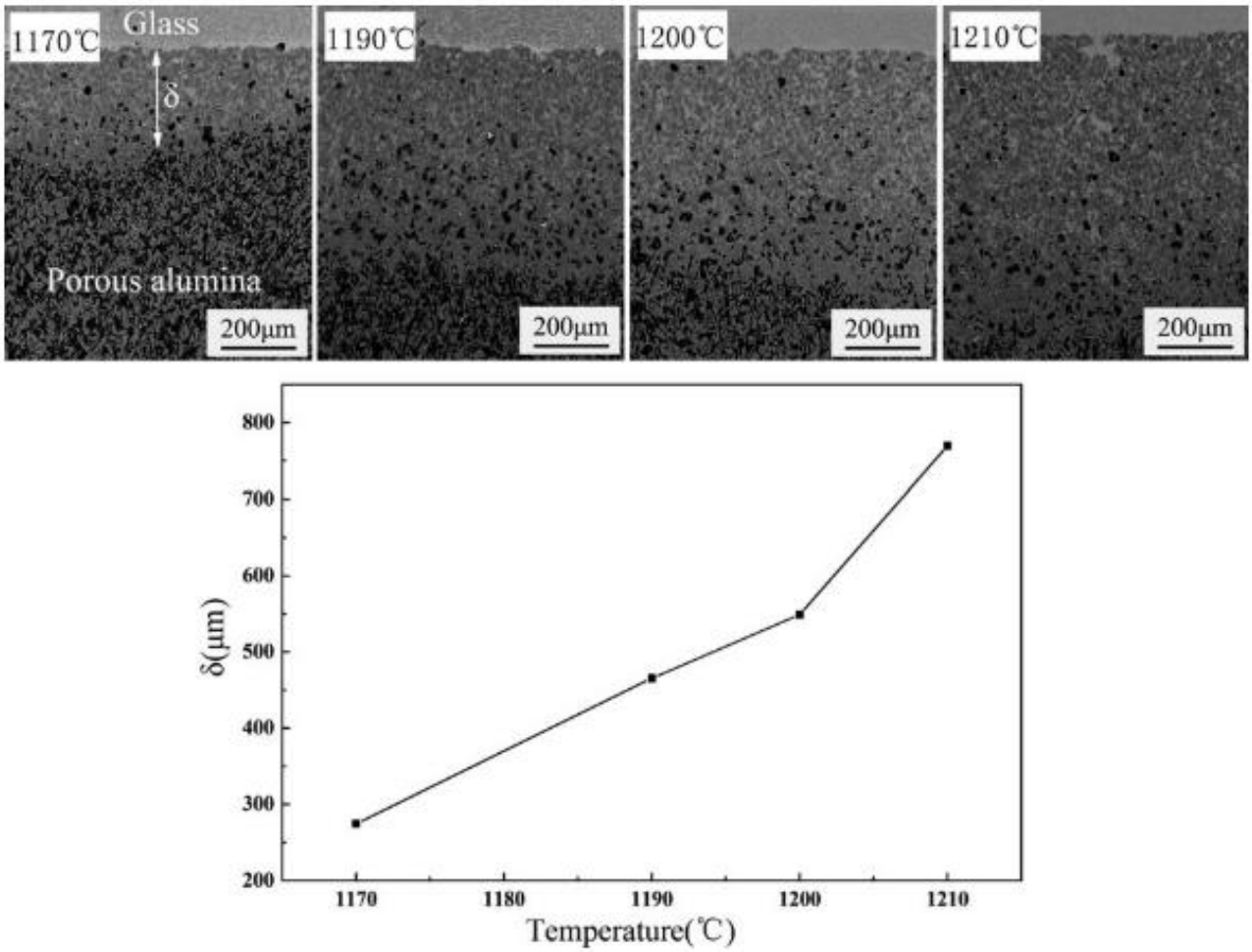

Figure 2.3: penetration depth of CAS glass in porous alumina as a function of the treatment temperature and corresponding SEM images of the interface[66].

The joints were less resistant to thermal shock if β-spodumene ($LiAlSi_2O_6$) was present, such samples withstood about 34 shock cycles. In contrast, less glassy joints that presented $CaTiSiO_5$ or $CaAl_2Si_2O_8$ phases showed no cracks and were able to withstand double the cycles.

Higher joining temperature has shown to reduce the crystallinity at the interlayer (the portion of glass between the dense and porous alumina), demonstrated by *Figure 2.4*. This is due to the dissolution of $LiAlSi_2O_6$ and $CaTiSiO_5$ formed at temperatures lower than 1170°C and slow heating rate 15°C/min. In addition, quench rate is very influential to the crystal phase formation; for quick quench rates (50°C/min) the glass interlayer assumes disordered structure and becomes glassy above the crystallization upper limit of 1210°C. Lowering the heat rate to 15°C/min increased crystallinity as *Figure 2.4* shows.

Alumina dissolves in the glass upon wetting, changing the composition at the interlayer; $CaAl_2Si_2O_8$ is a direct consequence of this and its quantity is proportional to the dissolution. Direct quenching prevented the formation of $LiAlSi_2O_6$. This microstructure difference also explains the worse thermal shock performance of these joints. The lower CTE of $LiAlSi_2O_6$ causes high stress concentration between the interlayer, where its most present, and the rest of the glassy joint.

Interlayers with $CaTiSiO_5$ or $CaAl_2Si_2O_8$ showed greater toughness and strength due to a minimal difference between the crystal and glass CTE [66].

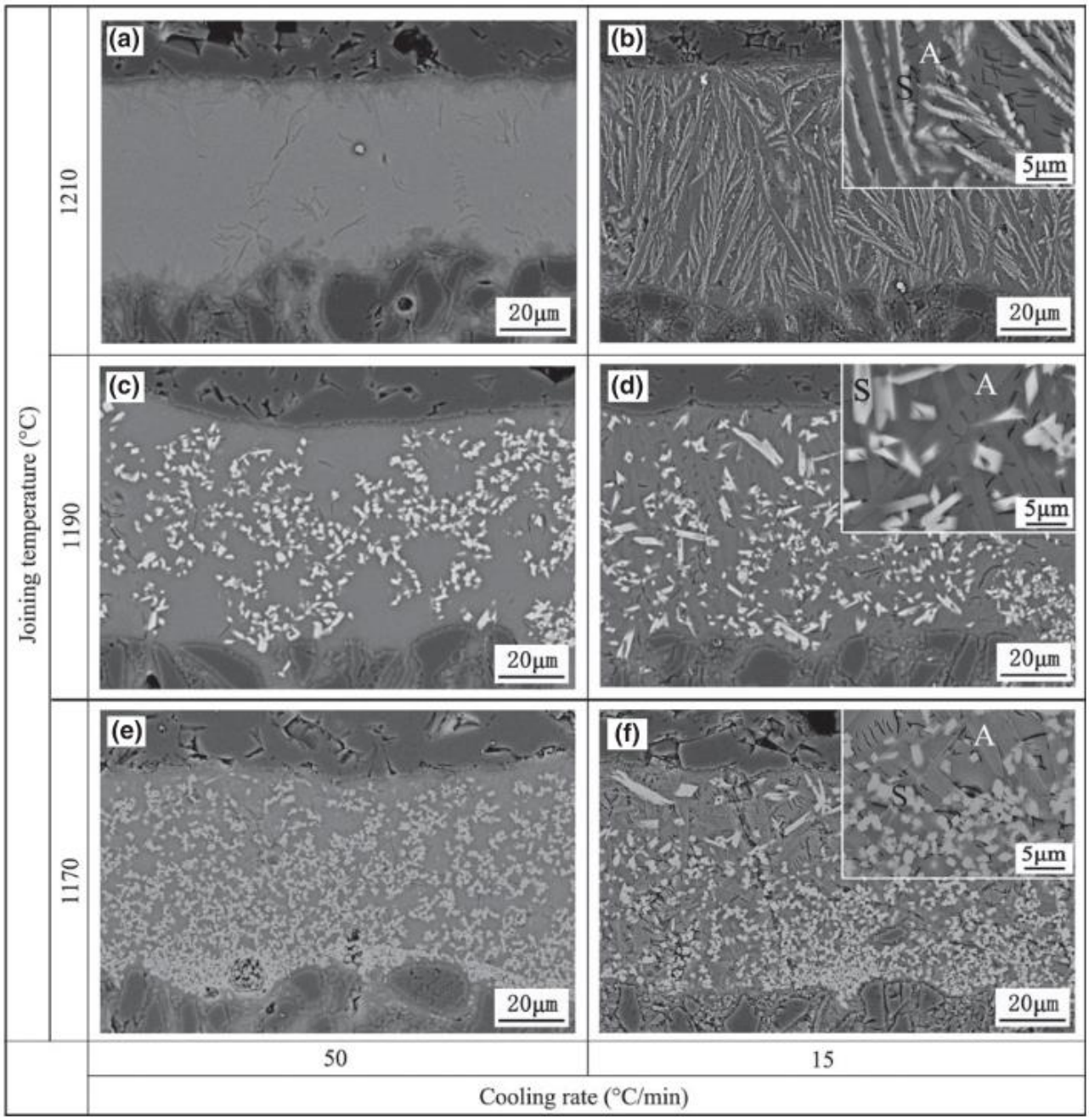

Figure 2.4: SEM images of different microstructures at the interlayer of a porous/CAS glass-ceramic/dense alumina sandwich at varying joining temperatures and cooling rates [66].

2.1.2 Silicon nitride substrates

Three different glass-ceramic systems were evaluated for efficient joining of a porous and dense silicon nitride namely Y/Yb-SiALON glasses with silicon nitride powders, LMAS and CLAS-based systems. All porous substrates featured 47% open volume and for the last two systems the substrates are obtained from the same manufacturer.

- Y/Yb-SiALON

Porous Si_3N_4 and dense Si_3N_4 were successfully joined with a RE_2O_3 (RE = Y or Yb), Al_2O_3, SiO_2, and α-Si_3N_4 powders glass mixture. The composition is shown in *Table 2.2*. For temperatures of 1550,

1600 and 1650°C for 30min, these silicon nitride powders in part transformed into β-SiAlON, in part dissolved into the glass matrix forming oxynitride glass, resulting in a β-SiAlON/glass composite.

Table 2.2:Chemical compositions of the Y-SiALON and Yb-SiALON glass solders in %wt [67].

Glass Solders	Y_2O_3	Yb_2O_3	Al_2O_3	SiO_2	α-Si_3N_4
Y-SiAlON	44.5	-	10.5	10.3	34.7
Yb-SiAlON	-	58.3	7.9	7.7	26.1

The joining section comprises of: diffusion zone, infiltration zone and a seam zone. The diffusion zone is located on the dense silicon nitride, while the infiltration occurred porous side. The seam is between the last two, it is also where the α-Si_3N_4 dissolved and formed a β-SiAlON/glass composite. A temperature increase showed that the developed liquid oxynitride glass quickly bonded the substrates and the capillarity of the porous substrate gave its contribution. The glass had uneven distribution due to the infiltration in the porous substrate. The infiltration contributed to the transformation of the initial α-Si_3N_4 to β-SiAlON, while in the seam the remaining glass turned into a β-SiAlON/glass composite. *Figure 2.5* shows the microstructures obtained with YSiALON glass, the infiltration zone contains a white YSiALON phase embedded with fine-grain β-SiAlON and β-Si_3N_4. For higher temperature the white phase diffused into the porous Si_3N_4 filling the pores formed at lower temperatures. The diffusion zone consisted in glass diffusion along the grain boundaries of D-Si_3N_4. The β-SiAlON formed in-situ contributed to the strength of the joint. In 4-point bending test the Y-SiALON and Yb- SiALON obtained 103MPa and 88MPa and the joint had a respective contribution of 73% and 62% of the porous Si_3N_4 strength.

Excessive infiltration however could be responsible for the pores at the P-Si_3N_4 and consequently weakening the joint [67].

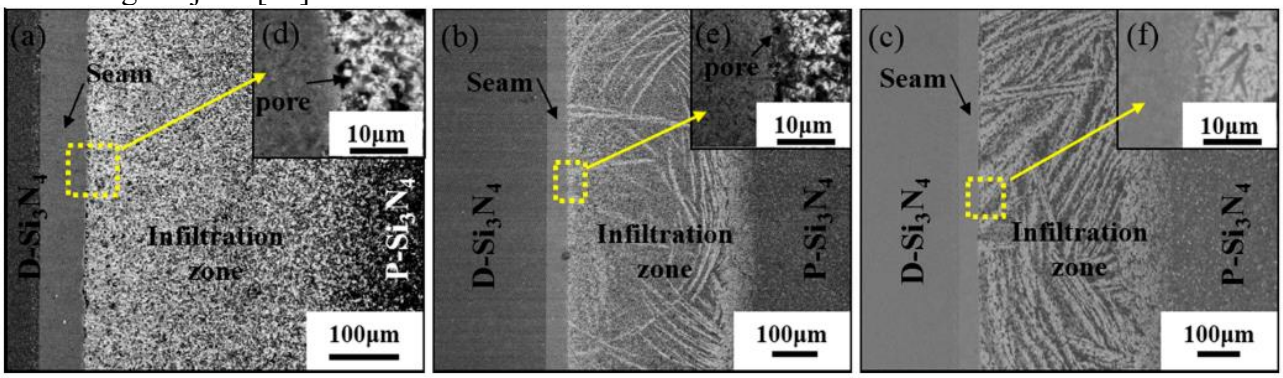

Figure 2.5: SEM images of P-Si_3N_4/ Y-SiALON/ D-Si_3N_4 joints at (a,d) 1550°C, (b,e) 1600°C and (c,f) 1650°C for 30 min[67].

- LMAS

Similar P-Si_3N_4 and D-Si_3N_4 were joined using a novel glass ceramic belonging to Li_2O-MgO-Al_2O_3-SiO_2 (LMAS) system with the objective to study the glass/ceramic interface, determining the influence of the joining temperature on the microstructural evolution and the shear strength at varying temperatures.

Boron oxide was not added, as it suppresses glass devitrification; it attracts cations on the network and forms bridging oxygen reinforcing the network itself. Li_2O however, when added in quantities > 5 wt% showed to enhance the crystallization ability of a glass ceramic system. The glass exact composition is 7% Li_2O, 10% MgO, 29% Al_2O_3 and 54% SiO_2 (percentages in %wt). The P-Si_3N_4 has 47% open-porosity and average pore radius of 253nm, the D-Si_3N_4 was subject to pre-oxidation at 1200°C for 5h to form a SiO_2 superficial layer in-situ to improve bonding. A compressed powdered LMAS glass sheet of 400μm was place between the substrates under 10 MPa load and heated in inert gas (N_2) tubular furnace to different temperatures 1300-1360°C for 10 min with a heating rate of 5°C/min and slow cooling. The performed wetting tests, of which the results are shown in *Figure 2.6 (a,b)*, showed good results and thermomechanical compatibility on both dense and porous substrates.

The latter first saw the infiltration when in contact with molten glass and then the reduction of the contact angle up to a stable value of 27° at ~600°C. The liquid glass infiltrated the P-Si_3N_4 much further along the surface than the edge of glass droplet as demonstrated in *Figure 2.6 (b)*. This supports the fact that the porous surface is different than the dense as it exhibits a much lower contact angle due to the roughness itself. D-Si_3N_4 gave an equilibrium contact angle at 1350°C of 25°C, validating the great wettability of both surfaces. Some porosities appeared at the edge of the glass-ceramic edge, possibly due to residual trapped gas. The main crystalline phases formed are β-spodumene and submicron size spinel ($MgAl_2O_4$) phase, in the interlayer they constitute a networks structure. The *Figure 2.7 (a)* show a cross-section of the joint, here the seam or interlayer zone is evident. At the D-Si_3N_4/glass interface B indicates the major β-spodumene and A the spinel (*Figure 2.7 (b)*), in Figure 2.7 (c) the glass-ceramic/Si_3N_4 composite constituting the infiltration zone. Point C in *Figure 2.7 (d)* shows the sintering product of silicon nitride and intergranular phase $Y_{4,67}(SiO_4)_3O$, originated from the Y_2O_3 used as sintering additive.

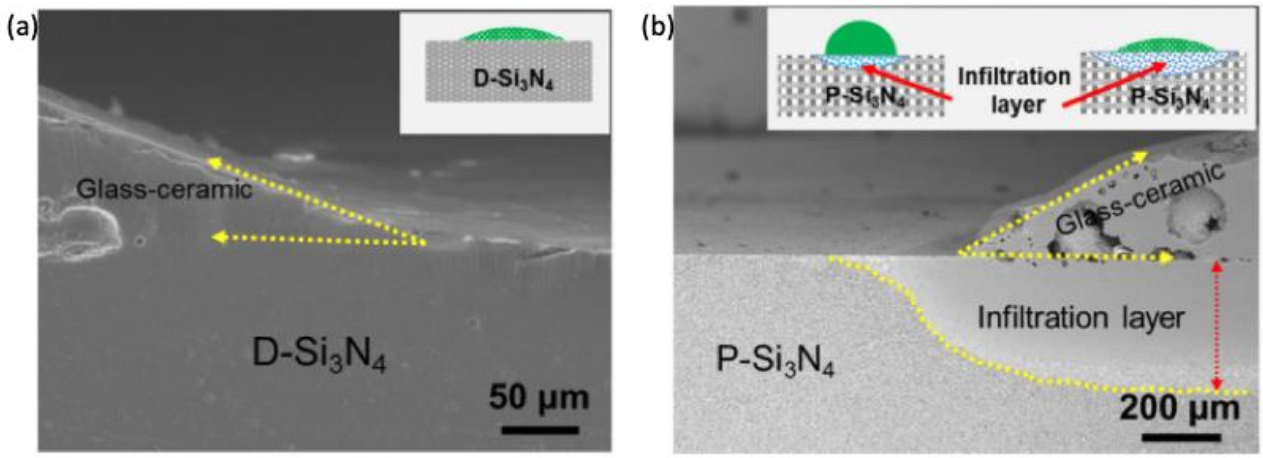

Figure 2.6:SEM micrographs of the glass LMAS doplet cross-section and schematic representation of (a) dense and (b) porous silicon nitride obtained at 1360°C [68].

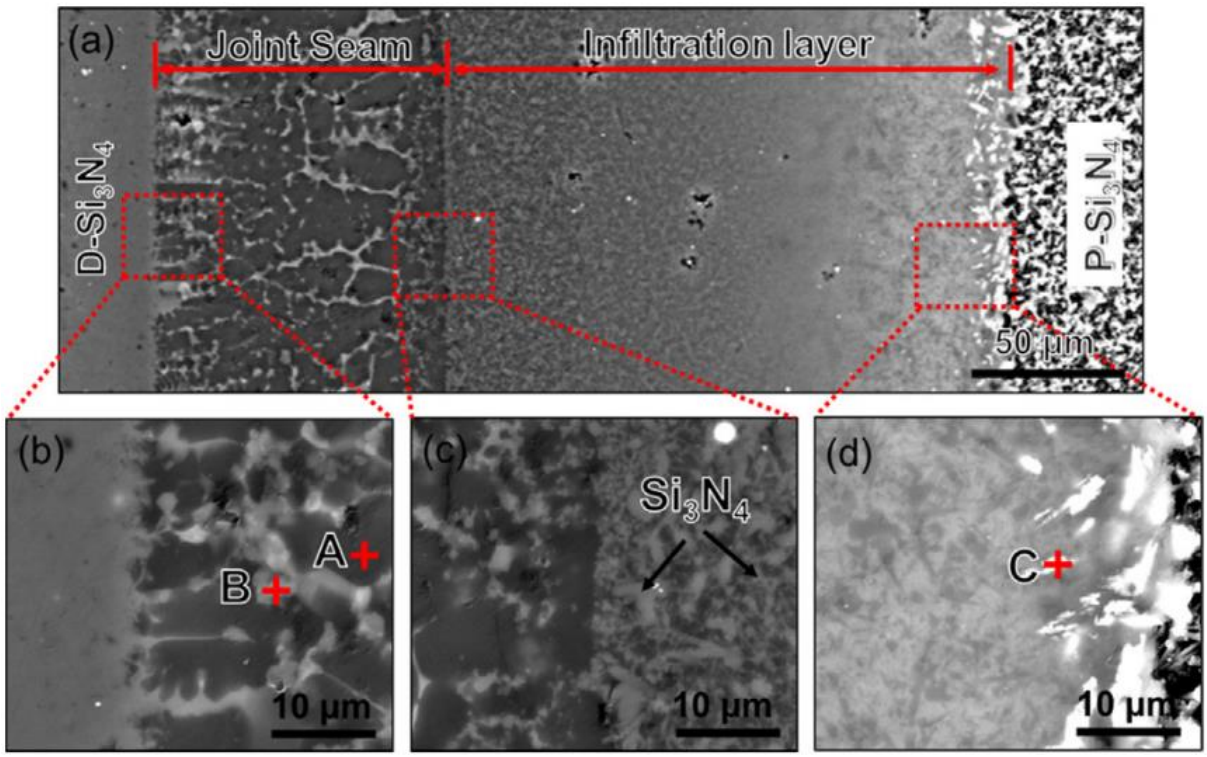

Figure 2.7:Back-scattered electron (BSE) image of P-Si_3N_4/ LMAS glass-ceramic/D-Si_3N_4 joint cross-section obtained at 1340°C. (a) integral joint (b) D-Si_3N_4/glass-ceramic interface (c) glass-ceramic/P-Si_3N_4 interface (d) infiltration layer[68].

At 1340°C the infiltration layer is 200µm deep, performs like a transition structure possibly increasing the bonding strength. The infiltration layer glass and rod-like Si_3N_4 exhibits increased mechanical properties as elastic modulus and micro-hardness. With the increase in temperature the infiltration depth increases and seam thickness decreases; this behaviour is dependent on the decreasing viscosity of the glass with the temperature. When infiltration is too high, it leads to the formation of porosities, as glass starts to lack in the joint area.
Good wetting influenced positively the formation of the infiltration layer in the porous substrate.
The consequent shear resistance was excellent, reaching values of 112 ±10 MPa at room temperature for joints sintered at 1340°C. It is now however directly related to the infiltration depth, with temperatures >1340°C the shear strength decreased as *Figure 2.8 (a)* demonstrates. The porosities formed at the seam interface caused by excessive infiltration is the cause of the lower strength values. *Figure 2.8 (b)* indicates how the increase of temperature reduces the shear strength to 87 ± 13 MPa at 850°C and still exhibited good strength at 1000°C with 25 ± 13 MPa, thus indicating great heat resistance of the joints [68].

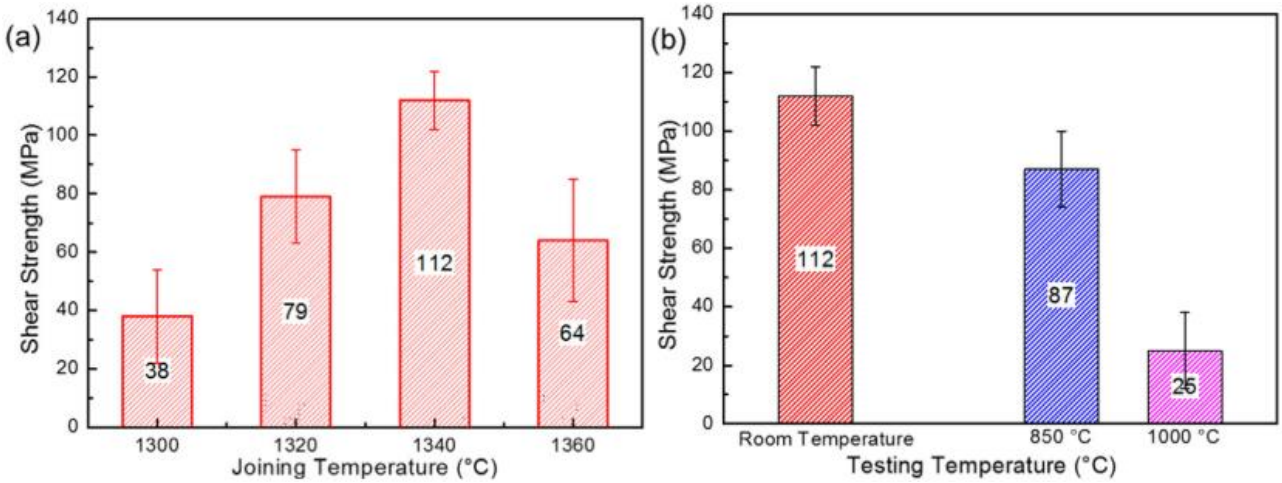

Figure 2.8: LMAS glass-ceramic P-Si_3N_4/D-Si_3N_4 shear strength of joints(obtained at 1340°C for 10min) function of the temperature and (b) shear strength as a function of the temperature[68].

At 1300°C bonding temperatures the samples broke due to void present at the glass-ceramic/D-Si_3N_4 interface (*Figure 2.9 (a)*). With slightly higher temperatures (1320 and 1340°C; *Figure 2.9 (b,c)*) the fracture propagated into the infiltration layer breaking the porous substrate, when the bonding temperature reached 1360°C the samples failed at the porosity located at the seam, evident in *Figure 2.9 (d)*, likely to excessive infiltration.

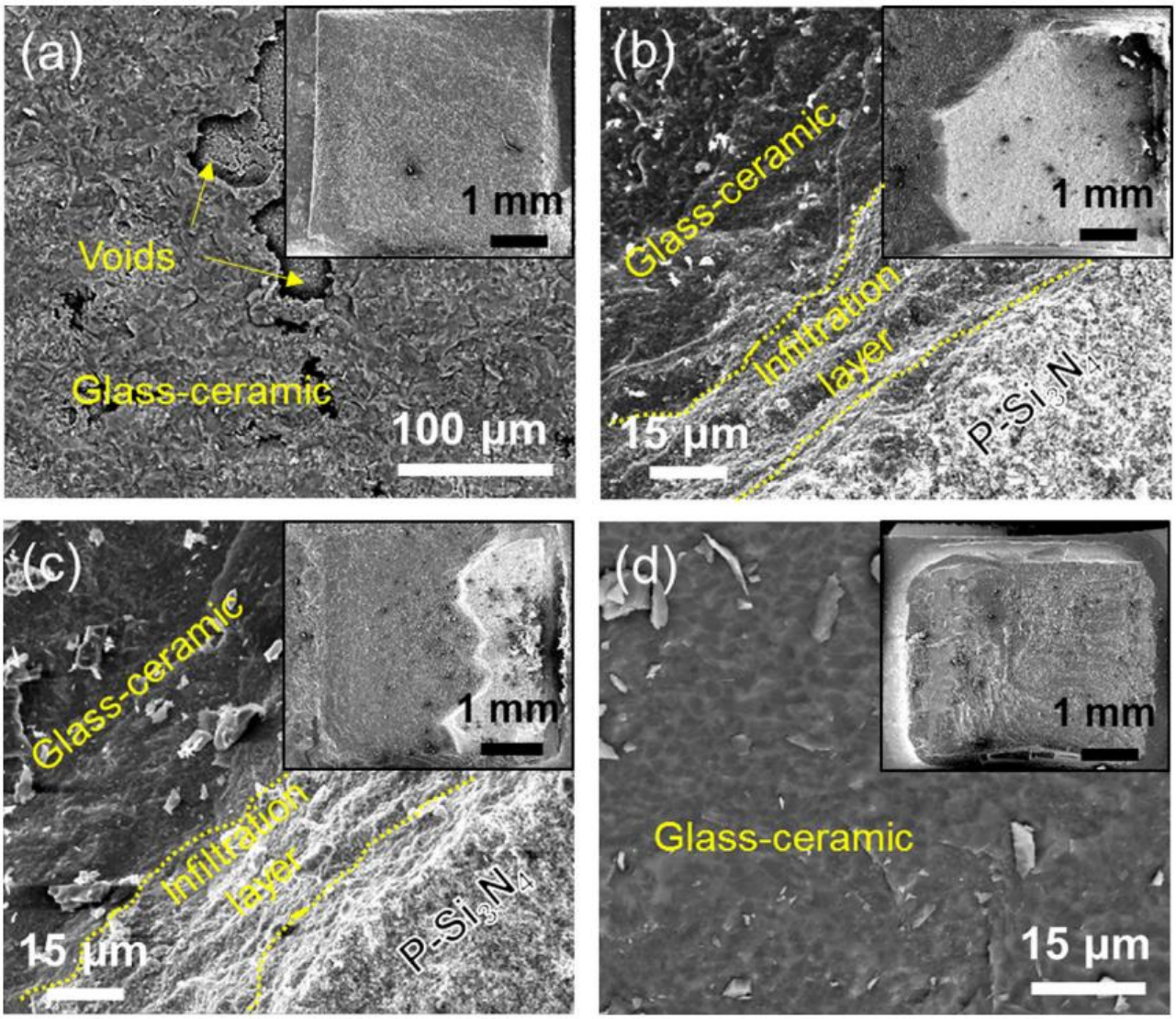

Figure 2.9: LMAS glass-ceramic P-Si_3N_4/D-Si_3N_4 joints fracture micrographs for different joining temperatures: (a) 1300°C (b) 1320°C, (c) 1340°C, (d) 1360°C [69].

- CLAS

The same two substrates, namely P-Si_3N_4 and D-Si_3N_4 were tested with a CaO-Li_2O-Al_2O_3-SiO_2 (CLAS) system the verify the joining efficacy, CTE mismatch and mechanical strength, analogously to the work carried out with the LMAS system. Some differences in the wetting test from the previous LMAS system were found, like measurements atmosphere and pressure used to compact the glass powders (now being 8MPa). Tests were carried out in 10^{-3} Pa vacuum furnace and the resulting contact angle were 45° and 36° for P-Si_3N_4 and D-Si_3N_4 respectively, indicating good wettability.
Joining temperatures >920°C were found to be more suitable; to allow the formation of anorthite ($CaAl_2Si_2O_8$) along with $CaSiO_3$ and $LiAlSi_2O_6$, bringing the CTE to 3.5 x 10^{-6}/°C, closer to the two substrates (3.1 x 10^{-6}/°C for P-Si_3N_4 and 3.0 x 10^{-6}/°C for D-Si_3N_4). The joints were obtained as before mentioned, by interposing between the substrates a glass paste held together by organic glue. The joining temperatures varied between 1080-1120°C for 20 min, the cooling rates where varied between 5 and 50°C/min. An initial heating step to 300°C, at 10°C/min for 30 min was essential to decompose and evacuate the glue.

For 1080°C treatment the joint presented a significant number of voids, likely due to the higher viscosity, that gradually disappeared as the temperatures increased and viscosity diminished. The interlayer thickness also diminished as expected.
A schematic representation of the distribution and morphology of the crystalline phases in the joint is given by *Figure 2.10*. The joining evolution can be divided, analogously to the LMAS system joining, in the same two phases: melting and infiltration of the glass and crystal precipitation. In the interlayer three phases were found: $CaAl_2Si_2O_8$, $CaSiO_3$ and $LiAlSi_2O_6$. $CaAl_2Si_2O_8$ increased with the treatment temperature, reducing Al for the $LiAlSi_2O_6$ promoting the formation of greater amounts of $CaSiO_3$.
Differently from the LMAS glass system, the infiltration layer presented two different layers. In layer I almost no pores were present, EDS analysis showed that the rod-like phases were β -Si_3N_4 grains. In layer II an intergranular phase of composition $Y_{4,67}(SiO_4)_3O$ was detected.

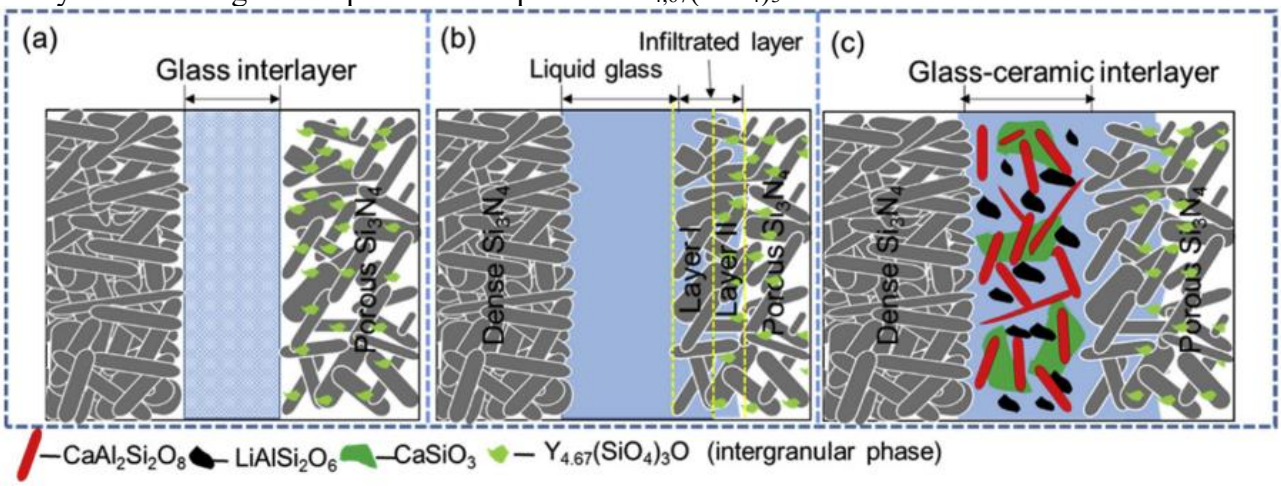

Figure 2.10:Schematic representation of CLAS glass-ceramic P-Si_3N_4/D-Si_3N_4 joints structure, morphology and crystalline phase distribution [69].

Slower cooling allowed for greater crystal growth as demonstrated in *Figure 2.11 (a)* and *(d)*, for 50°C/min values the glass remain amorphous and experienced cracking due to excessive thermal solicitation.
Maximum shear strength obtained was lower than the LMAS system, reaching 45MPa for a 1100°C joining at 5°C/min. Fracture occurred mainly within the porous silicon nitride side, stating that great joining strength of the P-Si_3N_4/CLAS glass-ceramic/D-Si_3N_4.
Analogously to the LMAS system the shear resistance increased with the treatment temperature then declined as *Figure 2.12 (a)* shows. The improvement of the shear resistance up to 1100°C was mainly attributed to the reduction in voids, while the dip in performance at 1120°C could be explained by the greater amounts of $CaSiO_3$ that has much greater CTE than any of the other joint phases. Excessive heating rates showed a negative impact on strength as shown in *Figure 2.12 (b)*.
The best joining and mechanical performances were obtained for 1100°C heat treating and 15°C/min heating rates [69].

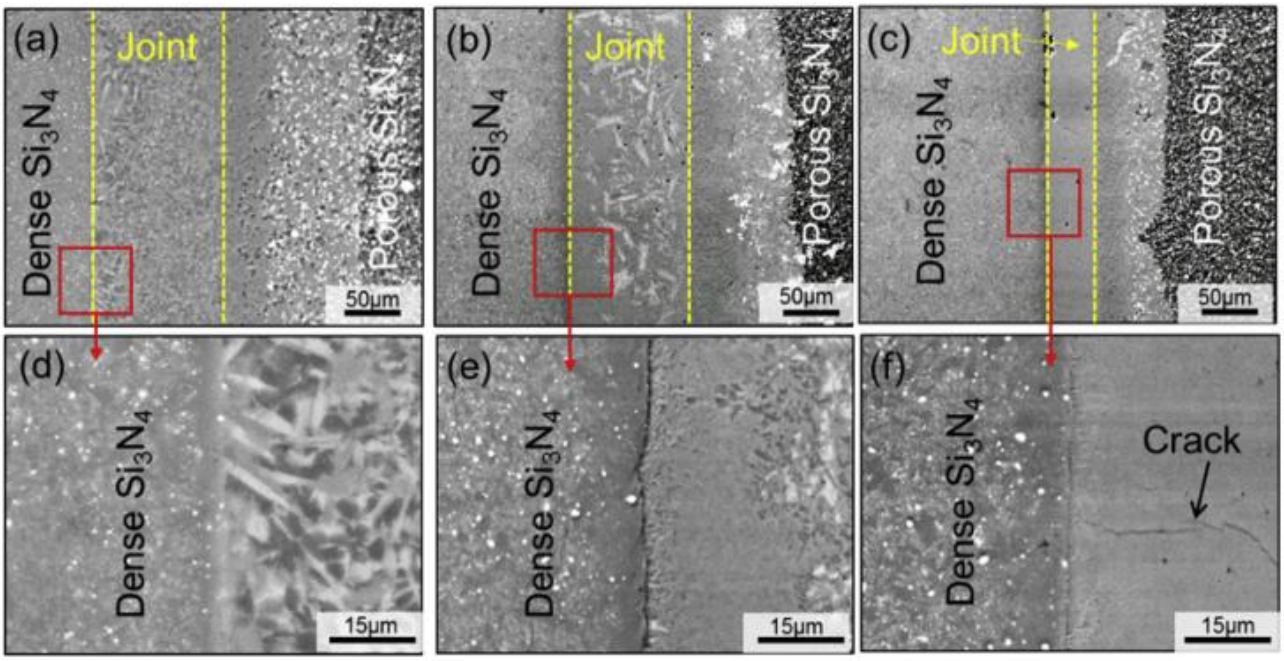

Figure 2.11: CLAS glass-ceramic P-Si_3N_4/D-Si_3N_4 joints microstructure bonded at 1100°C with different cooling rates: (a,d) 5°C/min; (b,e) 15°C/min; (c,f) 50°C/min [69].

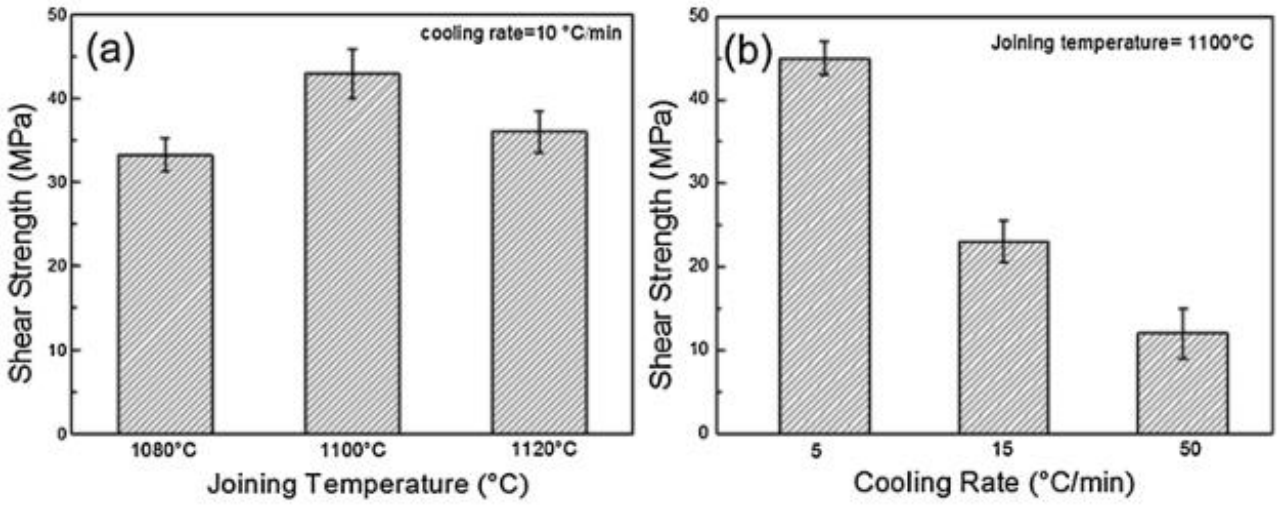

Figure 2.12: shear strength of CLAS glass-ceramic P-Si_3N_4/D-Si_3N_4 joints bonded at (a) 1080-1120°C (b) 1100°C as a function of the cooling rate[69].

The objective of this work is to investigate and optimize the possibility of joining a bulk sheet alloy to a porous one of analogous composition. Initially the glass of choice was the V10 glass, and accounts for the greatest variety of sample configuration treatments and set-ups. As will be demonstrated the GC2 glass yielded the better morphological results and is chosen along with a particular joint configuration (that will be explained) to perform a series of test: simple traction mechanical test before and a thermal aging and cycling process. Further analysis includes a CT scan of the reference sample set-up.

3 Experimental Procedure

3.1 Materials

3.1.1 Porous and Bulk alloy sheets

The porous substrate used for the experiments is a Fe22Cr ferritic stainless steel; this porous alloy was already characterised for high temperature corrosion in a previous study carried out by Koszelow et al ref [70]. It is an experimental product designated as MW2, of composition indicated in *Table 3.1*, produced by Höganäs AB, Sweden. The 0.4 mm thick steel sheets were manufactured with a proprietary tape-casting of steel-particle slurry, followed by drying, debinding and sintering at 1250°C in pure H_2 atmosphere. The size of the particles used ranged between 10-50 µm. The final product porosity amounts to 30% of free volume[70].

Table 3.1: Composition of the MW2 porous stainless steel (values in %wt) [70].

Fe	Cr	Mn	Si	Ni, Cu, Mo
Bal.	22	0.23	0.08	<0.03

The dense alloy sheet used is Crofer 22APU of composition shown in *Table 3.2*, is 0.3 mm thick.

Table 3.2: Crofer 22 APU composition (%wt)[71].

Fe	Cr	C	Mn	Si	Cu	Al	S	P	Ti	La
Bal.	20-24	0.03	0.3-0.8	0.50	0.50	0.50	0.02	0.05	0.03-0.20	0.04-0.20

3.1.2 Glass-ceramics

Two types of glasses were used in this study: V10 and GC2 systems, previously used in other works at Politecnico di Torino [72]. The compositions are shown in *Table 3.3*.

Table 3.3: Chemical composition in %wt of the V10 [72] *and GC2 glass systems.*

% wt	SiO_2	CaO	Na_2O	Al_2O_3	B_2O_3	BaO	MgO
V10	49.2	14.3	9.3	8.3	5.8	/	13
GC2	34.7-41.7	3.2-6.5	/	2.4-7.1	4-8	44.3-53.2	/

V10 glass was obtained by heating the precursor powders in a Pt-Rh crucible in a furnace at 1600°C for 1h at 10°C/min; successively the melted glass was poured onto a brass plate [72]. GC2 raw powders were mixed and melted in before mentioned Pt-Rh crucible at 1500°C, for 1 h. The first 30 min a lid covered the crucible and, for the remaining time, it was removed to allow better gas by-product evacuation from the melt. The melt was then casted onto a brass plate and left to cool [73]. The obtained bulk glass was reduced into powders through a ZrO_2 ball mill and sieved at particle size ≤25 µm in a stainless-steel sieve. After that, powders were used to create a slurry for deposition

3.2 Methods and equipment

3.2.1 Joint preparation procedure

For the joint processing roughly 10 x 10 mm^2 squares of MW2 and Crofer were cut with an abrasive disc cutting machine. The squares were then deburred onto 600 grit SiC abrasive paper, straightened (since were easily bent), prior to cleaning to avoid contamination. The segments were placed between two flat steel blocks in a press at 20 Bar for a couple of seconds. No deformation or alteration to the porous structure was detected. Cleaning occurred in ultrasonic with acetone first, then ethanol bath, and once dried, they were ready for deposition.

Starting from the cleaned substrates the joints were processed by depositing by hand at room temperature a glass powder-pure ethanol slurry (70-30% wt respectively). The base substrate (porous or dense according to the configuration) was placed onto an alumina base-plate. The glass slurry was carefully deposited onto the substrate with a spatula. After the deposition, the second sheet (dense or porous) was placed on top and lightly pressed to maximize the contact area with the slurry, in order to form a sandwich-like structure. Different configurations were experimented, porous alloy on top of the dense Crofer and vice versa. Some of the plates (both foam and bulk) were preventively pre-oxidized; at 900°C for 2h with a heating/cooling rate of 5°C/min in the OVMAT 2009, Manfredi (Italy) resistance oven. Other tests involved the use of preventively degased MW2, heat treated in a tubular furnace (STF 16/ 180, Carbolite Gero, Hope Valley, UK) at 850°C, 1h with 5°C/min as heating/cooling rate under flowing Ar. Depending on the sample, the joints were carefully loaded with either a 3.8g alumina block or a 15g Crofer block or left free of any load. The resulting weight distribution were 3.8 g/cm^2 and 15g/cm^2 (or 3.7 $x10^{-4}$ MPa and 1.5 $x10^{-3}$ MPa respectively).
Different atmospheres and temperatures were evaluated for the joining heat treatment. Atmospheres varied: air, Ar and vacuum were used in specific ovens: CWF 1300, Carbolite (UK) and P330, Nabertherm (Germany), under vacuum into the RHTH 70-150/16, Nabertherm (Germany) and under flowing Ar in a tubular oven STF 16/--/180, Carbolite (UK), already used to perform the degassing of the MW2 alloy. The heat treatment was chosen depending on the glass used: for V10 the peak temperature varied from 850°C to 950°C and 950°C for GC2 glass. Dwell and heating/cooling rates were kept constant at 1h and 5°C/min respectively, occasionally for V10 glass joints an initial 500°C 1h dwell was used. *Table 3.4* resumes the different possibility for each of the variable previously discussed.

Table 3.4: Variables in joint manufacturing.

Architecture	Crofer on MW2; MW2 on Crofer
Glass	V10; GC2
Substrate oxidation (prior to joining)	On MW2 and/or Crofer (900°C, 2h, 5°C/min)
Substrate glass coating (prior to joining)	MW2 and Crofer; MW2 only
Foam Degasing (prior to joining)	No degassing; Argon (850°C, 1h, 5°C/min)
Joining atmosphere	Air; Ar; Vacuum
Load	No load; 3.8g Al_2O_3; 15g Crofer block

3.2.2 SEM and EDS characterization

In order to morphologically characterise joined samples, the cross-section was polished parallel to the joint thickness with SiC papers progressively increasing from 320 up to 4000grit. Metallization ensued to render the so obtained cross-section more conductive, the metals used were Pt and Au. Fracture surfaces were also metalized in order to observe the possible failure causes.
The microstructure observation and analysis were carried out with a JCM-6000Plus-7E desk SEM and EX-230**BU_37001-8 EDS module, both made by Jeol Ltd., Tokyo, Japan. A scanning electron microscope device produces a high magnification image by detecting secondary electrons emitted by a sample after the interaction with a focused electron beam. The image reproduces the morphology of the investigated area. By detecting the back-scattered electrons it's possible to have an indication

of the composition of the surface. The lighter the elements the brighter will appear in the image. The sample, detector and electron beam need to operate in high vacuum in order to minimize electron interaction with gaseous species. EDS analysis were used to investigate the different phase compositions. Energy dispersive X-ray spectroscopy or EDS in short is used to have a qualitative and quantitative composition of the investigated area. The X-rays emitted by the sample after primary beam interaction have a distinct energy that can be correlated to the emitting atom type.

3.2.3 Wettability study

The heating stage microscopy (HSM) was used in order to investigate the sintering behaviour of the glass powders as a function of the temperature. The sample for HSM (Hesse Instruments, Harzgerode Germany) was a cylindrical pellet (3 mm diameter and 3 mm height) obtained by uniaxially pressing the glass powders with some drops of ethanol in a die. The measurement was carried out by placing the sample on a specific support (chosen based on the material on which the wettability is to be studied). The substrates in this work were MW2 and Crofer plates, sized to 8 x 10mm^2, eventually pre-oxidized with the pre-oxidation treatment mentioned before.
The heat treatment consists in heating until the instruments automatically detected the melting of the sample. On the basis of the shapes and dimensions assumed by the samples during the heat treatment, the instruments automatically detected some characteristic temperatures: first shrinkage temperature (T_{fs}), maximum shrinkage temperature (T_{ms}) deformation temperature (DT), sphere temperature (ST), half-sphere temperature (HT), flow temperature (FT).
The deposition thermal treatment (coating process) was chosen on the basis of the results of DTA and HSM analyses carried out at 10°C/min: 1300°C for 10 minutes + 855°C for 30 minutes.
It was carried out in a tubular furnace (STF 16/ 180, Carbolite, Hope Valley, UK) under continuous Ar flowing, with 10°C/min as heating rate, and it was used for producing glass-ceramic samples as well as coated samples (described later in this chapter).

3.2.4 Thermal aging

Five joined samples were submitted to a thermal ageing and subsequent mechanically tested. The treatment consisted in 700°C for 500h in air. The temperature of 700°C represents the best compromise for lifetime and performance in a possible fuel cell application. Such treatment was performed at the University of Hertfordshire, Hatfield, Hertfordshire UK.

3.2.5 Simple tensile test

The tests consisted in a modified ASTM C633-01, conducted at the laboratories at Politecnico di Torino on test machine (Syntech 10/D by MTS Corp.). The grips attached onto two loading fixtures already used by *Baino et al*.[74]. It consists of a steel cylinder 16-mm in diameter with a through 6-mm hole at about 6 mm from a face, as in *Figure 3.1 a)*, glued to the joint sheets putting a perpendicular stress on the joint itself. The fixtures were cleaned with pure ethanol, the circular base was coated with a hand-deposited thin Araldite® 2015 epoxy resin layer (capable of resisting up to 22 MPa as declared by the manufacturer [75]). Then the joined sample was laid in the centre of the cylinder base and lightly pressed. Particular care was to be put in the quantity in order to avoid the "bridging effect" of the glue contacting the glass-ceramic, skewing the results. The orientation of the joined alloys was identical to the one in the oven; the top alloy was also the top alloy in the tensile test and vice versa. Co-axiality of the loading fixtures was assured by the use of a jig constituted by

an aluminium block twice as tall, the holes slightly larger than the cylinders making them stand upright as show in *Figure 3.1 b)*; with the axis perpendicular to the bench plane.

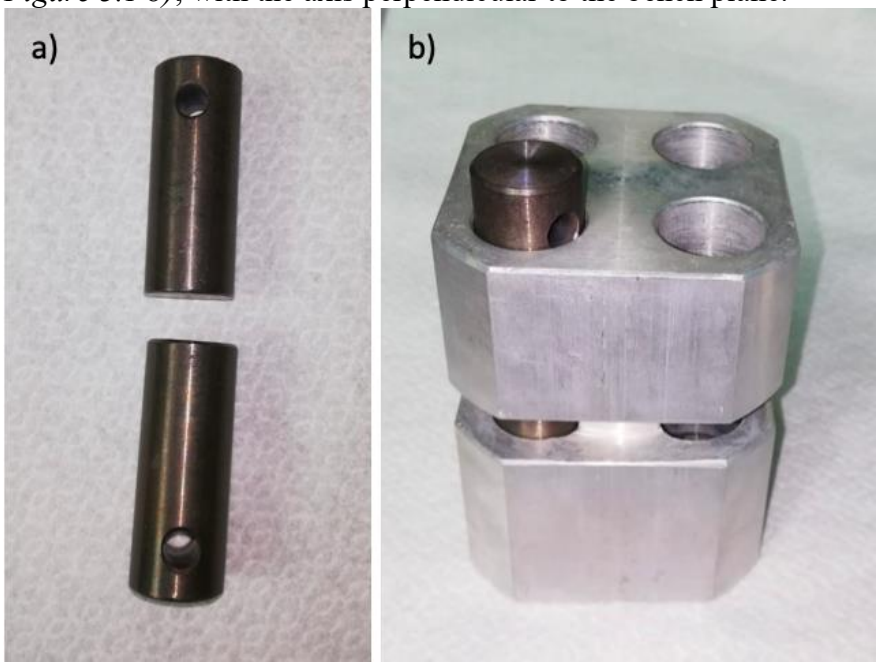

Figure 3.1: a) steel loading fixtures and b) aluminum jig to maintain co-axiality.

The second fixture was carefully laid onto the sample-bottom cylinder assembly, already inserted into the jig. The whole jig containing the sample/fixtures assembly was then carefully placed in oven to cure and left to cure (1h at 85°C). After the curing, samples were loaded onto the machine as shown in *Figure 3.2*, the cross-head speed was set to 0.5 mm/min. A total of four samples were tested; after fracture the effective surface area was measured, and was used to obtain the maximum stress from the peak force. The results yielded an average stress ± standard deviation. After the tensile test, the fractured joints were removed from the fixtures by heating in an oven at 400°C for an hour to burn-off the glue, then wiped clean with ethanol and metalized for SEM observation.

Figure 3.2:Loading fixture-sample assembly in the test machine.

3.2.6 CT Scan analysis

Computerized tomography is a non-destructive technique that allows to obtain morphological and density information of the entire sample volume. The process articulates in three phases; scan, reconstruction and analysis. The scanning requires the generation of X-rays: a cathode emits electrons onto an anode (typically composed of W), this interaction generates X-rays. The obtained radiation is polychromatic with some sharp and defined peaks. Radiation impacts the sample and can be absorbed to varying degrees. It is essential to have a component of the incident rays to be transmitted in order to generate enough contrast to evidence the sample. Attenuation of the incident X-rays is described by the Lambert-Beer equation, its attenuation coefficient is proportional to the atomic mass of the interacting element of the sample and inversely proportional to the incident ray energy. The transmitted rays impact onto a detector screen behind the sample and the X-ray source, generating a shadow image of the entire sample volume. Darker areas indicate higher absorption, hence heavier elements. The sample is rotated onto an axis perpendicular to the X-rays generating as many shadow images as desired by the operator. By increasing the number of views, which in terms consist in diminishing the degrees of rotation between each shadow image, greater detail is achievable, at the cost of higher scanning and analysis time. The reconstruction consists in creating a 3D model of the analysed volume via software. The analysis consist in modulating the grey scale in order to evidence the sample and giving contrast to chemically and physically distinct area of the same, while excluding the rest of the sample volume represented by air [76].
In this work a GC2 joined sample was subjected to CT Scan analysis at the Advanced Joining Technologies (J-TEC) Laboratory at the Politecnico di Torino, in order to have a better view of the internal structure and integrity of the same. The CT scan used is custom built by IKTS Fraunhofer, has a maximum X-ray tube operating tension of 300kV, a resolution of about 9µm (5µm in optimal conditions) and 400 x 400 mm detector with a 200 µm resolution.

4 Results and discussions

4.1 V10 glass joined samples

4.1.1 Morphological characterization

The first sample (sample 1) was produced using an MW2 square pre-cut with shears, hence was lightly warped and no viable way of efficient straightening was found at this early stage of the experimentation, the V10 glass was not sieved. The joining treatment used was 850°C 1h dwell in air and the foam was placed on top of the Crofer. On top of the whole joint was placed an alumina block of 3.8g, and was not metallized due to equipment malfunction. Deformation of the porous alloy is evident in *Figure 4.1 a)*, it immediately shows that glass has a greater joining characteristic on the bulk alloy than the MW2. The void shown in *Figure 4.1 b)* is just one of several indicating a sub-optimal deposition during the manufacturing. Upon further inspection the Crofer/glass interface showed a detachment as it was filled by debris from the abrasive; a confirmation comes from the elemental analysis in *Figure 4.1 c).* The glass-ceramic appears to be well consolidated with slight the porosity, irregularly shaped and evenly distributed. The glass/MW2 interface is also filled with debris, some large areas of detachment seen in *Figure 4.1 a)* indicated low adhesion of the glass to the porous alloy. Sample 1 indicated that better bonding to the alloy substrates was crucial.
In order to better understand and evaluate the interface quality of the glass onto the alloys, simple coatings were prepared using the same heat treatment of sample 1. Three coatings were prepared using sieved glass to 25 µm: on pre-oxidized Crofer (900°C, 2h, 5°C/min), on Crofer as-received, on MW2 alloy (samples 2, 3 and 4 respectively).
The coating covered all the substrates surface and the heat-treatment was identical to sample 1. The resulting samples showed shrinkage of the glass thereby leaving a portion of the substrates as if no adhesion occurred. In *Figure 4.2 a)* the pre-oxidized and non-oxidized samples of Crofer exhibit this phenomenon, although to a lesser extent on the non pre-oxidized substrate and almost absent in the MW2 alloy. There is no particular difference in pore size, shape and distribution among the substrates, *Figure 4.2 b)* and *c)* show a very continuous and solid interface between the glass and the Crofer. The Crofer (w/o pre-oxidation), exhibits some metal pushed over the glass-ceramic from the polishing, likely filling the pores at the interface, not present in the other two samples.

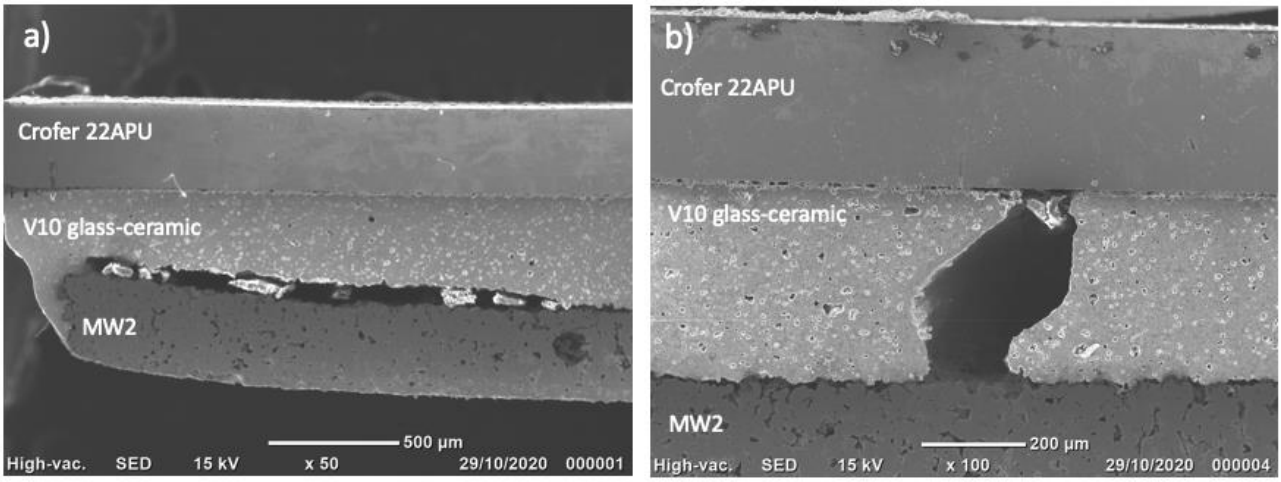

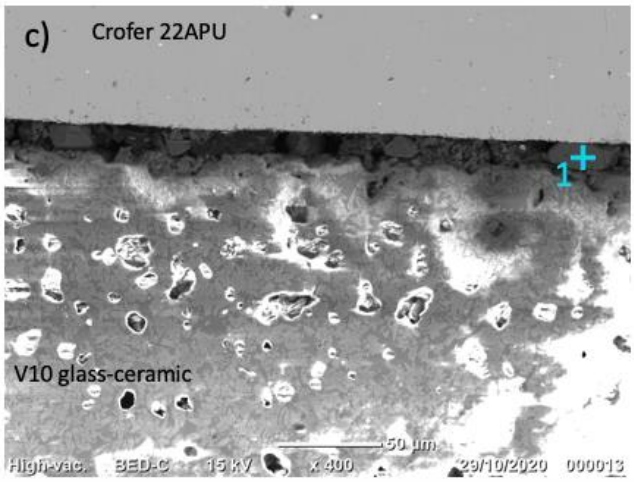

%atm	C	O	Si	Ca	Cr	Fe
N° 1	52.32	1.21	46.23	0.05	0.03	0.14

Figure 4.1:SEM image of Sample 1 cross-section: upside-down with respect to the configuration during the heat-treatment (MW2 bottom-Crofer top, V10 glass, 850°C for 1h at 5°C/min, in air, under 3.8g weight). a) view of the joint edge, b) detail of the interfaces, c) detail of the trapped debris and relative EDS composition. The glass was not sieved and the MW2 was not straightened.

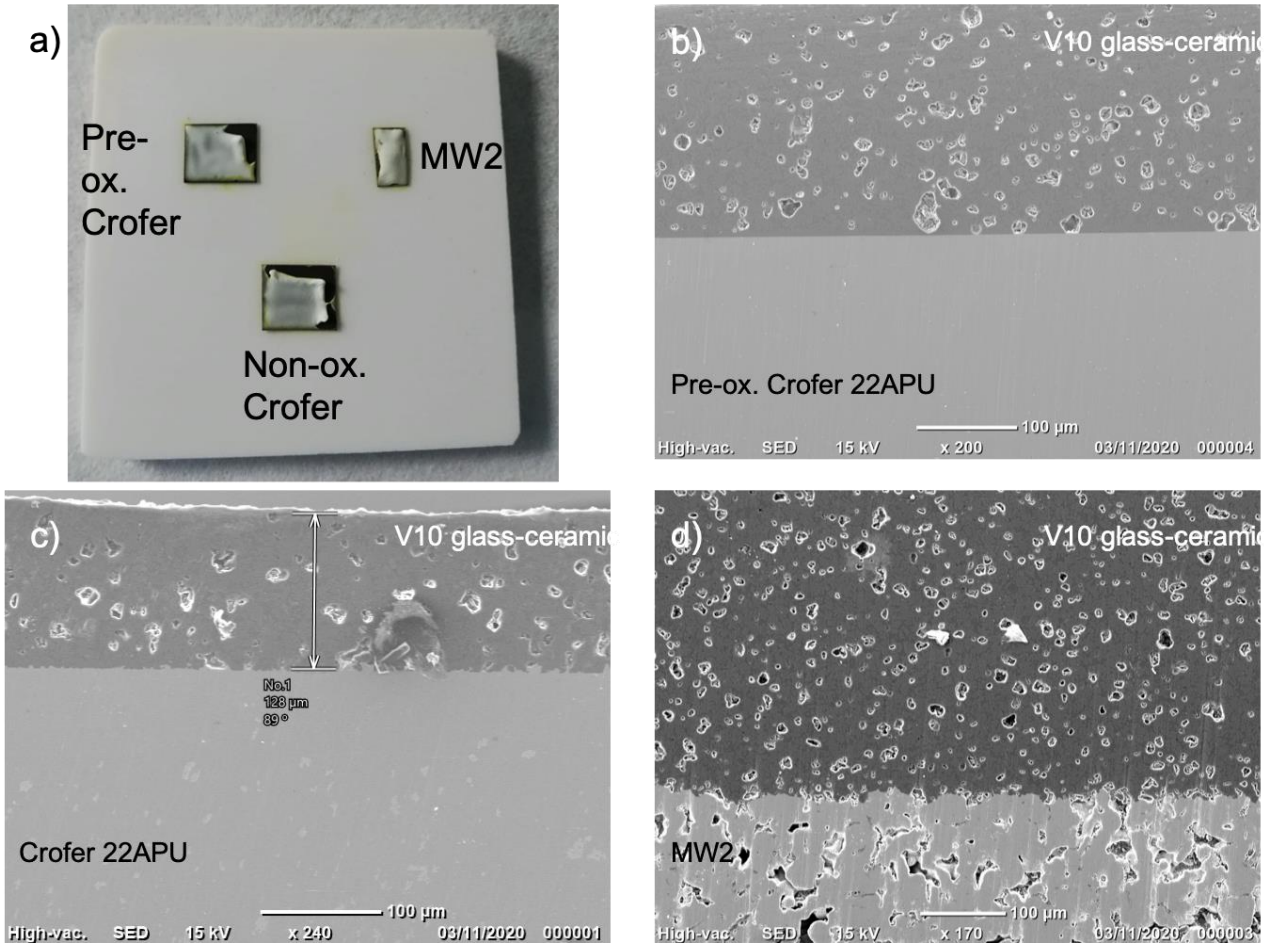

Figure 4.2: Macro image a) and SEM images of the cross-section of coatings after sintering, b) sample 2, c) sample 3, d) sample 4. Sample obtained at 850°C for 1h at 5°C/min, in air.

Sample 4, i.e. the coated MW2 shown in *Figure 4.2 d)*, demonstrated that V10 glass has a very compatibility with the substrate. The glass shrinkage seemed to happen where the slurry was thicker, likely indicating a strong tendency towards sintering of the glass powders and a lower affinity to the metal substrates. The lack of a top plate forcing the adhesion could have contributed to the phenomena that couldn't be otherwise explained.

Some words can be spent on the glass itself; glass transition occurs at 610°C, the main crystalline phase is Augite, an Mg-Al monocline silicate that starts to form around 800°C and has maximum crystallization rate at 840°C[72]. In *Figure 4.3* the crystals correspond to the light grey phase surrounded by a darker glass matrix. A hint of the crystal phase shape can be seen in the red square: indicating a hexagonal platelet. The composition is fairly constant as indicated by *Table 4.1* for points N° 1 and 2, the matrix has higher amounts of Na and Al, but lower Mg and Ca.

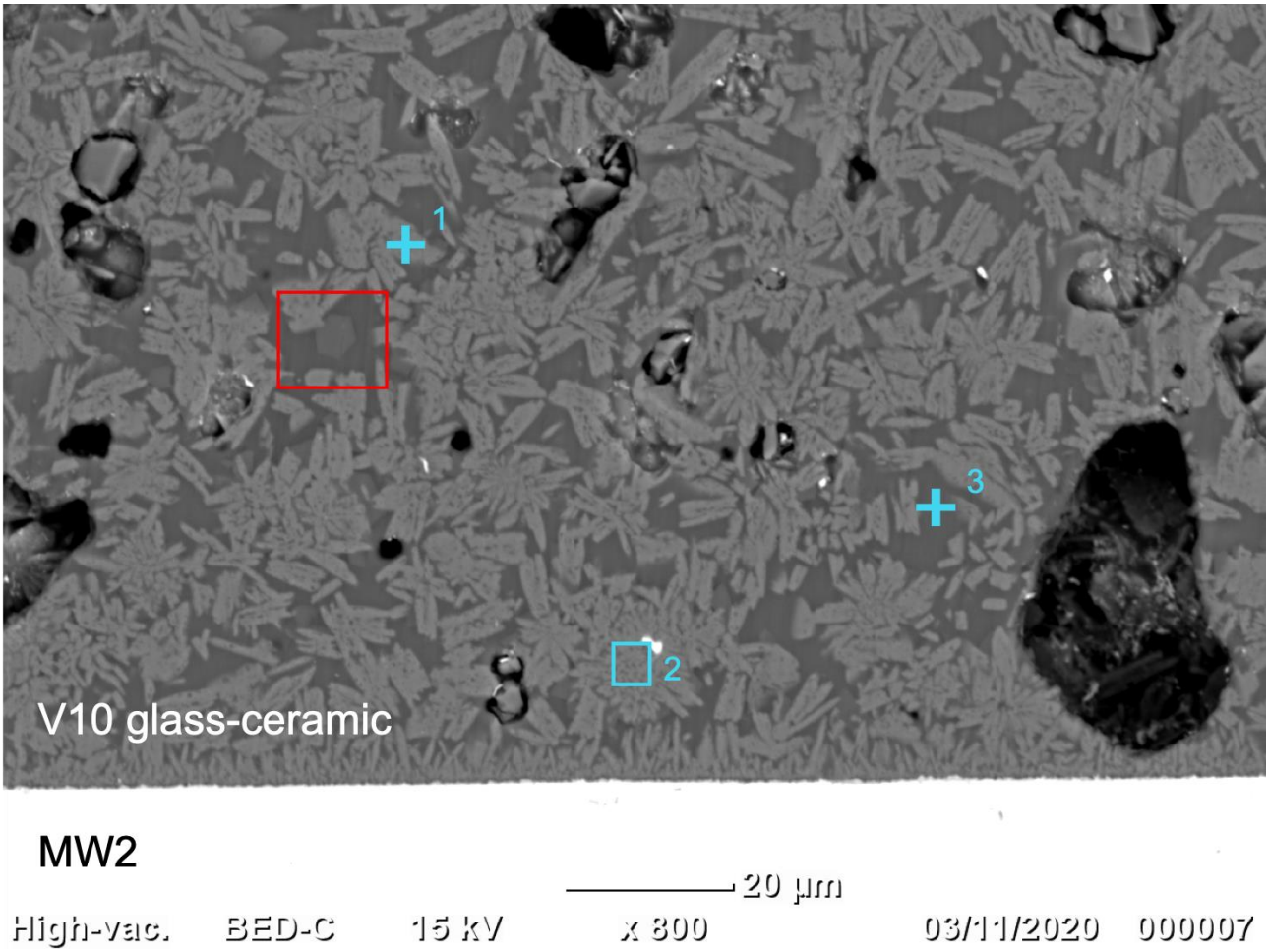

Figure 4.3: EDS analysis of Sample 2 (850°C for 1h at 5°C/min, in air).

Table 4.1: Chemical composition of the EDS scan points/areas indicated in Figure 4.3 (% atm).

%atm	O	Na	Mg	Al	Si	Ca
N° 1	62.07	2.04	7.96	1.89	18.44	7.59
N° 2	64.55	3.23	6.38	2.80	16.40	6.63
N° 3	65.33	8.30	1.89	7.12	17.03	0.33

In attempt to evaluate the shrinkage of the glass depending on the specific substrate, HSM analyses of the 3 different substrates were performed. The yielded results are shown in the graph of *Figure 4.4*.

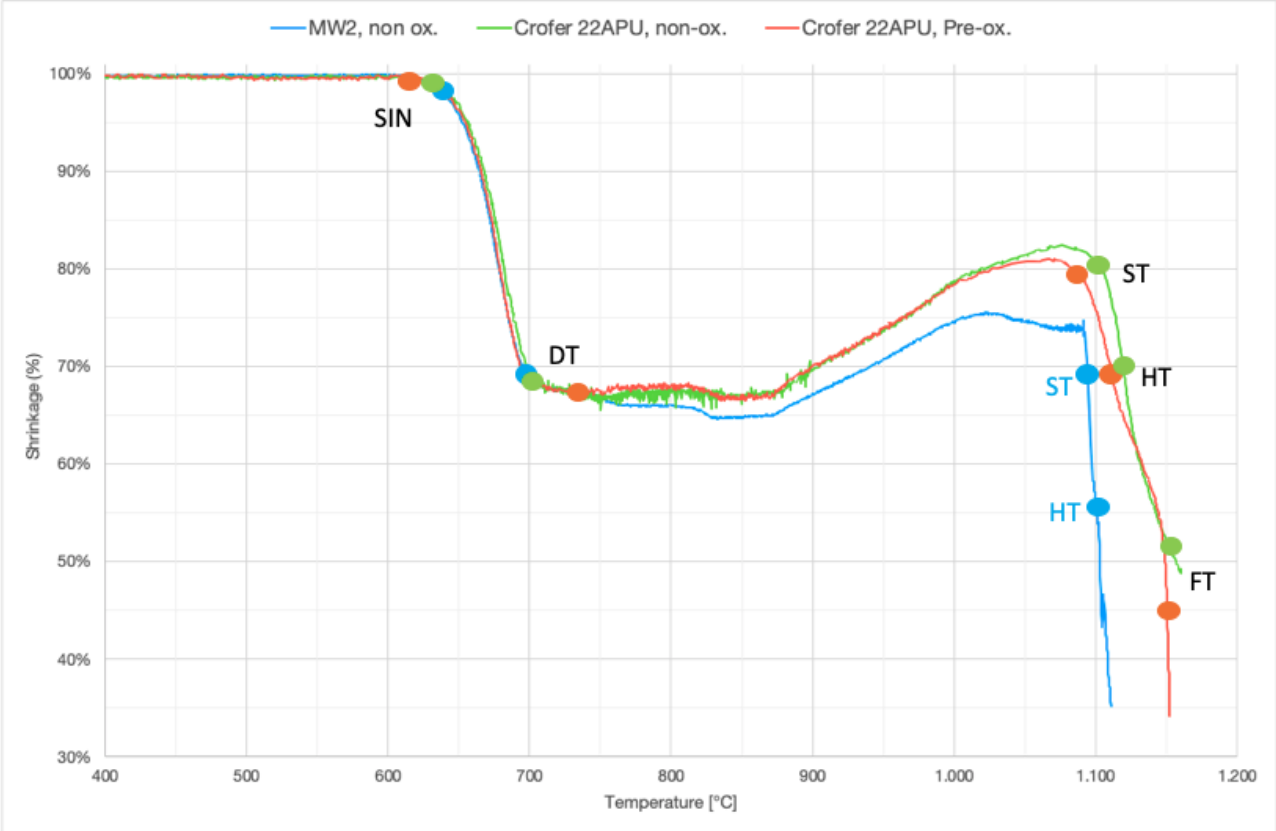

Figure 4.4: HSM curves of V10 glass on different substrates: Crofer (pre-oxidized and not pre-oxidized) and MW2. Characteristic temperatures of the glass are indicated as follows: SIN-sintering temperature; DT-deformation temperature; ST-Sphere temperature; HT-half sphere temperature; FT-flow temperature.

The Sintering behaviour does not seem to be affected by the substrate, but at about 750-800°C the behaviour of the curves tends to differentiate, particularly for the MW2. The range between the initial deformation and the sphere temperature is where sintering competes with the crystallization. The glass has a great tendency to crystallize on all of the substrates, particularly for the pre-oxidized one. MW2 sample shows a sharp decrease of the area, part of it can be attributed to the difficulty of the software to account for the strong warping that occurred. The sphere temperature corresponds to the "melting" of the crystalline phase, and for V10 corresponds to approximately 1100°C. further information of the affinity of the glass to the substrate can be obtained, when on the pre-oxidized Crofer the glass spreads more than the bare substrate as seen in *Figure 4.5 a)* and *b)* respectively. The MW2 substrate visible in *Figure 4.5 c)* and *d)* demonstrates the severe deformation, indicating infiltration in the pores.

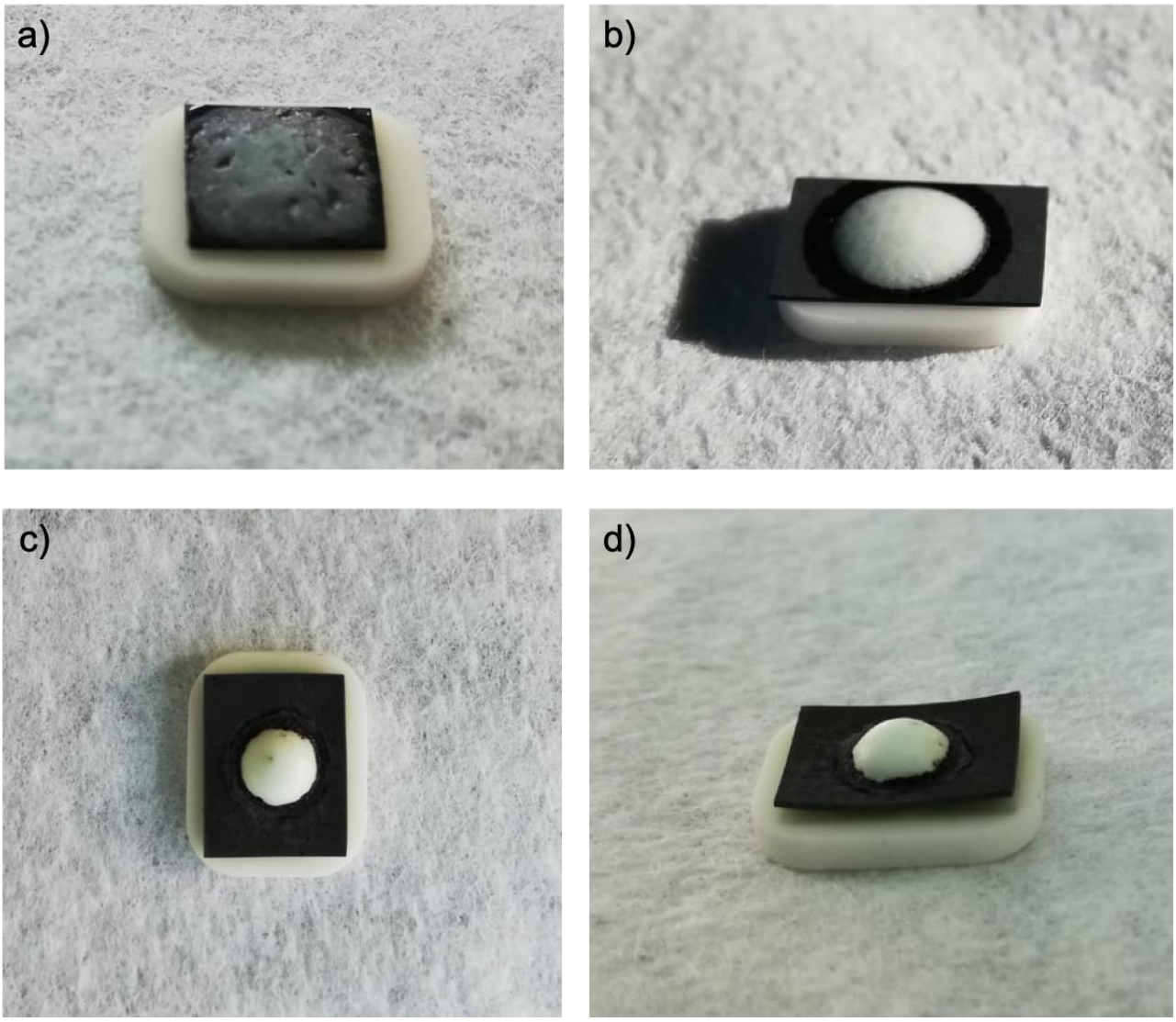

Figure 4.5: HSM sample after the HSM run: a) V10 on Pre-oxidized (at 900°C for 2h at 5°C/min, in air) Crofer 22 APU, b) V10 on Crofer 22 APU w/o pre-oxidation. c) and d) show two different views of the MW2 plate.

Two new joints samples, 5 and 6, were produced identical to sample 1 (MW2 on Crofer and alumina weight), only sample 5 had the Crofer pre-oxidized. This allowed to reach a sound interface (*Figure 4.6a)*), no detachment, although larger voids and discontinuous sections are still present due to uneven slurry depositions. On the contrary the MW2 alloy is detached along most of the cross-section, some glass infiltrated the foam but mainly in the major pores. Different results were obtained in sample 6 as shown in *Figure 4.6b)*; the MW2 alloys exhibits good adhesion and interface continuity. The un-altered Crofer/glass-ceramic interface shows the presence of abrasive particles indicating a detachment similarly to sample 1. It is evident that the oxide layer on the Crofer greatly increases the affinity for the glass, but does not help with overall joint integrity. While on both samples the foam alloy was placed on top two such different results were not expected, leading to think that surface treatment may influence the behaviour of other areas of the joint.

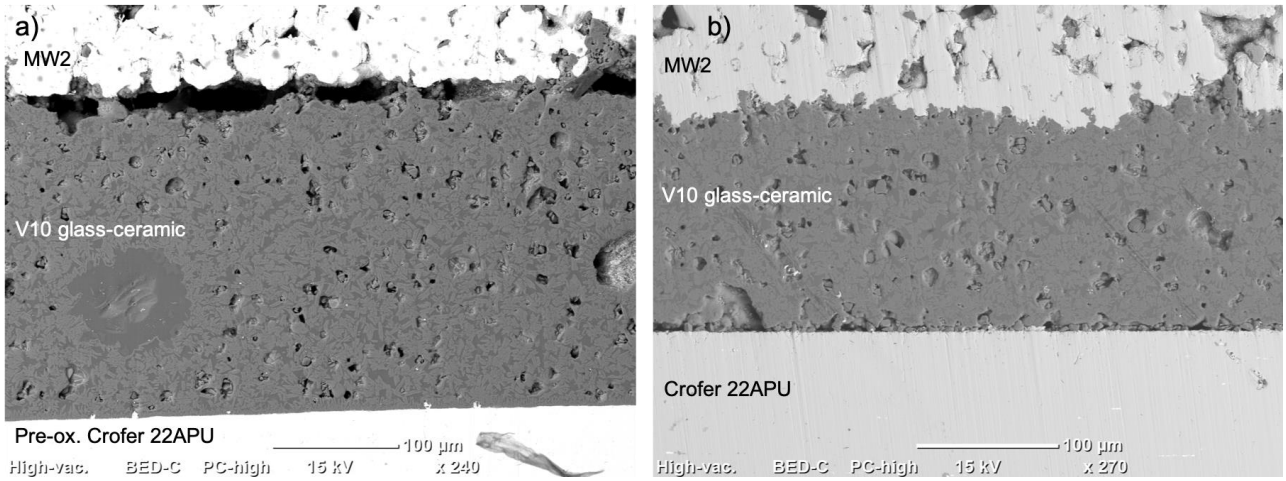

Figure 4.6: SEM images of cross-sections from a) Sample 5 and b) Sample 6. Both treated at 850°C for 1h at 5°C/min, in air, under 3.8g weight. *Samples were not metallized and MW2 was not straightened.*

Further tests involved the oxidation of both substrates prior to joining, labelled as sample 7, and sample 8 using a pre-oxidized Crofer on top, inverting the former setup. For these joints the load was increased to 15g/cm^2 (and will remain the same for all samples from now on). The MW2 plates from this point on were all successfully straightened. As seen in *Figure 4.7 a)* and *b)*, it has improved the adhesion only in restricted parts of the joint, as some are completely detached. It can be assumed to be caused by thermal expansion difference or possibly to the release of internal stresses in the alloy. The surface oxidation has been shown to be minimal for such short oxidation times, as demonstrated by Koszelow et al. [70], so no pores could be occluded in any significant way to justify the slight difference in MW2 alloy interface. Where the joint is sound, larger than average pores are present, glass can be drawn into the pores when molten leading to "lacking" material in the joint. For sample n°8 in *Figure 4.7 c,d)* the set-up resulted in improved interfaces both with the Crofer and the MW2, but some detached areas persist. This configuration (pre-oxidized Crofer on top of MW2) produced the best results in terms of adhesion. However, a light mid-thickness elongated porosity is evident in such joint: it is clearly undesired as it can negatively impact the mechanical strength of the joint.

Given the excellent adhesion of the same to the glass and the good adhesion of the glass in a MW2 coating of sample 4 this could possibly give the best of both worlds at the cost of greater manufacturing complexity. Weight, joining treatment and atmosphere were kept the same (15g/cm^2, 850°C 1h dwell at 5°C/min, air) as for sample 9 production.

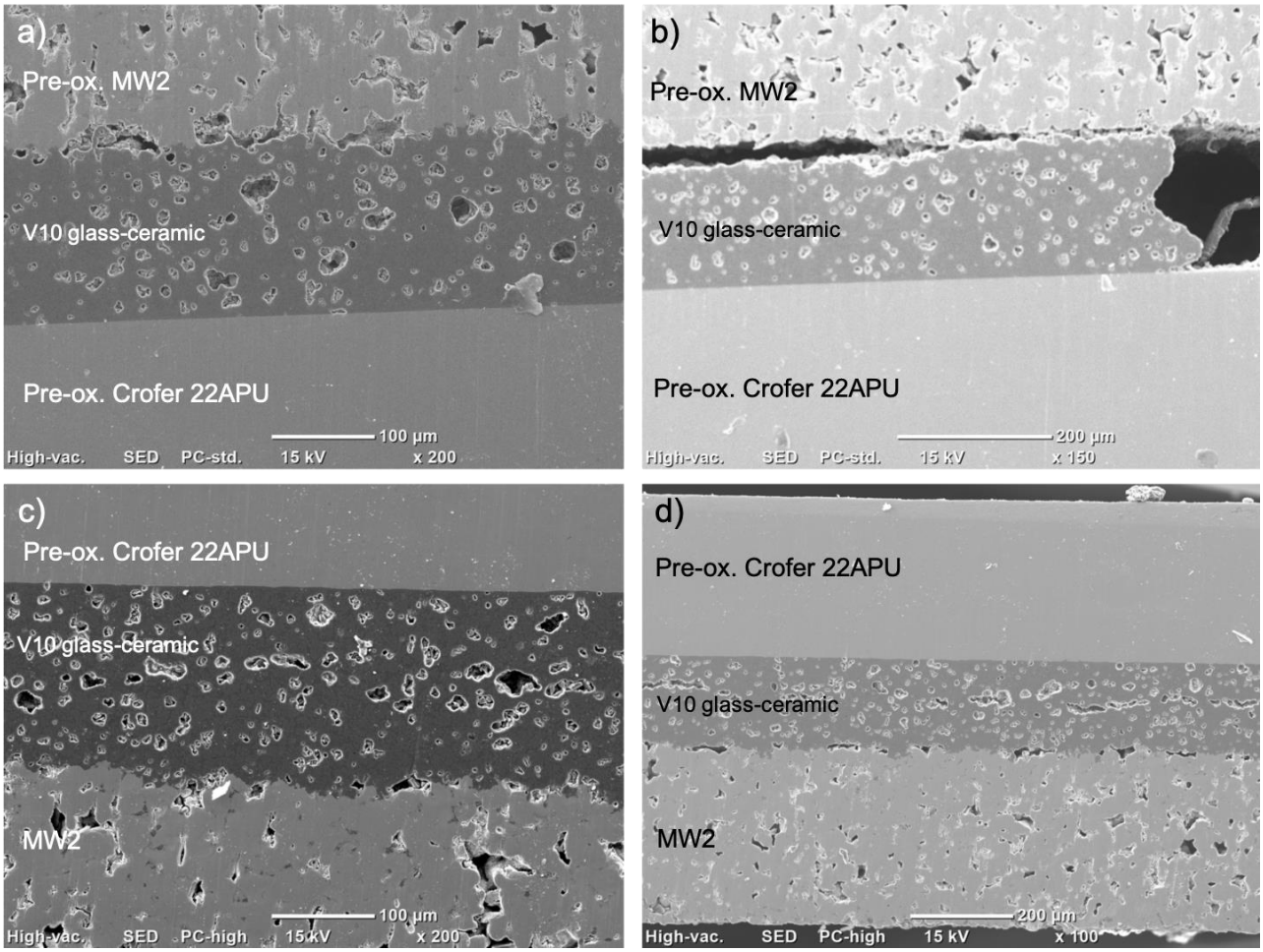

Figure 4.7: SEM images of: a,b) Sample 7: both substrates previously oxidized. c,d) Sample 8. Treatment conditions: 850°C for 1h at 5°C/min, in air, under 15g weight.

Sample 9 showed a good adhesion with both MW2 and Crofer but not as good as observed in sample 8, especially on the latter substrate. While being on the bottom like for sample 7 the interface is noticeably worse (*Figure 4.8 a)*). This is particularly unexplainable; pre-oxidized Crofer has greater bonding characteristics then the clean alternative whether on top or bottom for the simple configuration, while when combined to a coated MW2 exhibits higher discontinuities.
In *Figure 4.8 b)* a subtle line of pores indicates the interface between the coating and the glass slurry, a constant thickness of glass-ceramic arched towards the coating and detaching from the pre-ox. Crofer substrate in many sections of the joint, making it de-facto unsuccessful. While homogenous in distribution and size the porosity is still unsatisfactory high and shall be reduced.

A possible solution to the joining problems encountered was believed to lie in the treatment temperature. By referring to samples 2 and 4, the relative HSM curves (in *Figure 4.3)* and the images at 850°C and 900°C in *Figure 4.9*, it can be noted that at 900°C the pellet on MW2 has slightly lower contact angle than at 850°C. Furthermore, by increasing the temperature, the viscosity of the glassy matrix also lowers supposedly allowing for better spreading on the substrates under load. For this reason, the peak temperature was raised to 900°C while maintaining constant the dwell. Sample 10 was so composed: the bottom substrate was MW2, the pre-ox. Crofer plate on top, all under 15g load and heat treated to 900°C for 1h a 5°C/min in air. During polishing a fracture at the glass/MW2 interface occurred, thus indicating bad adhesion.
For sample 11 the configuration and parameters during the thermal treatment were identical to sample 10. The adhesion to the alloys remained unchanged, no significant difference was found when compared to sample 8. It must be noted the sample was not metallized, hence the interface suffers from the darkening of the glass in proximity to the metal from the release of excess surface charge.

The porosity was still high and mid-joint voids are very evident in *Figure 4.8 c)*. It is possible to note the good adhesion at the Crofer and what seems to be the surface oxide layer in *Figure 4.8 d)* and its composition in *Table 4.2*. While the joint appears to be sound the long voids and the distributed porosity are still present, the strategies used did not sort any apparent effect to reduce such occurrences.

Table 4.2: Chemical composition of the EDS scan points/areas indicated in Figure 4.8 f) (% atm).

%atm	O	Na	Mg	Al	Si	Ca	Cr	Mn	Fe
N° 1	20.45	0.37	0.16	0.53	0.49	0.23	20.14	0.15	57.48

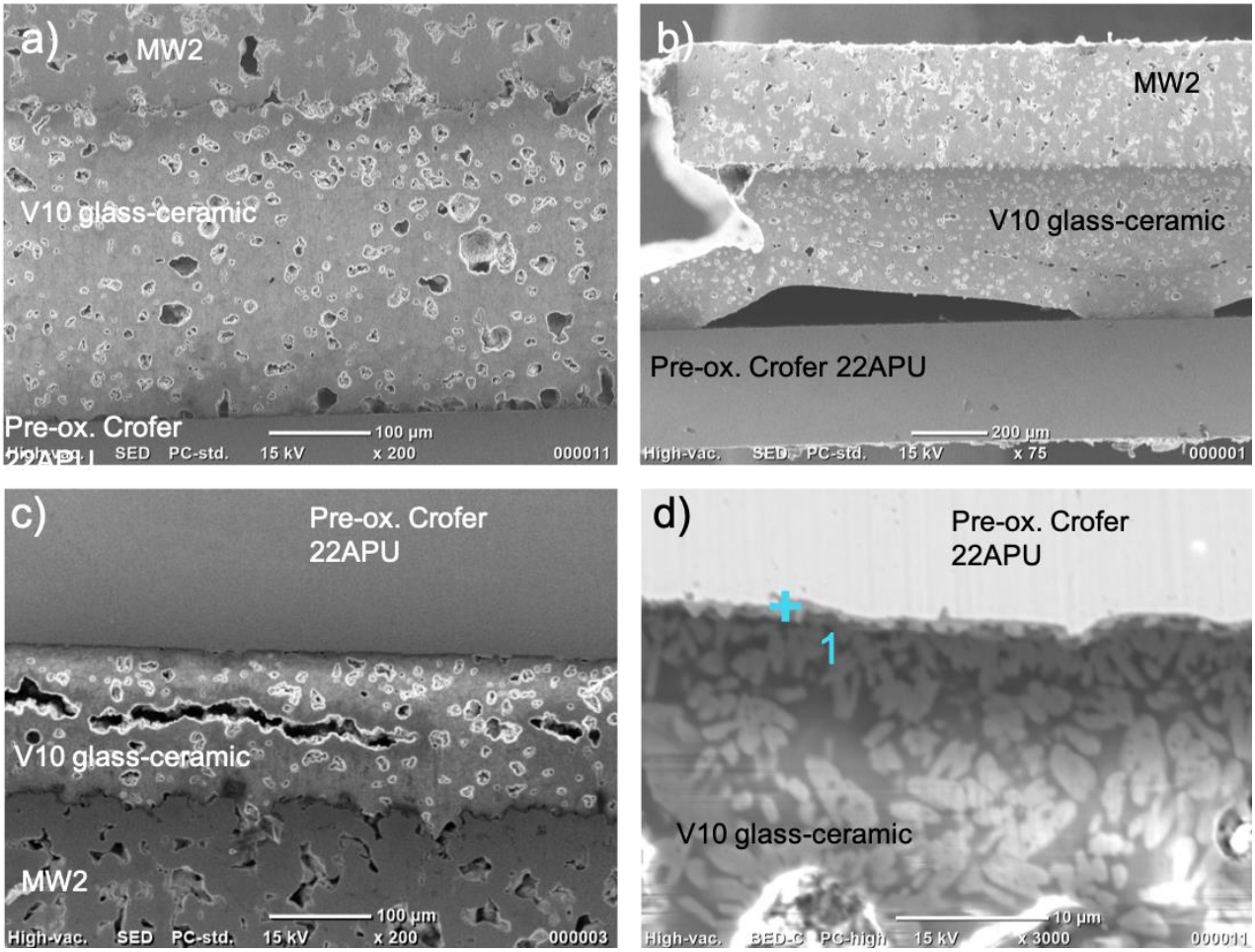

Figure 4.8:SEM images of: a,b) sample 9: coating and joint were treated at 850°C for 1h at 5°C/min, in air, to the joint 15g top weight was added.
c) sample 11; joined at 900°C for 1h at 5°C/min, in air, under 15g weight. d) zoom in the Crofer interface of sample 11. All of the samples were not metallized.

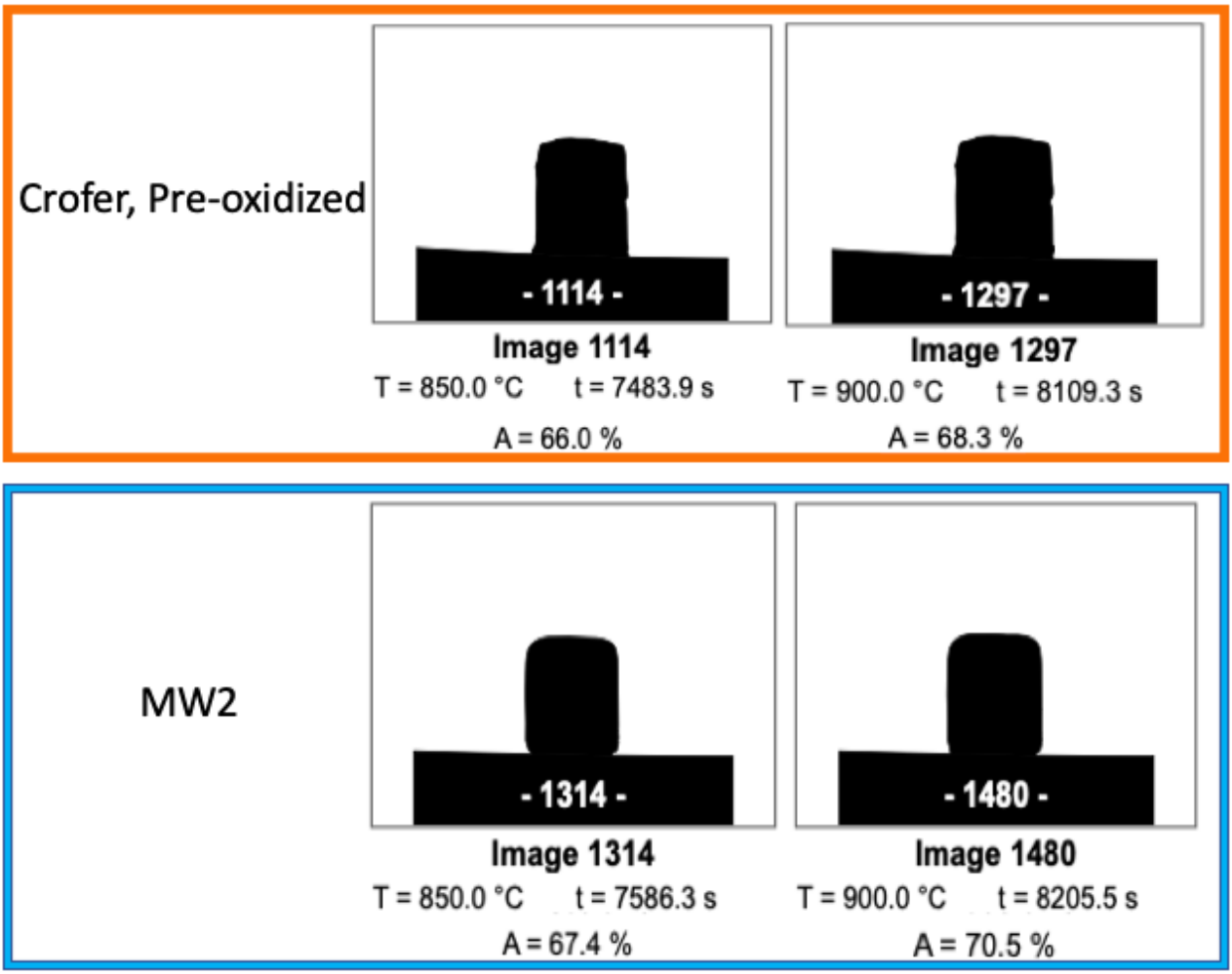

Figure 4.9: Comparison of HSM images of V10 pellet on different substrate, along with time, temperature and area % of the recorded images. Top: Crofer, pre-oxidized, bottom: MW2.

4.1.2 Argon treatments

It was hypothesized that red-ox reactions with the atmosphere produced gasses that were then trapped inside the glass-ceramic melt, so a possible way to verify it was to conduct the joining under inert Ar flux.
Sample 12 reproduces the previous sample, but thermally treated in Ar atmosphere in a tubular oven; a cross section can be seen in *Figure 4.10 a)* and *b)*. The adhesion was found to be excellent both on Crofer and especially on the MW2. The glass infiltrated up to the considerable depth of 50 µm, the layer adjacent to the glass/MW2 interface appeared to be particularly dense and with fewer pores. The same held true for the bulk alloy, especially when compared to sample 9 and 11 in *Figure 4.8 a,c)* respectively. When moving to the centre of the joint two rows of porosity are visible, located in proximity of the alloys, encapsulating a somewhat increased number of voids of varying size. For sample 13 the same configuration and treatment were used, however the foam alloy was subjected to Ar degassing during the same treatment of sample 12. After such procedure the joint was manufactured and treated in air at 900°C, 1h dwell at 5°C/min. No significant difference can be noted

from sample 11 in *Figure 4.10 c)* and the elongated porosity is still present. Some sections of Crofer were not successfully joined but it was attributed to a likely uneven glass slurry deposition.

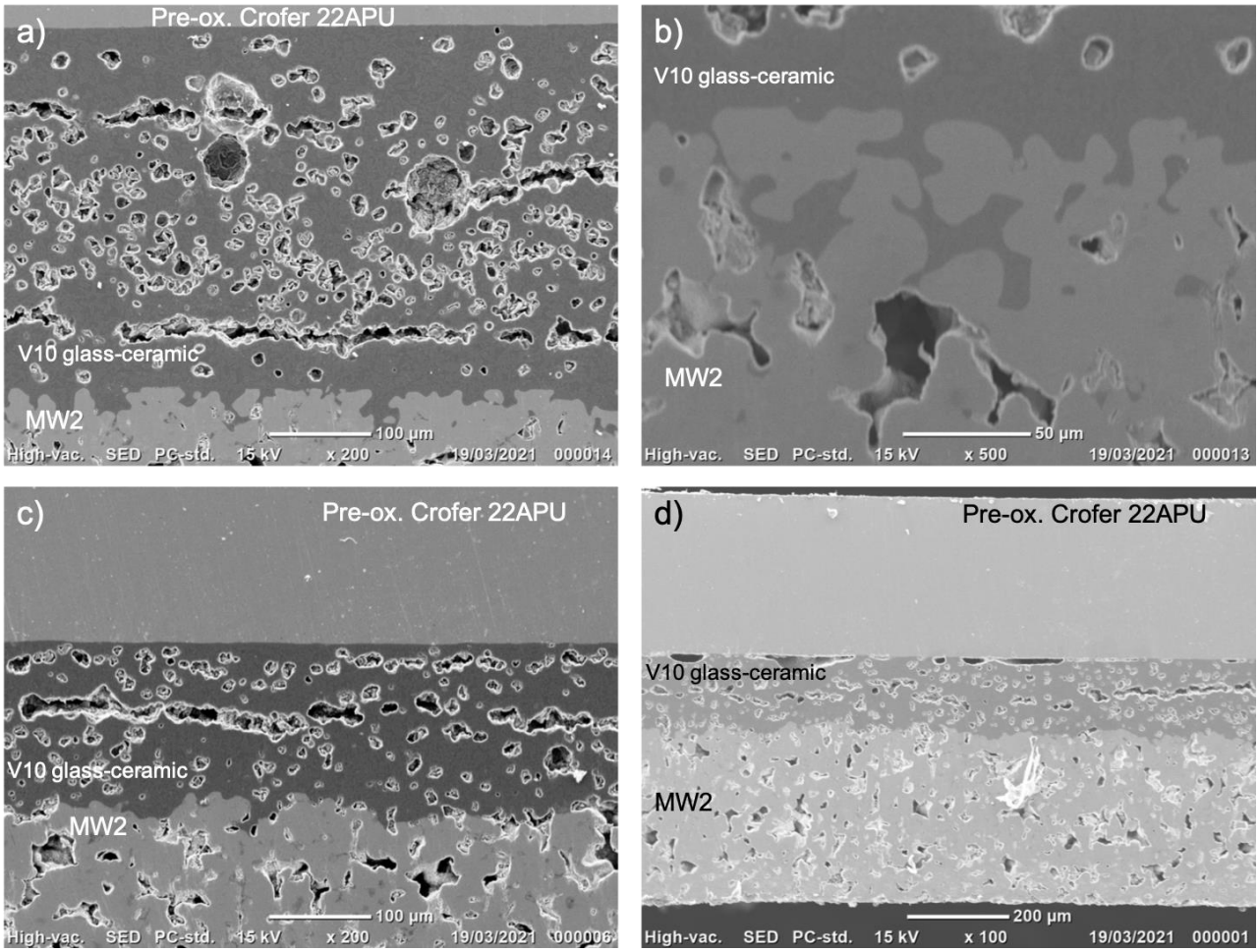

Figure 4.10: SEM images of: a) Sample 12; joined at 900°C for 1h at 5°C/min, in Argon, under 15g weight, and its magnification at the MW2 interface b). Images c,d) Sample 13: obtained at 900°C for 1h at 5°C/min, in Argon, under 15g weight.

4.1.3 Vacuum treatments

The following series of tests aimed at reducing the porosity by vacuum atmosphere joining. Sample 14 was the first of this collection; it replicated the previous setups, namely Crofer (pre-ox.) on top, 900°C for 1h at 5°C/min but with the joining thermal treatment carried out in vacuum. The results are shown in *Figure 4.11 a)*. Glass has infiltrated to the record depth of 160µm into the foam cavities as demonstrated by the darker phase in point 1 of *Figure 4.11 b)* and *Table 4.3*. The Crofer appeared to be detached in most of the cross-section and filled from abrasive particles and metal chips from the joining surfaces (points 2 and 3 in *Figure 4.11 c)* and *Table 4.3*). Contact is surely present in other parts of the joint as it didn't break during polishing. The pore distribution and size however drastically changed: fewer, greater and more irregularly shaped. Some pores were in contact with each other as shown in *Figure 4.11 d)* and are mostly located in the middle of the joint likely rendering the structure less mechanically resistant.

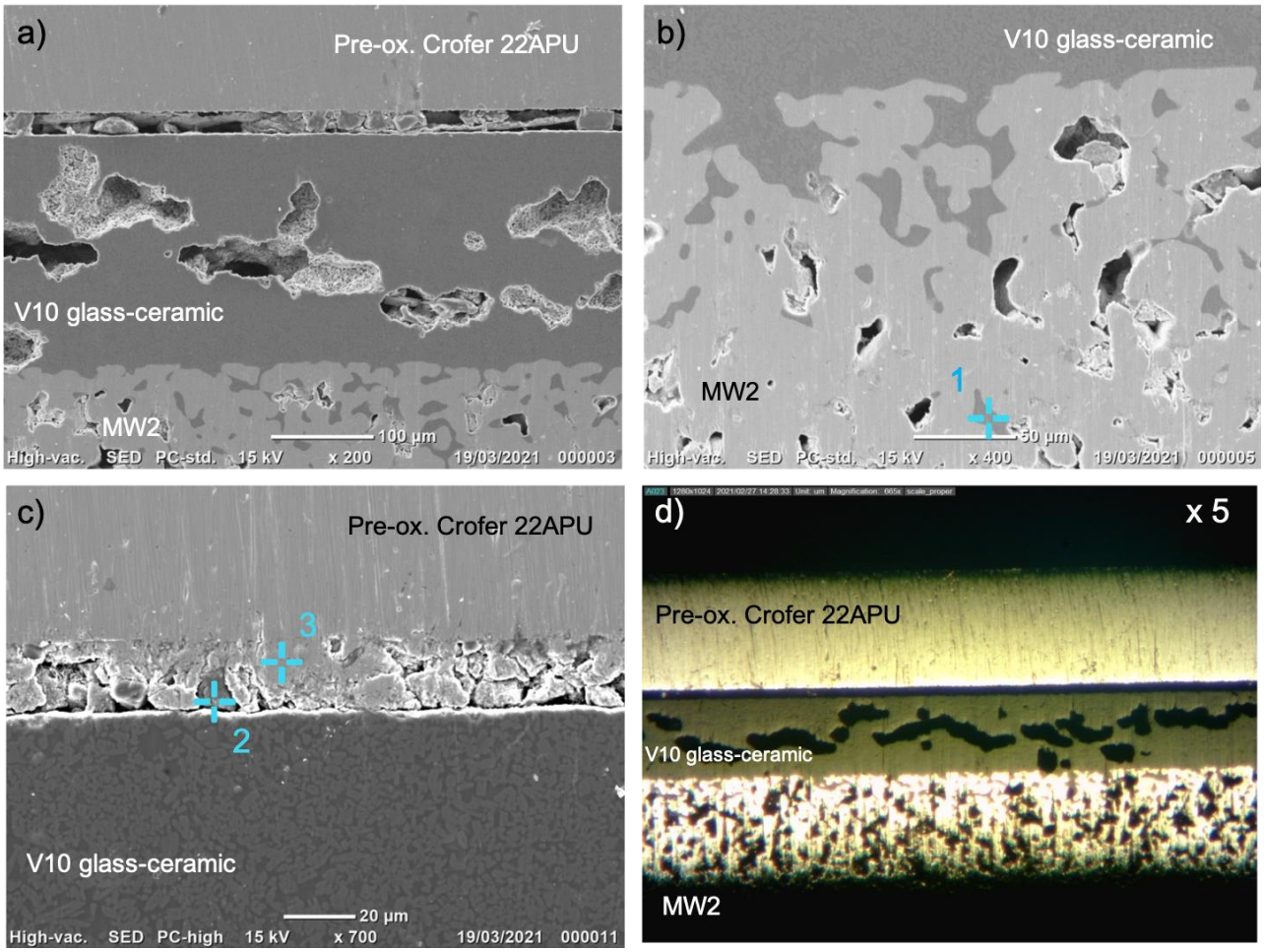

Figure 4.11:SEM images of sample 14 cross-section. a) view of the whole joint section, b) glass/MW2 interface, c) glass /Crofer. In d) an optical microscope image of the joint. Sample joined at 900°C for 1h at 5°C/min, in vacuum, under 15g weight.

Table 4.3: Chemical composition of the EDS scan points/areas indicated in Figure 4.11 *(% atm).*

%atm	C	O	Na	Mg	Al	Si	Ca	Cr	Mn	Fe
N° 1	ND	59.68	8.87	0.11	6.98	20.71	1.28	1.49	0.18	0.70
N° 2	ND	11.43	0.09	0.40	0.77	71.40	1.05	3.85	ND	11.02
N° 3	ND	7.08	0.54	0.04	0.94	6.24	0.24	17.99	ND	66.93

The configuration was inverted from the previous to see if it was possible for the foam alloy on top to assist in gas venting, designated sample 15. In order to evaluate the influence of the foam on the formation of pores some control samples were prepared: a Crofer-Crofer blank, MW2 coating and Crofer coating (all Crofer substrates were pre-oxidized), samples 15B, 15C1 and 15C2 respectively. Both 15 and 15B were loaded with 15g weights and all samples were treated in the same batch. Sample 15, shown in *Figure 4.12 a)*, demonstrates that the foam could not allow for gases to escape the gases; glass powders consolidate and occlude the pores. From sample 14 fewer elongated voids can be seen, but even larger pores tend to locate themselves in proximity of the MW2 substrate. The Crofer interface was substantially unaffected: filled with debris and chips, suggesting that the Crofer over MW2, is a better configuration as the alloys are better bonded, despite the mid-joint porosity. The other samples in the batch 15B (*Figure 4.12 b)*) and C1 (*Figure 4.12 c)*) prove that the porosity is mainly due to the presence of the foam, but unexpectedly also the Crofer coating (*Figure 4.12 d)*) presented analogous pores to C1. The joint 15B presents a glass-ceramic joining of just 70µm thick,

greatly inferior to the coating of sample, leading to believe that the thickness of the applied slurry may strongly influence the formation of the undesired voids.

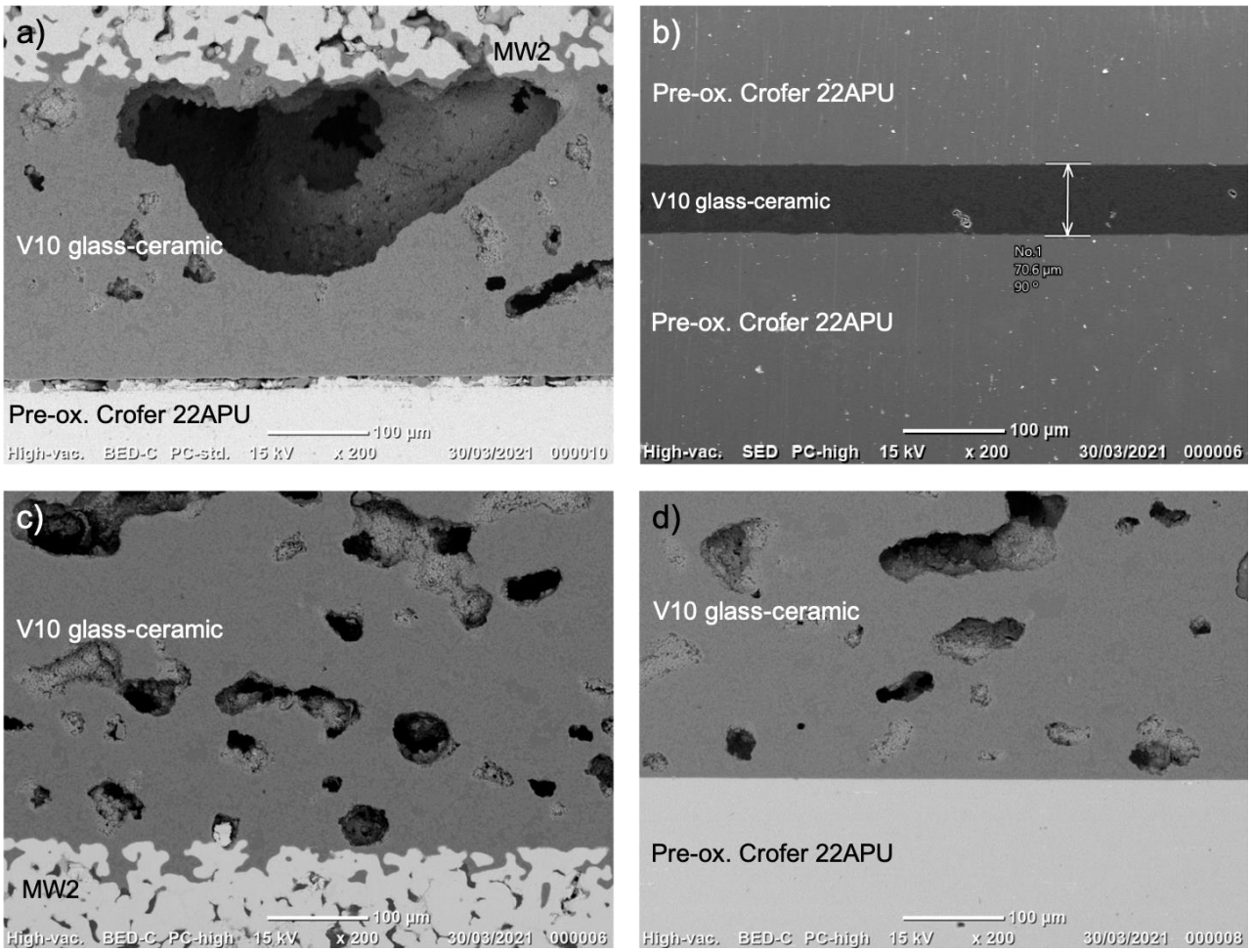

Figure 4.12: SEM images of a) sample 15, b) 15B, Crofer-Crofer joint, c) 15C1; MW2 coating, d) 15C2, Pre-ox. Crofer coating. All of the samples were joined at 900°C for 1h at 5°C/min, in vacuum. Only the joint was under 15g load.

In order to avoid gaseous species, an additional dwell of 1h at 500°C during heating was added keeping the peak temperature at 900°C, supposing it would give more time for it to happen. As before mentioned, another control sample Crofer-Crofer blank was prepared and thermally treated simultaneously. Sample 16, in *Figure 4.13 a)* did not show any particular difference from sample 14, the number of pores actually seem to have increased, locating themselves even in contact with MW2. The detachment at the Crofer surface could not find an explanation, it happened only in presence of the foam, in vacuum atmosphere and independently from its position in the joint. The black sample, i.e. 16B in *Figure 4.13 b)* showed the same elongated void roughly at the centre of the glass-ceramic layer. The whole stuck to the Crofer load on top due to leaked glass slurry in deposition, and during the attempts to manually detach it the lower substrate detached. There is no reason to believe the interface was weak to begin with, as the shear force applied was substantial. With this array of samples, the using of vacuum atmosphere and intermediate dwelling heating were abandoned, since it did not resolve the porosity coalescence problem and increased the detachment rate of Crofer substrates.

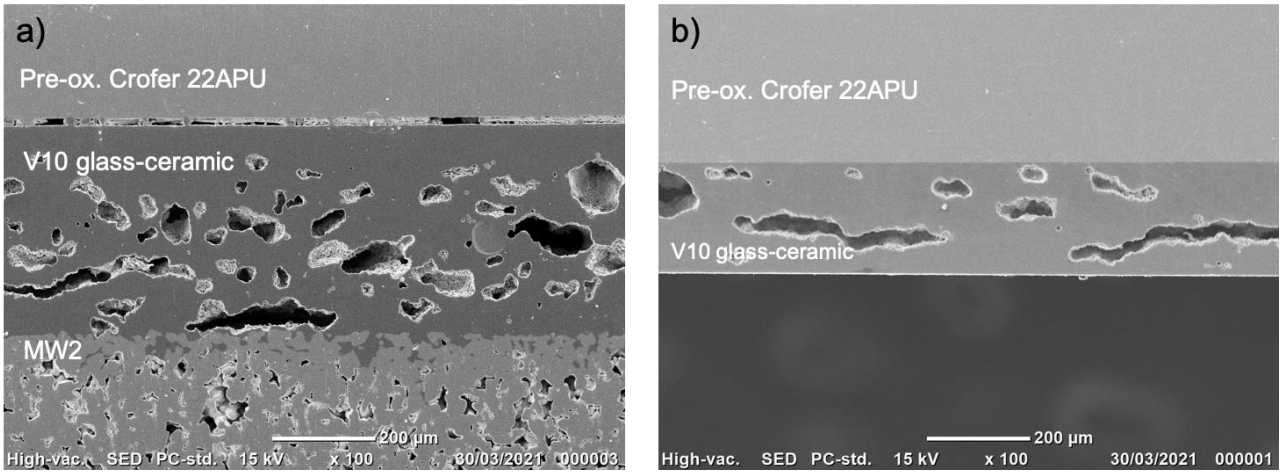

Figure 4.13:SEM images of a) sample, b) sample 16B, only top Crofer plate and glass layer are shown. Both samples were bonded with the following treatment; first dwell at 500°C for 1h then at 900°C for 1h at 5°C/min, in vacuum, under 15g weight.

Even blank joints (Crofer on Crofer) consolidated with the standard treatment (850°C, 1h, 5°C/min) in air, minus the weight, yielded practically the same results as sample 8, the reference for the setup. Excellent adhesion, small and homogeneous porosity with occasional larger void.

One last attempt with V10 glass was to precoat both substrates (sample 19), and joining them with the most successful setup, Crofer on top. Both the coatings and the joining used the same treatment in two different instances (850°C, 1h, 5°C/min) in air, with the 15g load on top. The joint resulted considerably thick, as evidenced in *Figure 4.14 a)*. Due to coating surface irregularities the slurry in the joining process left some areas unbonded. The joining glass-ceramic con be distinguished from the coating from the presence of in line pores and larger elliptical voids roughly in in the centre of the joint. In *Figure 4.14 b)* a detail of the Crofer interface shows the good bonding, some smaller pores at the interface are event, they were not found on the previous sample with the same treatment. The foam adhesion, pore size and distribution were similar to sample 8, unlike the coating obtained at 900°C (sample 15C1), the coated MW2 of the joint presents elongated porosity at about half the thickness. Such instance is still not understood, nor is the strategy to prevent it. It seems that thickness of the slurry coating may influence its presence. With lower temperatures the porosity seems smaller and more even, with the possibility of elongated void, while by increasing the temperature the pores enlarge, get more irregular and become fewer. Clearly a balance point must be found.

Several studies indicated the development of redox reaction between glass and metal substrate, the first reduces and the latter oxidizes [77], [78]. In sessile drop studies of sodium disilicate glass in 10^{-4} Pa vacuum at 1000°C, active metals like Cr can react with Na_2O or SiO_2 of the glass melt and form Cr_2O_3, Na or SiO vapour. Such vapour can form bubbles in the glass just above the interface and occurred more readily when close to a periphery of glass drops, due to easier escape of the gas for Na_2O reduction and in more central areas for silica [77]. However, the size of such pores was much lower than the ones produced in vacuum and Ar gas shielding. The only ones comparable in size were observed in sample thermally treated in air, at atmospheric pressure. Some studies reported that in Ar atmosphere, hence in absence of O_2, water can serve as the oxidizing agent on the metal, producing metal oxide and H_2 gas [78]. When lithium-alumina-silicate glass-ceramic was used to join Ni-Cr superalloy substrates in Ar shielded atmosphere at 1000°C, large voids appeared in the bulk of the glass. Upon detecting H_2 presence, it was found that water contained in the glass oxidized the metal substrates, producing metal oxides and hydrogen. It also increased presence of interfacial porosity [78]. It is possible that the coalesced porosity under flowing Ar thermally treated samples, might be due to water molecules adsorbed on glass powder particles, that desorb and react during treatment. Since water is mainly responsible for high pores in the joint bulk, it can be supposed that the

phenomena could occur also in air at atmospheric pressure and perhaps even in vacuum. Further work on the subject is needed.

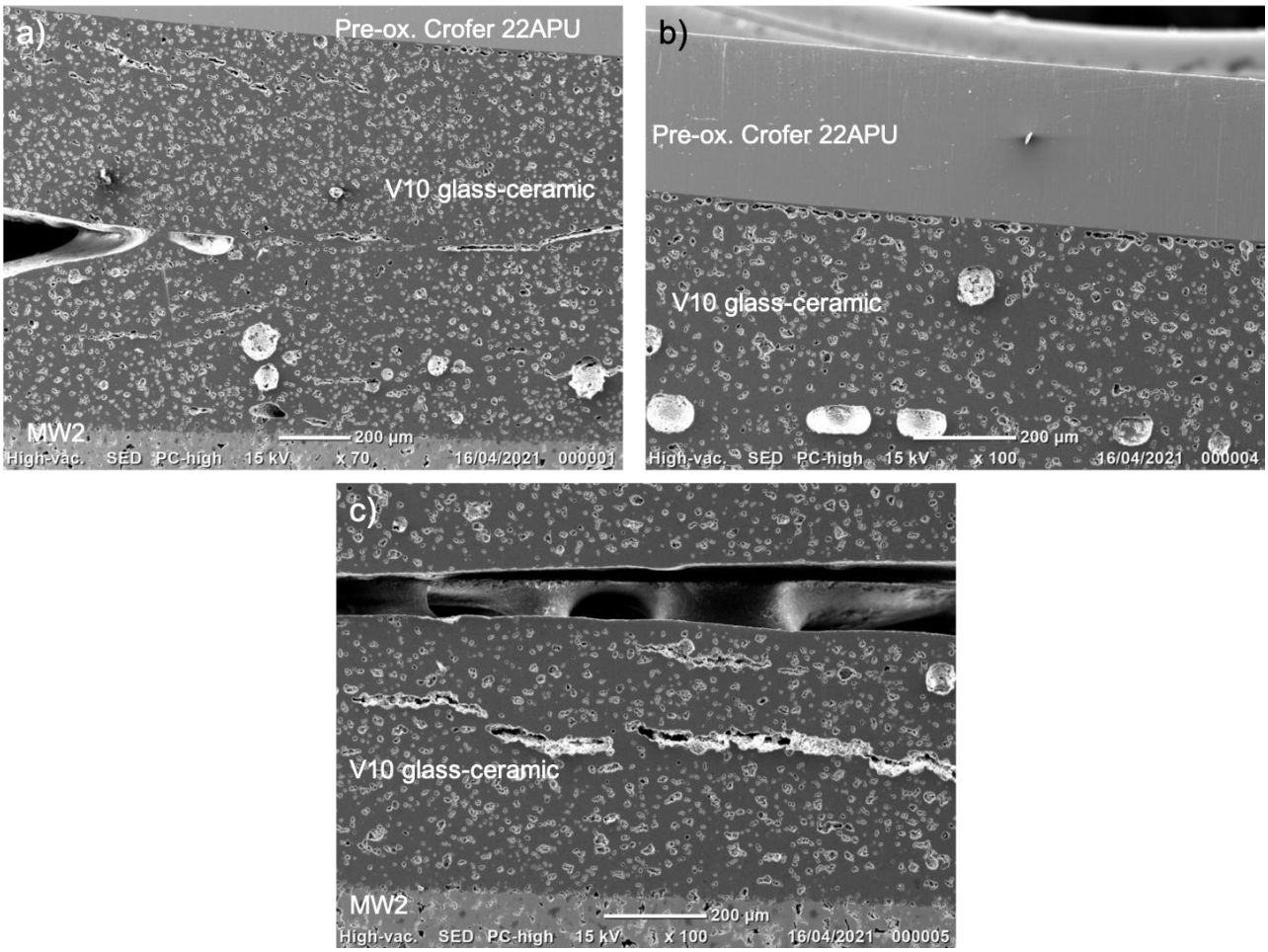

Figure 4.14: SEM images of sample 19; obtained at 850°C for 1h at 5°C/min, in air, under 15g of weight. a) joint cross-section, b) detailed view of the Crofer interface and c) of the MW2.

4.2 GC2 glass

No margin of improvement was seen with V10 glass, so a new type designated as GC2 was used to see if the excessive porosity was due to the specific type of glass. GC2 required a treatment of 950° for 1h at 5°C/min of heating and cooling to room temperature.

4.2.1 Morphological characterization

HSM test on foam allowed a more direct comparison and understanding of the two glass types behaviour seen in *Figure 4.15*. GC2 starts sintering 70°C higher than V10 but after 800°C the area drop is much greater. Assuming sintering ends at DT, GC2 sinters to a greater extent on MW2 than V10 and crystallization does not produce the increase in area featured by V10. GC2 tends to shrinkage decrease constantly as temperature increases. The morphological characterization of the cross-section of V10 and GC2 after HSM analysis revealed interesting results. The oxide layer on the foam is very evident in *Figure 4.16 b)* (N°1 *Table 4.4*). GC2 glass is less porous than V10 when compared (*Figure 4.16 a,d)* but the latter infiltrates to a greater extent. On the underside of the foam alloy a mixed V10

glass-ceramic/ iron and chromium oxide layer can be identified; proven by points N° 3 and 4 in *Figure 4.16 c)* and *Table 4.4*. A further layer consists in almost pure iron oxide (N° 2 of *Table 4.4*). The reason why such thick iron oxidation is present is not yet understood, ad it was not found in the GC2 equivalent. It is possible that such side of the alloys was mildly oxidized prior to the joining, or that suffered sufficient heating at the abrasive cutting machine due to momentary lack of cooling fluid. A closer inspection of infiltrated GC2 in *Figure 4.16 e)* revealed the presence of a novel phase. From *Table 4.4* it appears to be barium chromate ($BaCrO_4$).
Barium chromate is formed by reaction of BaO with chromia scale in presence of oxygen, or with volatile chromium species such as $CrO_2(OH)_2$[41]. It is an undesirable product for its high thermal expansion coefficient, creating a strong mismatch with the sealing glass[79]. The requirement for O_2 usually relegates its formation at the edge of the joints [41]. In this instance it was found deep in the joint. An obvious explanation comes from the fact that the MW2 alloy is porous, a greater amount of glass can come in contact with air and favour its formation even far away from the conventional edges of the joint.

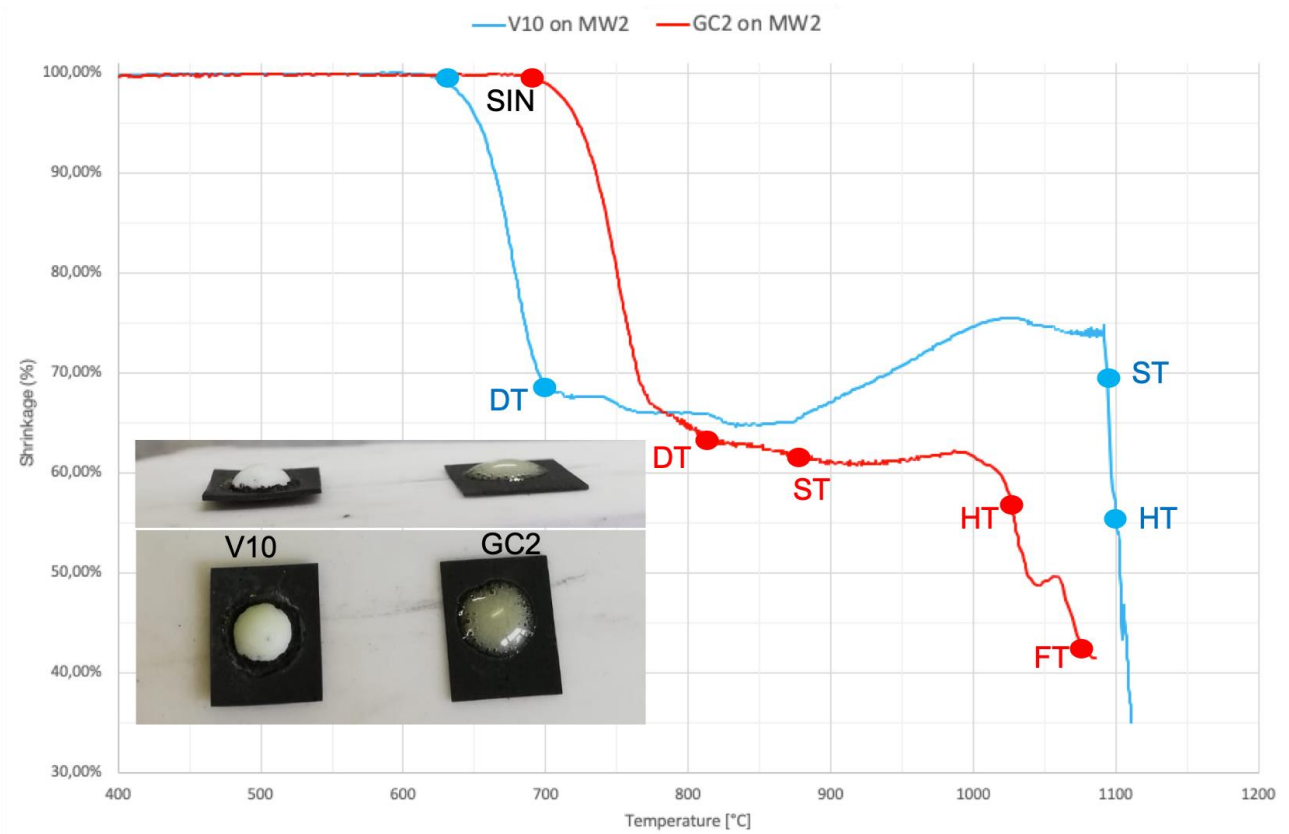

Figure 4.15: HSM curve comparison between V10 and GC2 on MW2 substrates. Bottom left: images of the samples after the measurement.

Sample 20 used the best configuration of the V10 set indicated as pre-oxidized Crofer over MW2, with the 15g weight over top. A blank sample (Crofer on Crofer without weight) was prepared and thermally treated in parallel. When compared to sample 8 (which has V10 glass as joining material), sample 20 in *Figure 4.17 a)* showed a more regular and rounded pores with the addition of larger voids at the MW2 interface. These are in between sections of effective bonding with the glass-ceramic. Sample 20B (*Figure 4.17 b)*) did not show any of these, confirming the supposition that the structure of the substrate is what induces the formation of the "pore belt". With V10 such belt was more often located at the centre of the joint, while GC2 induces its formation at the foam interface. Close ups of the foam in contact with the glass show good infiltration, up to 50µm, crystals appear as light grey needles immersed into a darker grey matrix in the top half of *Figure 4.18 a)*. The crystal

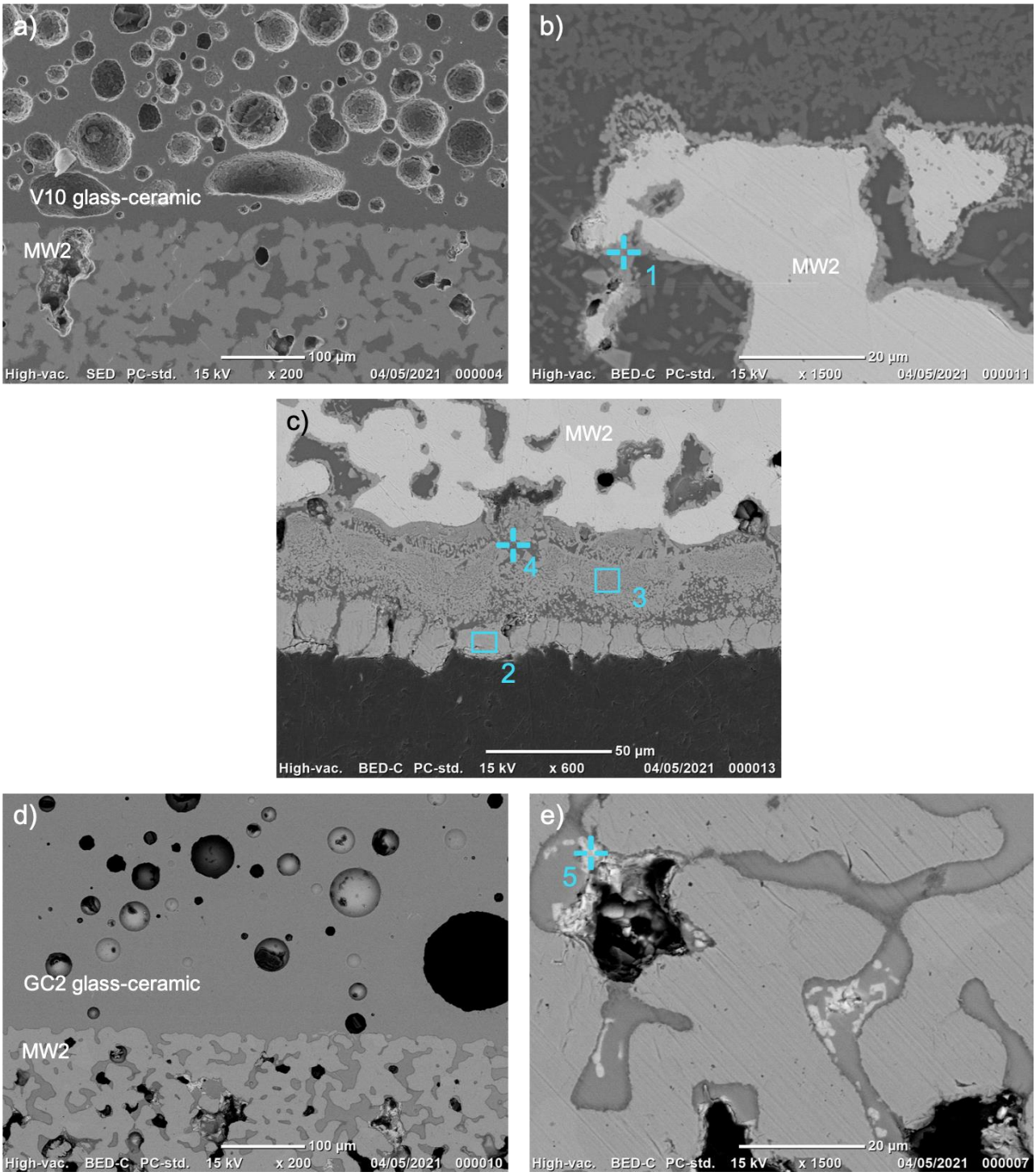

Figure 4.16:SEM images of V10 pellet on MW2, from HSM test. a) view of the interface, b,c) closu-ups of the MW2 oxide layer and bottom edge of the MW2 substrate respectively. GC2 HSM sample d) overview and e) close-up.

Table 4.4: Chemical composition of the EDS scan points/areas indicated in Figure 4.16 (% atm).

%atm	O	Na	Mg	Al	Si	Ca	Cr	Mn	Fe	Ba
N° 1	42.28	0.13	11.65	1.47	1.30	0.17	38.56	ND	4.44	/
N° 2	42.54	0.50	2.08	0.72	ND	0.33	2.35	ND	51.48	/
N° 3	43.42	2.01	1.74	2.26	4.83	0.08	22.61	0.03	23.02	/

N° 4	47.47	16.69	0.35	4.12	17.47	0.64	1.37	0.23	11.66	/
N° 5	45.21	/	/	0.68	1.12	0.08	25.70	ND	4.18	23.03

phase and matrix EDS analysis (N° 1 and 2 respectively of *Table* 4.5) have minor differences, the latter has higher Al_2O_3 and BaO concentration while lower SiO_2.

GC2 has a glass transition temperature of 677°C and a maximum crystallization temperature of 833°C, the main phase being Sanbornite ($BaSi_2O_5$) (the final CTE of the glass-ceramic is 11.4 x10^{-6} K^{-1}) as reported in [73].

In *Figure 4.18 b)* another not well-defined phase, similar in colour to the one analysed in *Figure 4.16 e)* indicated by its brighter colour, was spotted and analysed in point N° 3. It was not possible to determine with certainty the composition of such phase, given the very small size of the EDS analysis, but is very likely to be $BaCrO_4$.

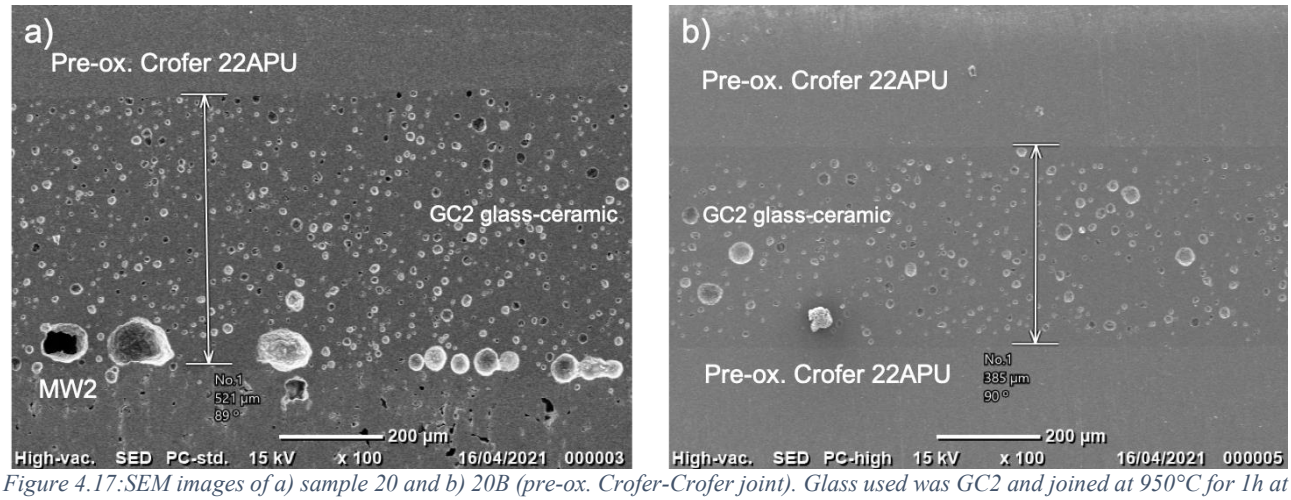

Figure 4.17:SEM images of a) sample 20 and b) 20B (pre-ox. Crofer-Crofer joint). Glass used was GC2 and joined at 950°C for 1h at 5°C/min, in air, under 15g of weight.

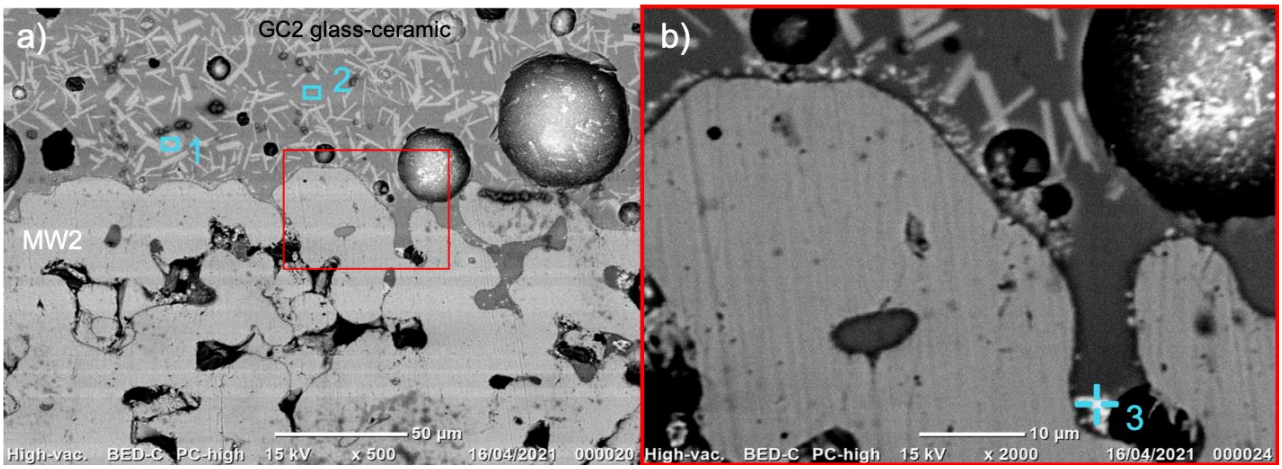

Figure 4.18:SEM images of a) sample 20's MW2-glass interface with EDS scan areas, in b) a close-up of the area in the red frame.

Table 4.5: Chemical composition of the EDS scan points/areas indicated in Figure 4.18 (% atm).

%atm	O	Al	Si	Ca	Cr	Mn	Fe	Ba
N° 1	48.69	1.67	32.06	1.15	/	/	/	16.44
N° 2	48.02	6.90	26.94	4.68	/	/	/	12.86
N° 3	53.92	3.97	17.50	2.18	7.92	0.49	2.00	12.02

As for V10 joints, final trials included varying the substrate position and atmosphere while keeping the standard GC2 joining treatment (950°C, 1h dwell, 5°C/min). Sample 21 consisted of MW2 on the top of the pre-oxidized Crofer, under load, joined in air. Sample 22 varied from n°20 just for the joining treating atmosphere, being under flowing Ar. Sample 22 had a substantial number of large voids at the interface with the porous alloy, analogously to sample 15, some more void was found also by the Crofer substrate. Overall the glass adhesion was excellent, even infiltrating the pores when the foam alloy was on top. Sample 22 evidenced greater voids distributed throughout the joint thickness, consistent infiltration up to 50µm of glass in MW2 accompanied by a dense section of glass adjacent of the foam was also noted. These evidences suggest that the Ar flux clearly influenced the infiltration and the pore formation inside the glass. Both samples had considerably thick glass-ceramic layer; as previously experienced with the V10 joints, this may play a role on horizontally developed porosity inside the joints as seen in sample 22. The distance and size of the major pores from the interfaces validates the thesis of water adsorbed glass powder particles, thus developing gas and forming pores. It is also evident when comparing the V10 glass behaviour to the GC2, that the latter has on average greater water affinity and content.

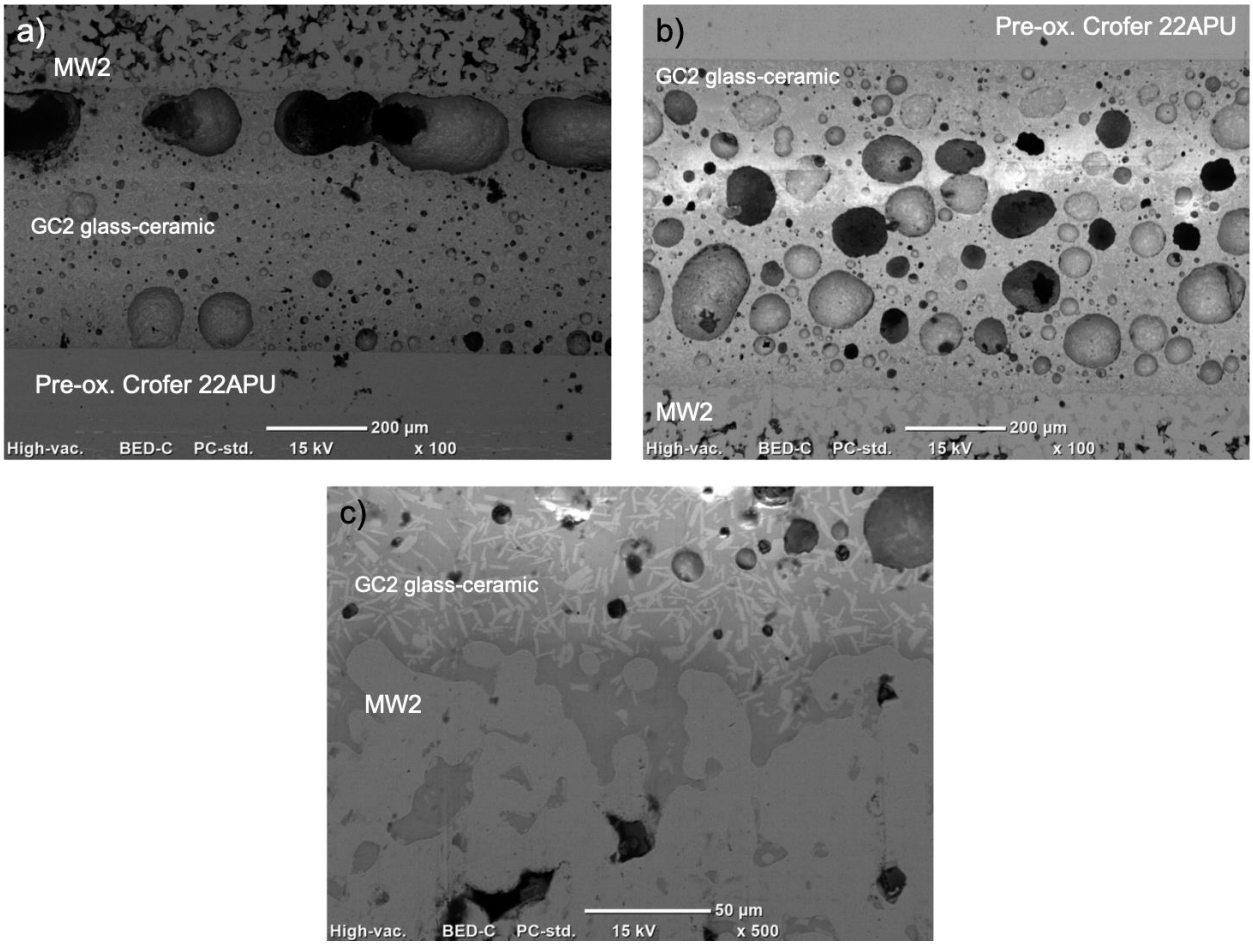

Figure 4.19: SEM images of GC2 joints. a) sample 21; MW2 on Pre-ox. Crofer bonded in air, b) sample 22 consisted of Pre-ox. Crofer on MW2 bonded in Argon, and c) MW2/glass interface close-up.
Both of the samples were joined at 950°C for 1h at 5°C/min, under 15g of weight.

Sample 20 yielded the best overall results, in term of adhesion, porosity size and distribution. While still undesired the pore coalescence is not as significant as previous samples, GC2 glass and pre-oxidized Crofer on MW2 subjected to load represent the best compromise between results obtained and complexity of joint realization. Type 20 samples were subjected to further test and analysis.

4.2.2 CT Scan

As evidenced in the previous section from the exposed surfaces, fracture occurred mostly in parts of the joint of reduced cross-sections. Such areas can be seen in a type-20 joint subjected to CT scan. *Figure 4.20 a)* shows a reconstructed model of the joint while *b)* through *d)* show the cross-section from the top (towards the foam alloy) from just above the foam, to mid-joint and in proximity of the bulk metal substrate. The higher number of voids right at the MW2 interface corresponds to the fracture areas of the tested samples. At about half the thickness a considerable size void was detected, and it was present also close to the Crofer, certainly due to trapped air during the joint assembly.

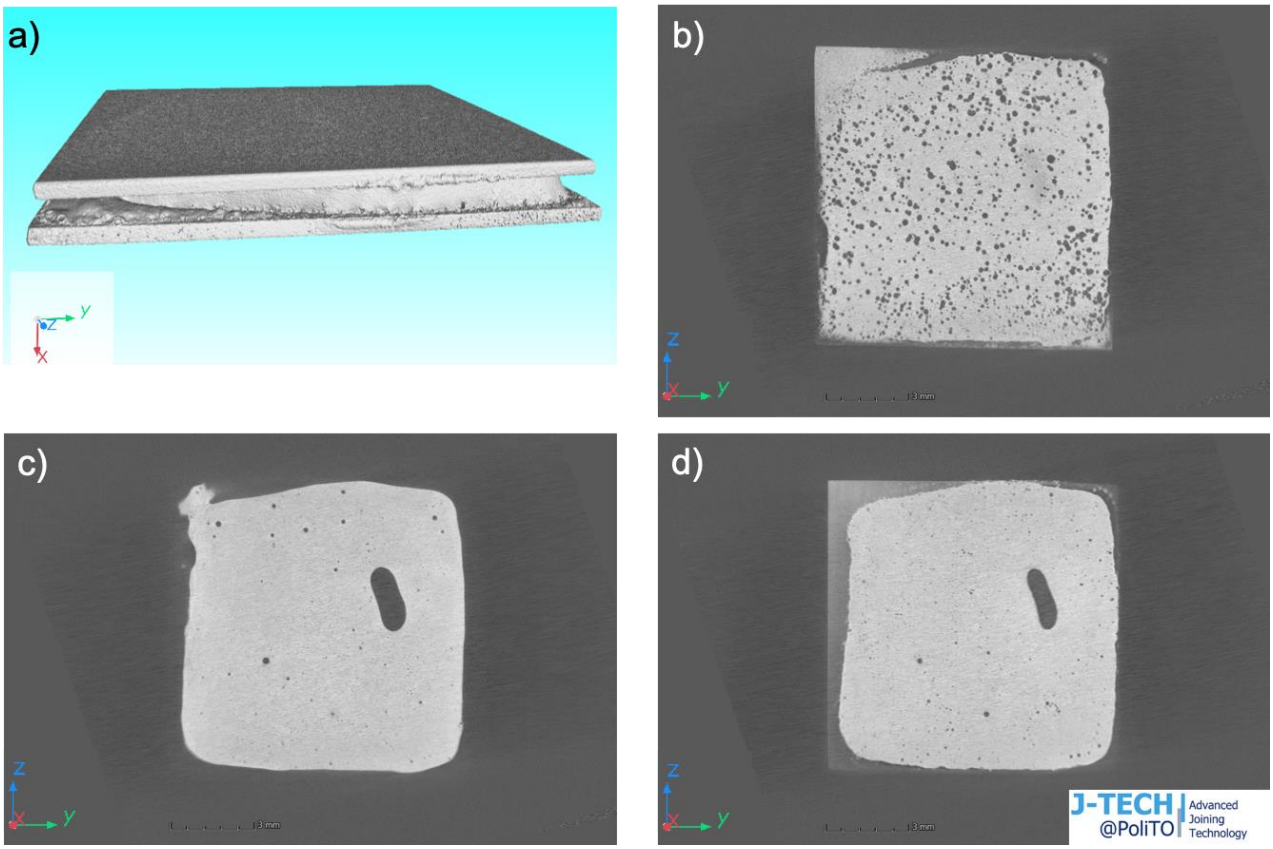

Figure 4.20: a) reconstruction of the joint, Crofer on top, b) section seen from top, the sectioning plane is located approximately just above the MW2 (0.28 mm from top surface of the MW2), c) middle of the glass ceramic layer (0.51 mm from the MW2) and c) just under the Crofer interface (0.74 mm from the MW2).

Figure 4.21 gives position and size of closed volumes identified in the joint. It was not possible to filter out the pores of the foam from the ones of the glass-ceramic due to insufficient discrimination from the machine of the glass from MW2.

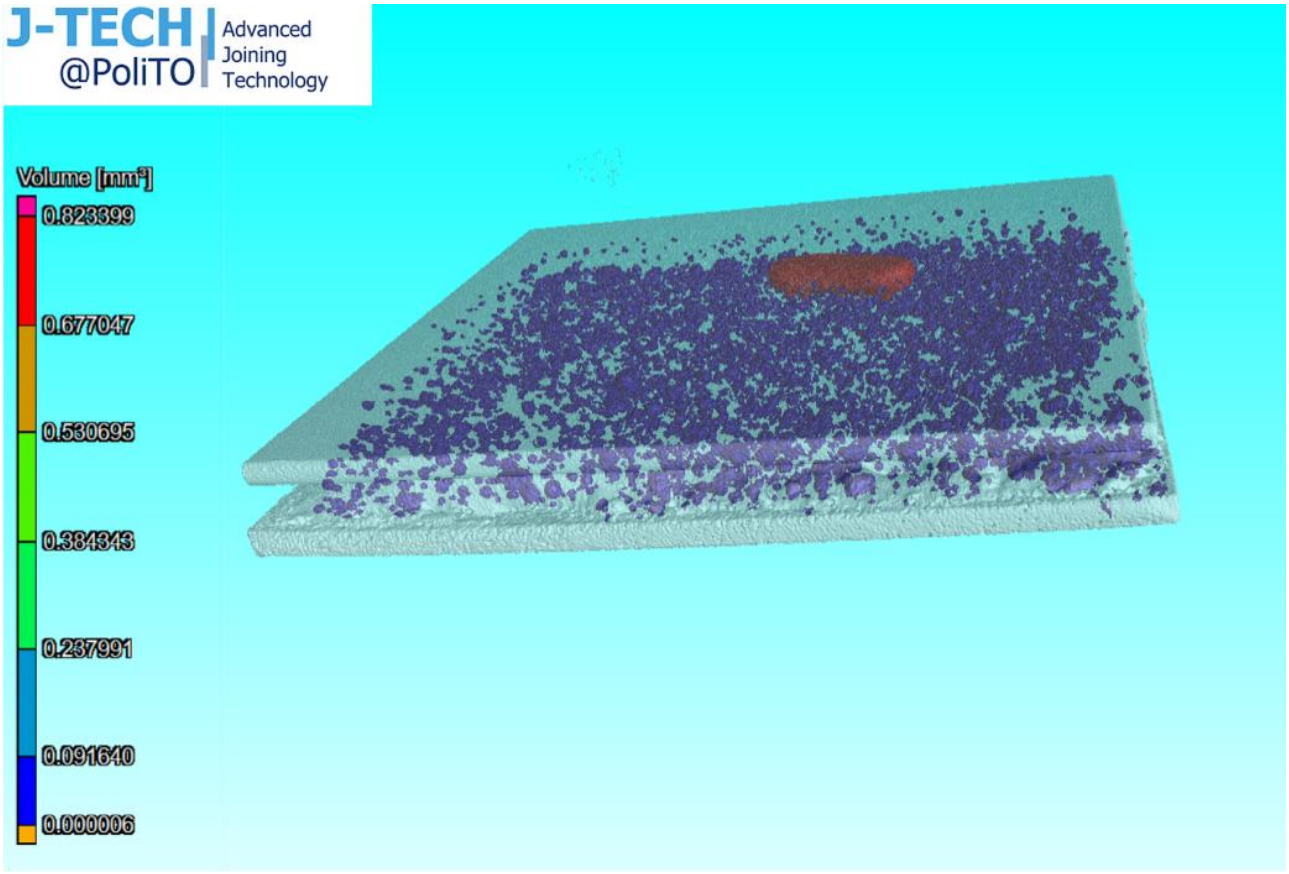

Figure 4.21: Reconstruction of the joint evidencing different sizes of closed volumes.

4.2.3 Tensile tests

A first set of three type-20 joints (pre-oxidized Crofer on MW2 and GC2 as joining glass, thermally treated at 950°C for 1h in air) were prepared and subjected to simple tensile test. The results are summarized in *Table 4.6*. After measurement of the joining area, the tensile stress was calculated with the following formula: $\sigma\ [\text{MPA}] = \frac{\text{FORCE [N]}}{\text{JOINING AREA } [mm^2]}$. None of the samples suffered detachment from the fixtures during testing.

Table 4.6: Tensile stress of GC2 Type-20 joints.

Test Sample N°	Force [N]	Joining area [mm²]	Stress- σ [MPa]
20-1	945	121.99	7.75
20-2	841	110.3208	7.62
20-3	789	114.9159	6.87

$$\sigma = 7.4 \pm 0.5\ MPa$$

From the fracture surfaces in *Figure 4.22* it can be observed that the substrates with greater contact with glass-ceramic are Crofer plates, in sample n° 20-3 almost all the glass is concentrated on the top plate.

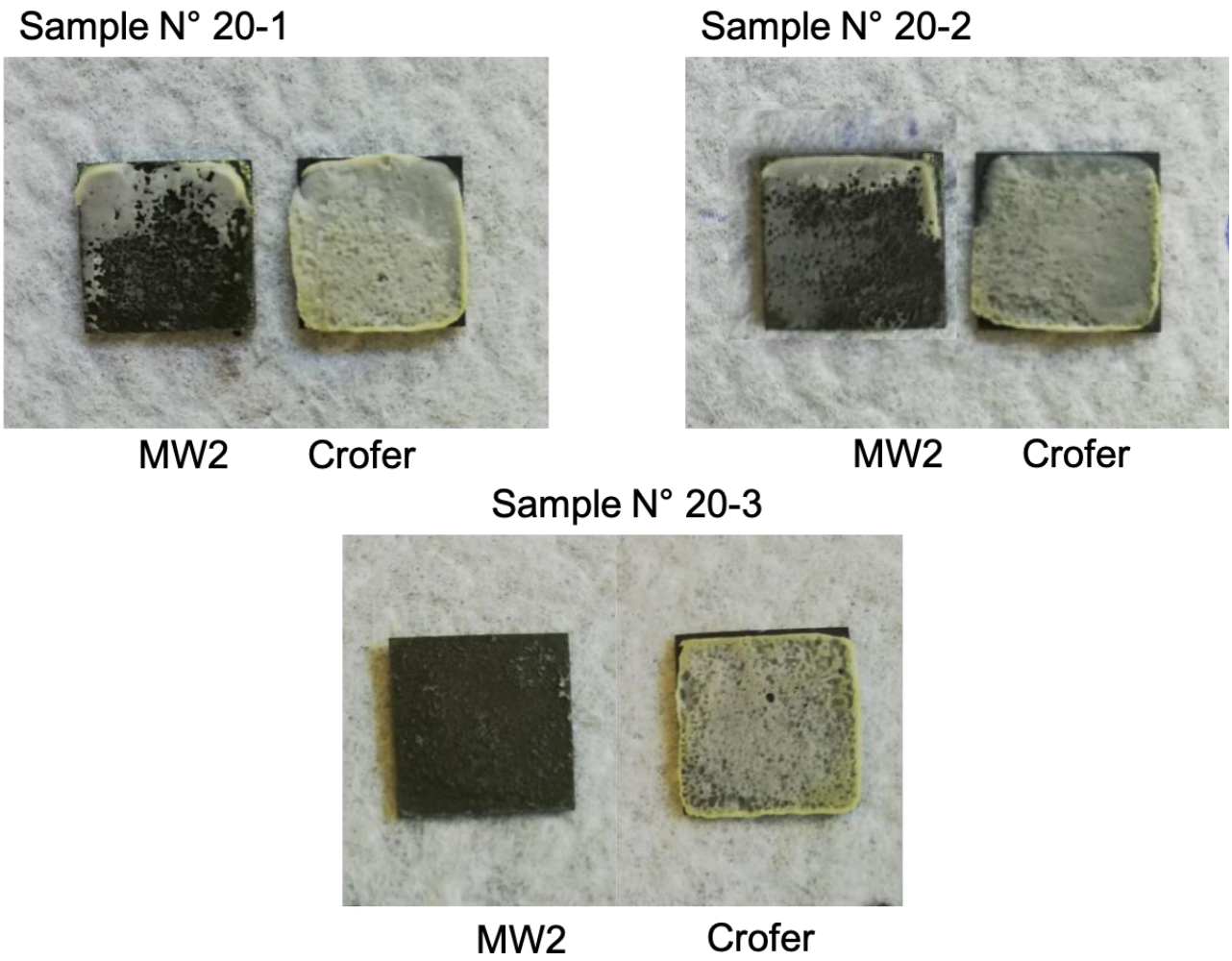

Figure 4.22:Mechanical test samples after fracture, the Crofer was placed on the top fixture, the foam on the bottom.

Since the cracks and failures happen at the sites of least resistance we can conclude that, macroscopically, it was initially supposed the MW2/glass interface to be the weakest, thus originating an adhesive fracture. For samples 20-1 and 20-2 the failure is partly cohesive and partly adhesive. The average values can be compared to the tensile strength of Crofer 22APU and H variant with a variety of glass-ceramics in the study conducted by *Greven et al*. [80]. In fact, the results are slightly higher than the majority of the sample attest at 3.80 to 6.3 MPa, only one reaches and gets above 16.7 MPa.

Widely distributed pores can be seen on each of the fracture surfaces. Post-mortem SEM analysis of the samples revealed that glass was covering the MW2 substrates, even on the outer edges as seen in *Figure 4.23 a,c)* and scan points 1, 2 of *Table 4.7*. The fracture surfaces showed small porosities (*Figure 4.23 a)* and *b)*). Unexpectedly even the areas that appeared to have exposed metal were covered with a glass-ceramic layer, proven by *Figure 4.23 d)* (point 3 in *Table 4.7*). A darker point was identified, but indicated an area were the glass was thinner hence metal underneath more easily drained surface charge. The specular fracture in *Figure 4.23 e)* surface is very small, the pores clearly disrupt its continuity. The glassy layer was found in all of the darker fracture surfaces, suggesting that the fracture happened mainly at the part of the glass ceramic with the lowest resistance, not at the foam surface but just above it, where the pores are concentrated. *Figure 4.24 a)* and *b)* of test sample 20-2 further validates the presence of glass layer even when invisible to the eye.

On the fracture surfaces of sample 20-3 a bright phase similar to the one found in *Figure 4.16 e)* was spotted. Upon analysis it was revealed to be once more $BaCrO_4$ (n°7 and 8 of *Table 4.8*) mainly

located on the Crofer side, but also on the MW2 fracture surface. Such presence may explain the lower resistance of the test sample. Such cracks could then easily propagate and bring the joint to failure during the tensile tests. Both barium chromate and concentrated pores are a detriment for the joint soundness, but it is unclear which of the two play the major role on the resistance. $BaCrO_4$ could easily form, due to the compositional and thermal conditions of the joint, hence could be an inherent flaw of the system. Further studies on the subject are needed.

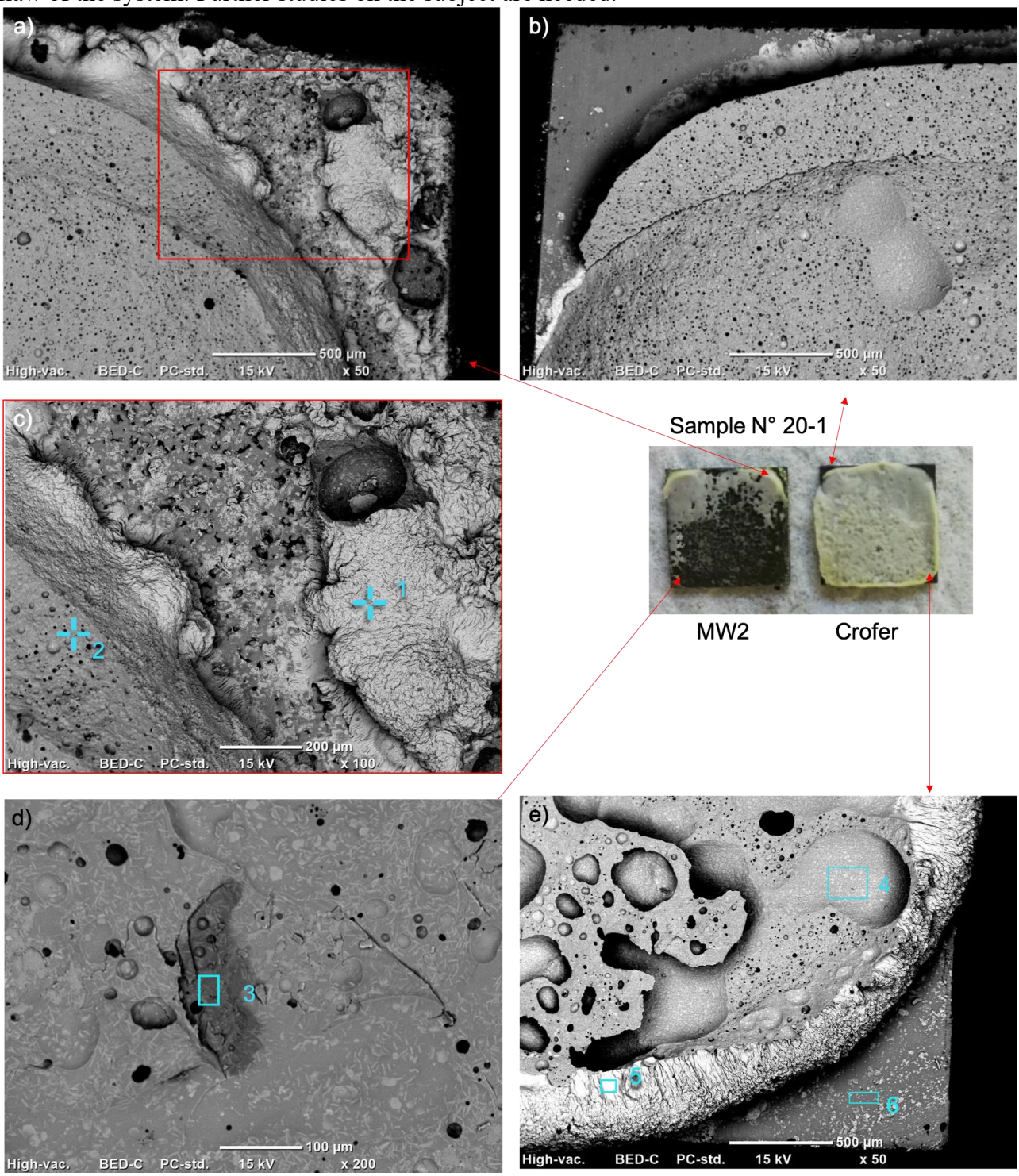

Figure 4.23:SEM images of different details of test sample 1. a) top left edge of the foam substrate and its corresponding fracture surface on the top Crofer substrate in b). c) details of the glass joining edge of figure a). d) shows an area of particularly thin glass, e) its corresponding fracture surface on Crofer.

Table 4.7: Chemical composition of the EDS scan points/areas indicated in Figure 4.23 (% atm).

%atm	O	Al	Si	Ca	Cr	Mn	Fe	Ba
N° 1	54.23	1.57	3.27	1.34	18.21	ND	ND	21.40
N° 2	66.87	4.61	18.64	2.39	/	/	/	7.48
N° 3	56.38	2.69	13.03	1.62	6.80	ND	12.57	6.91
N° 4	51.00	18.28	13.02	1.96	/	/	/	15.73
N° 5	73.65	13.60	3.20	0.86	/	/	/	8.69
N° 6	49.29	2.12	6.98	0.69	23.07	9.44	5.75	2.66

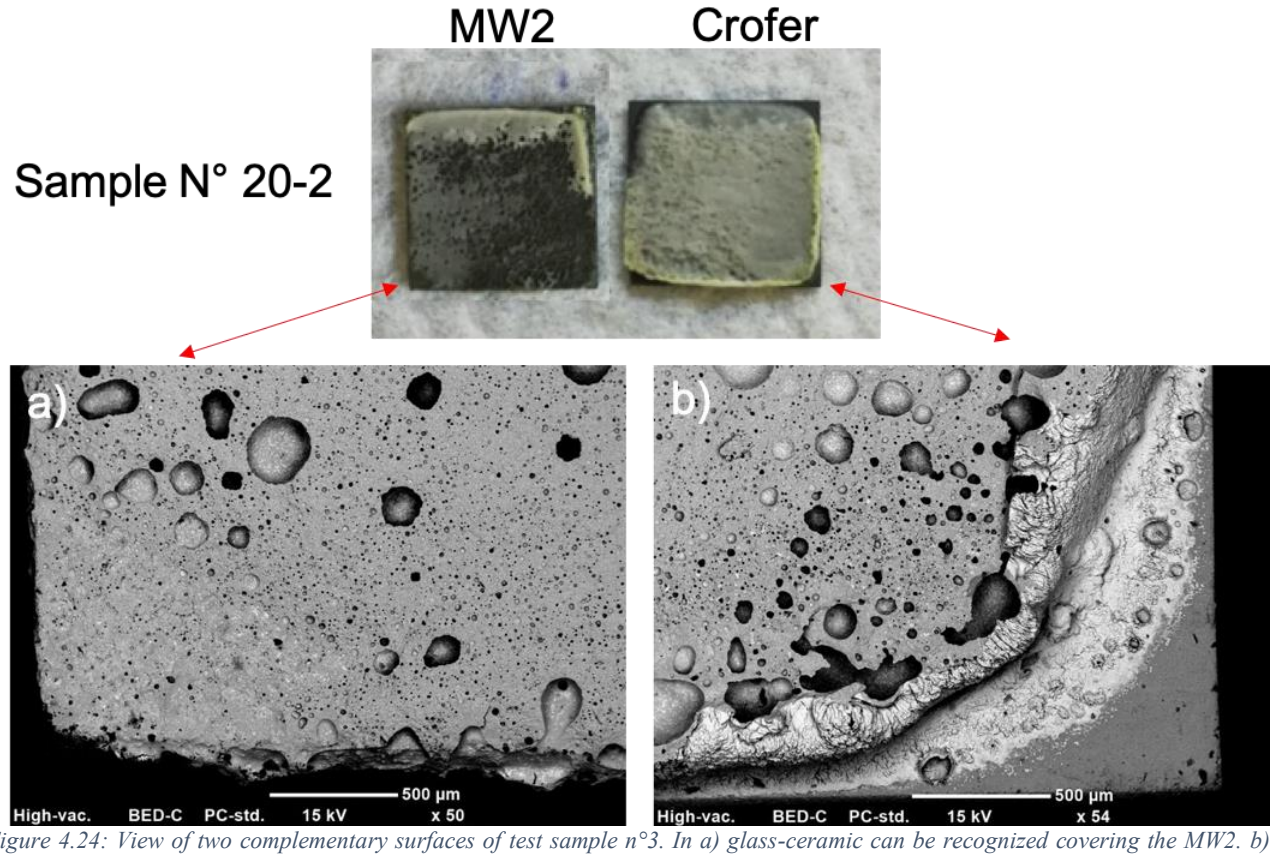

Figure 4.24: View of two complementary surfaces of test sample n°3. In a) glass-ceramic can be recognized covering the MW2. b) glass-ceramic layer on the edge of the Crofer.

A further set of three joints were prepared and was submitted to a simple thermal aging at 700°C for 500h in air. The temperature was chosen as it represents best compromise for lifetime and performance in a possible mid temperature fuel cell application. The MW2 alloy is capable of resisting for several hundred hours at 700°C without developing excessive oxide growth. According to data it is possible for the alloy to reach 1700h at the same temperature before the breakaway oxidation limit (assumed at 6% weight gain in oxide growth)[70] is reached. The temperature of 700°C proved a good challenge to the oxidation resistance of the alloy without being too extreme.

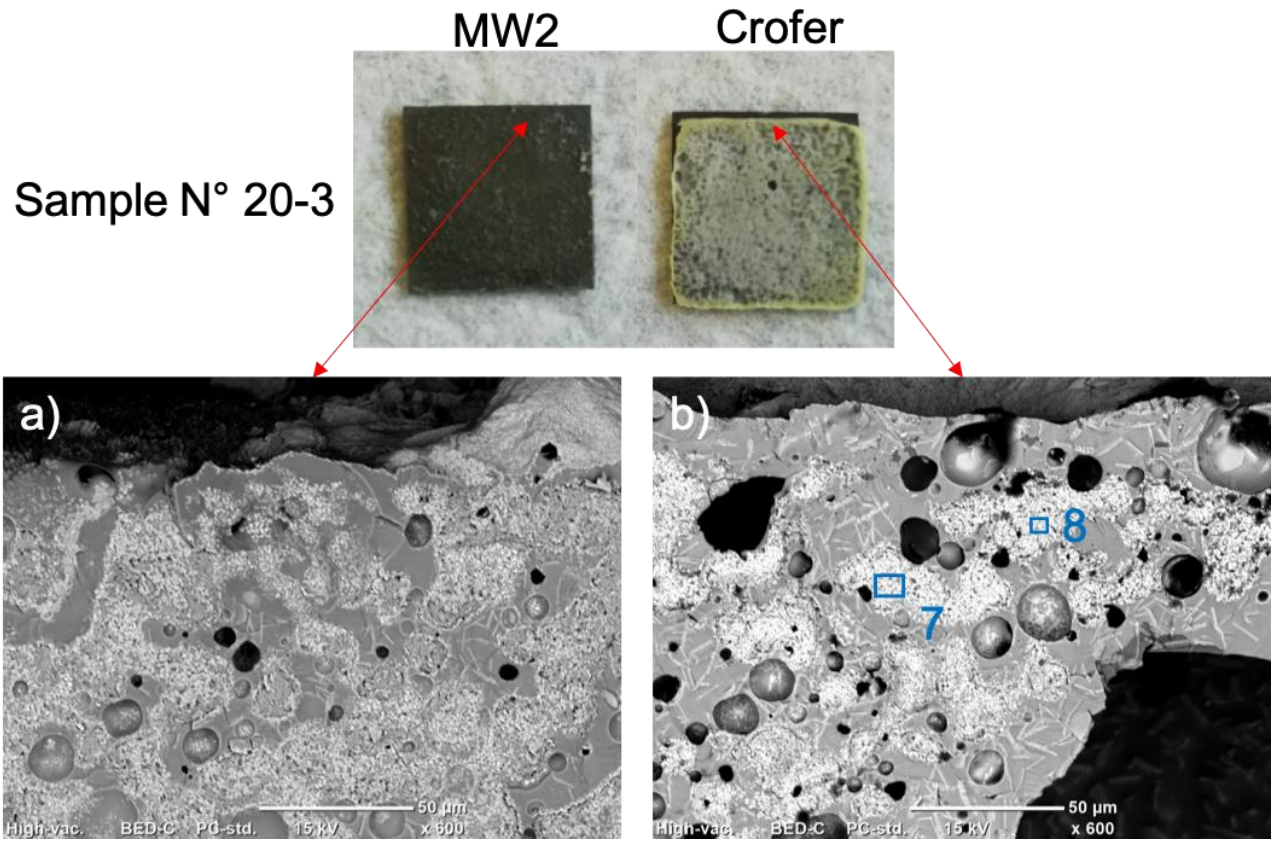

Figure 4.25: View of two complementary surfaces of test sample n°3. In a) view of the MW2 surface. b) Glass-ceramic attached to Crofer.

Table 4.8: Chemical composition of the EDS scan points/areas indicated in Figure 4.25 (% atm).

%atm	O	Al	Si	Ca	Cr	Mn	Fe	Ba
N° 7	60.42	2.32	5.71	1.70	13.76	/	/	16.09
N° 8	59.17	2.70	5.78	1.67	13.78	/	/	16.90

The results (in *Table 4.9*) showed that the aging slightly increased average resistance, but with greater minimum values. Samples 20-1A and 20-2A (in *Figure 4.26*)showed a completely adhesive fracture, while sample 30-3A was mostly adhesive with some cohesive component. It is possible that chromium can react to a greater extent, apart from oxidizing, to form barium chromate. Such compound is known to negatively impact the resistance of the joint due to the CTE mismatch, in fact sample 20-3 showed its presence and had the lower resistance of the as joined batch. With time and temperature this effect can only increase; sample 20-3A exhibited some of the lowest tensile strength. SEM and EDS analysis will be carried-out in the next future.

Table 4.9:Results of the tensile tests of the simple aging treatment.

Aging treatment (air)	Test Sample N°	Force [N]	Joining area [mm^2]	Stress- σ [MPa]	Avg. Stress + Std. Dev.
700°C, 500 h	20-1A	1247	126.560	9.85	**7.7 ± 2.9 MPa**
	20-2A	1006.7	115.260	8.73	
	20-3A	506.5	114.1465	4.44	

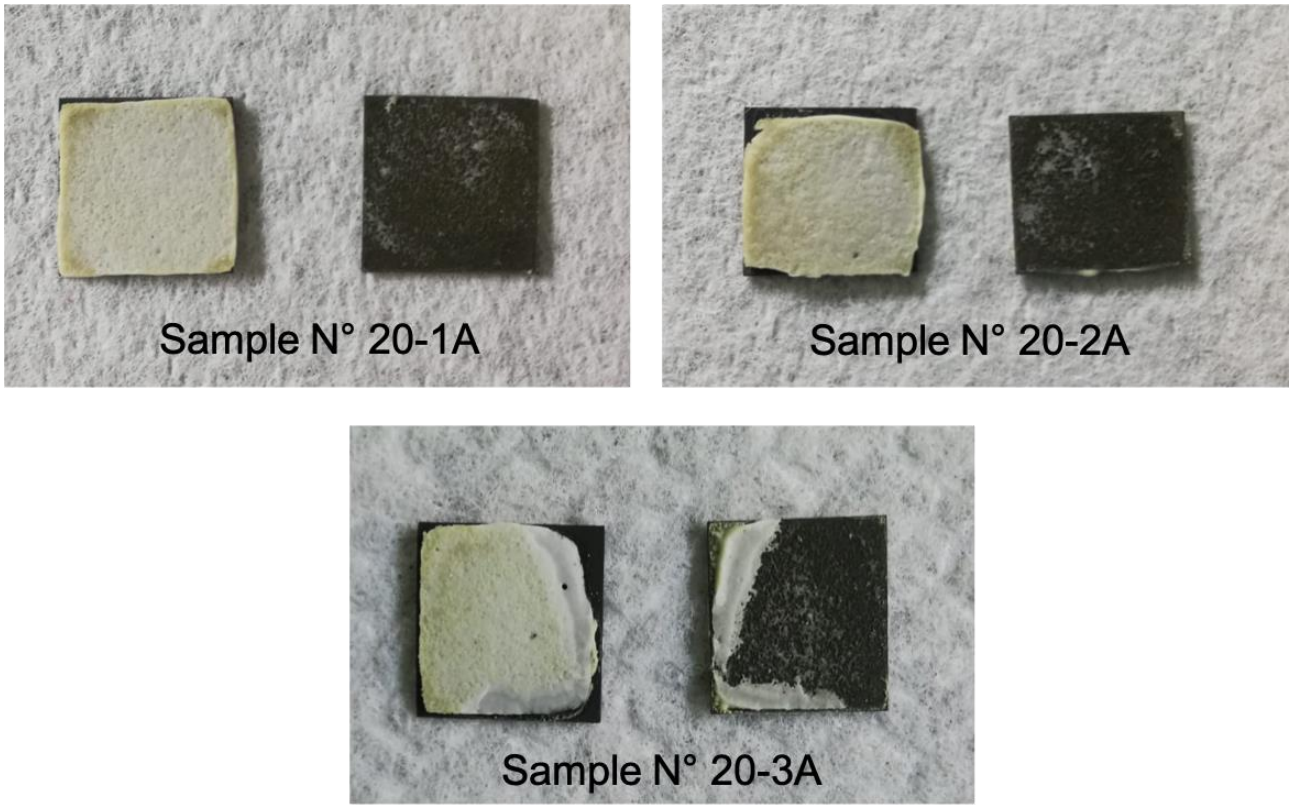

Figure 4.26: Fracture surfaces of post-aging type-20 joints.

5 Conclusions

The results can be summarized as follows:

- The first joint produced with the V10 glass exhibited insufficient bonding with the MW2. HSM studies indicated that pre-oxidation of the bulk alloy lightly improved the wetting of the substrate by the glass. For air treatments even when the Crofer was oxidized, if placed on the bottom, no good adhesion with the foam took place; the same results were obtained for the same configuration, but both alloys pre-oxidized. Reliable bonding with both substrates was achieved for a very specific set-up: pre-oxidized Crofer on top and MW2 on the bottom and 15g/cm^2 load, becoming the default configuration. Pre-coating the substrates gave unsatisfactory results and increased needlessly the complexity. A surprising fact was that, if both substrates were successfully bonded via the previously mentioned set-up, a centre-joint pore "coalescence" started to appear. It was supposed that redox reaction occurring during treatment in the glass or at the interfaces, producing gaseous species that would get trapped in the glass itself. Joining under flowing Ar did not remove the porosity, but allowed for consistent infiltration of the glass in the foam. At this point, it was thought that the gaseous species could be adsorbed on the MW2; the joint obtained with such degassed substrate yielded unsatisfactory results; the pore belt was still present. Vacuum treating only enlarged the pores and caused extensive detaching of Crofer, the reason is still unclear. It must be noted that it is surely dependent on the substrate, blank joints produced in parallel to many samples were mostly free of mid-joint voids.
  Small evenly distributed porosity was a constant in almost all of the joints, except for vacuum treatments, so air treatment was preferred especially when considering the negative impact on the tensile strength.
  A further glass containing Ba was used as joining material.

- GC2 samples in the default setup, when treated in air at 950°C for 1h at 5°C/min, resulted in a sound joint. Porosity was lower, and the infiltration on the MW2 was consistent. However larger pores appeared right at the MW2 interface, despite the excellent bonding of the glass with the alloy. According to literature, the porosity can be likely due to a reaction between adsorbed water on the glass powders with the metallic species at the interfaces, yielding metal oxides and hydrogen that accumulates forming bubbles in the glass-ceramic. Barium chromate was formed at the interface with the MW2 alloy and the glass-ceramic. Unlike other recorded examples in literature, it was found not only at the edges, but in the middle of the joint cross-section, likely due to the increased contact with oxygen in air permitted by the openings in the MW2 alloy. GC2 joint thermally treated in air, under 15g/cm^2 load, with pre-oxidized Crofer on top gave the best overall results between complexity, efficient bonding, porosity size and distribution. Despite the void at the MW2, they were considered small enough to be worth evaluating the tensile strength of the joint.
  tensile tests gave results on par with bulk-bulk joints found in literature, the glass-ceramic was mostly located at the Crofer substrate, leading to think the fracture was adhesive. On closer inspection MW2 substrates were consistently coated with glass rendering a cohesive failure.
  The aging at 700°C for 500h showed an increase of the average resistance compared to the pre-aged samples (7.7±2.9 MPa and 7.4±0.5 MPa respectively), while the minimum results were much lower. The reason may lie in the increase of the barium chromate crystal size common to the aging process, but more importantly on the thermal stresses induced by the CTE mismatch (between $BaCrO_4$ and the GC2 glass-ceramic) during the cycles. Such stresses may have caused internal cracks, that caused premature failure in testing.
  CT scan of integral test joint revealed high pore density just above the MW2 alloy suggesting that is where fracture is most likely to originate and propagate. Barium chromate was found

on the fracture surface of the least resistant joint. Further studies need to be performed to verify which are the most deleterious on the strength; the pore belt or $BaCrO_4$ formation.

The manual deposition often induced the presence of larger porosity, especially on the top of the glass-ceramic, where irregular thickness of slurry could not be evened by the force applied by the load, trapping air in the joint. More reliable, automated deposition could solve this problem. Thickness was a variable suspected to influence the formation of the mid-joint pores, to verify such suspicion a way to effectively controls the joint thickness first must be identified.
Further research should focus on determining the effect of the joining atmosphere on the interaction between glass-ceramics and perforated substrates such as MW2, particularly on ways to vent the forming gases or evaporate water when present. As for tensile strength and resistance to thermal aging, further test shall be conducted, perhaps on a greater number of samples to accurately quantify the phenomena.
The present study provides the first comprehensive assessment of joining porous to bulk alloys using glass-ceramics; it lays the groundwork for future research into MSOC development.

6 Bibliography

[1] W. Holand and G. H. Beall, *Glass-Ceramic Technology*. Newark: John Wiley & Sons, Incorporated, 2019.

[2] M. Salvo and F. Smeacetto, "Materiali Vetrosi." Dipartimento di Scienza Applicata e Tecnologia, Politecnico di Torino, Italy, 2018.

[3] A. K. Varshneya and J. C. Mauro, *Fundamentals of Inorganic Glasses*. San Diego: Elsevier, 2019.

[4] N. Russo, "' Fuel Cells and H2 Generation ,'" 2020, p. 0.

[5] S. M. Haile, "Fuel cell materials and components," *Acta Mater.*, vol. 51, no. 19, pp. 5981–6000, 2003, doi: 10.1016/j.actamat.2003.08.004.

[6] S. Hernández, "Electrocatalysis for Sustainable Energy," no. March. "catalisis per l'ambiente e l'energia" Course of study, Politecnico di Torino, 2020.

[7] M. Gödickemeier, K. Sasaki, L. J. Gauckler, and I. Riess, "Electrochemical Characteristics of Cathodes in Solid Oxide Fuel Cells Based on Ceria Electrolytes," *J. Electrochem. Soc.*, vol. 144, no. 5, pp. 1635–1646, May 1997, doi: 10.1149/1.1837653.

[8] F. Smeacetto, "Solide oxide cells materials." "Ceramici avanzati" Course of study, Politecnico di Torino, 2018.

[9] B. Timurkutluk, C. Timurkutluk, M. D. Mat, and Y. Kaplan, "A review on cell/stack designs for high performance solid oxide fuel cells," *Renew. Sustain. Energy Rev.*, vol. 56, pp. 1101–1121, 2016, doi: 10.1016/j.rser.2015.12.034.

[10] O. Yamamoto, "Solid oxide fuel cells: fundamental aspects and prospects," *Electrochim. Acta*, vol. 45, no. 15, pp. 2423–2435, 2000, doi: https://doi.org/10.1016/S0013-4686(00)00330-3.

[11] G. A. Tompsett, C. Finnerty, K. Kendall, T. Alston, and N. M. Sammes, "Novel applications for micro-SOFCs," *J. Power Sources*, vol. 86, no. 1, pp. 376–382, 2000, doi: https://doi.org/10.1016/S0378-7753(99)00418-8.

[12] J. Molenda, K. Świerczek, and W. Zajac, "Functional materials for the IT-SOFC," *J. Power Sources*, vol. 173, no. 2 SPEC. ISS., pp. 657–670, 2007, doi: 10.1016/j.jpowsour.2007.05.085.

[13] B. C. H. Steele, "Running on natural gas," *Nature*, vol. 400, no. 6745, pp. 619–621, 1999, doi: 10.1038/23144.

[14] A. Nakajo, "Thermomechanical and Electrochemical Degradation in Anode-Supported Solid Oxide Fuel Cell Stacks." Lausanne, EPFL.

[15] F. Smeacetto, "Solide oxide cells materials part 2." "Ceramici avanzati" Course of study, Politecnico di Torino, 2018, doi: 10.1149/07801.2943ecst.

[16] E. Ivers-Tiffée, A. Weber, and D. Herbstritt, "Materials and technologies for SOFC-components," *J. Eur. Ceram. Soc.*, vol. 21, no. 10, pp. 1805–1811, 2001, doi: https://doi.org/10.1016/S0955-2219(01)00120-0.

[17] Y. Arachi, H. Sakai, O. Yamamoto, Y. Takeda, and N. Imanishai, "Electrical Conductivity of the ZrO2–Ln2O3 (Ln=Lanthanides) System," *Solid State Ionics*, vol. 121, pp. 133–139, 1999, doi: 10.1016/S0167-2738(98)00540-2.

[18] A. Tschöpe, E. Sommer, and R. Birringer, "Grain size-dependent electrical conductivity of

polycrystalline cerium oxide: I. Experiments," *Solid State Ionics*, vol. 139, no. 3, pp. 255–265, 2001, doi: https://doi.org/10.1016/S0167-2738(01)00678-6.

[19] V. Thangadurai and W. Weppner, "Li6ALa2Nb2O12 (A=Ca, Sr, Ba): A New Class of Fast Lithium Ion Conductors with Garnet-Like Structure," *J. Am. Ceram. Soc.*, vol. 88, no. 2, pp. 411–418, 2005.

[20] X. Zhang *et al.*, "Interface reactions in the NiO–SDC–LSGM system," *Solid State Ionics*, vol. 133, no. 3, pp. 153–160, 2000, doi: https://doi.org/10.1016/S0167-2738(00)00744-X.

[21] H. H. Möbius, "On the history of solid electrolyte fuel cells," *J. Solid State Electrochem.*, vol. 1, no. 1, pp. 2–16, 1997, doi: 10.1007/s100080050018.

[22] S. Skinner, "Recent Advances in Perovskite-Type Materials for SOFC Cathodes," *Fuel Cells Bull.*, vol. 4, pp. 6–12, 2001, doi: 10.1016/S1464-2859(01)80254-6.

[23] S. Stølen, E. Bakken, and C. E. Mohn, "Oxygen-deficient perovskites: linking structure{,} energetics and ion transport," *Phys. Chem. Chem. Phys.*, vol. 8, no. 4, pp. 429–447, 2006, doi: 10.1039/B512271F.

[24] R. Chiba, F. Yoshimura, and Y. Sakurai, "Investigation of LaNi1-xFexO3 as a cathode material for solid oxide fuel cells," *Solid State Ionics*, vol. 124, no. 3, pp. 281–288, 1999, doi: 10.1016/S0167-2738(99)00222-2.

[25] R. Chiba, F. Yoshimura, and Y. Sakurai, "Properties of La1-ySryNi1-xFexO3 as a cathode material for a low-temperature operating SOFC," *Solid State Ionics*, vol. 152–153, pp. 575–582, 2002, doi: 10.1016/S0167-2738(02)00374-0.

[26] L.-W. Tai, M. M. Nasrallah, H. U. Anderson, D. M. Sparlin, and S. R. Sehlin, "Structure and electrical properties of La1−xSrxCo1−yFeyO3. Part 1. The system La0.8Sr0.2Co1−yFeyO3," *Solid State Ionics*, vol. 76, no. 3, pp. 259–271, 1995, doi: https://doi.org/10.1016/0167-2738(94)00244-M.

[27] S. Park, J. M. Vohs, and R. J. Gorte, "Direct oxidation of hydrocarbons in a solid-oxide fuel cell," *Nature*, vol. 404, no. 6775, pp. 265–267, 2000, doi: 10.1038/35005040.

[28] A. Atkinson *et al.*, "Advanced Anodes for High-Temperature Fuel Cells," *Nat. Mater.*, vol. 3, pp. 17–27, 2004, doi: 10.1038/nmat1040.

[29] S. Zha, Z. Cheng, and M. Liu, "Sulfur Poisoning and Regeneration of Ni-Based Anodes in Solid Oxide Fuel Cells," *J. Electrochem. Soc.*, vol. 154, no. 2, p. B201, 2007, doi: 10.1149/1.2404779.

[30] J. F. B. Rasmussen and A. Hagen, "The effect of H2S on the performance of Ni–YSZ anodes in solid oxide fuel cells," *J. Power Sources*, vol. 191, no. 2, pp. 534–541, 2009, doi: https://doi.org/10.1016/j.jpowsour.2009.02.001.

[31] M. Gong, X. Liu, J. Trembly, and C. Johnson, "Sulfur-tolerant anode materials for solid oxide fuel cell application," *J. Power Sources*, vol. 168, no. 2, pp. 289–298, 2007, doi: https://doi.org/10.1016/j.jpowsour.2007.03.026.

[32] O. A. Marina, N. L. Canfield, and J. W. Stevenson, "Thermal, electrical, and electrocatalytical properties of lanthanum-doped strontium titanate," *Solid State Ionics*, vol. 149, no. 1, pp. 21–28, 2002, doi: https://doi.org/10.1016/S0167-2738(02)00140-6.

[33] S. Zha, P. Tsang, Z. Cheng, and M. Liu, "Electrical properties and sulfur tolerance of La0.75Sr0.25Cr1−xMnxO3 under anodic conditions," *J. Solid State Chem.*, vol. 178, no. 6, pp. 1844–1850, 2005, doi: https://doi.org/10.1016/j.jssc.2005.03.027.

[34] S. Wang, M. Liu, and J. Winnick, "Stabilities and electrical conductivities of electrode

materials for use in H 2 S-containing gases," *J. Solid State Electrochem. - J SOLID STATE Electrochem*, vol. 5, pp. 188–195, 2001, doi: 10.1007/s100080000142.

[35] O. Costa-Nunes, R. J. Gorte, and J. M. Vohs, "Comparison of the performance of Cu–CeO2–YSZ and Ni–YSZ composite SOFC anodes with H2, CO, and syngas," *J. Power Sources*, vol. 141, no. 2, pp. 241–249, 2005, doi: https://doi.org/10.1016/j.jpowsour.2004.09.022.

[36] N. Mahato, A. Banerjee, A. Gupta, S. Omar, and K. Balani, "Progress in material selection for solid oxide fuel cell technology: A review," *Prog. Mater. Sci.*, vol. 72, pp. 141–337, 2015, doi: 10.1016/j.pmatsci.2015.01.001.

[37] T. Nakamura, G. Petzow, and L. J. Gauckler, "Stability of the perovskite phase LaBO3 (B = V, Cr, Mn, Fe, Co, Ni) in reducing atmosphere I. Experimental results," *Mater. Res. Bull.*, vol. 14, no. 5, pp. 649–659, 1979, doi: https://doi.org/10.1016/0025-5408(79)90048-5.

[38] T. Akashi, T. Maruyama, and T. Goto, "Transport of lanthanum ion and hole in LaCrO3 determined by electrical conductivity measurements," *Solid State Ionics*, vol. 164, no. 3, pp. 177–183, 2003, doi: https://doi.org/10.1016/j.ssi.2003.08.050.

[39] J. W. Patrick, "Handbook of fuel cells. Fundamentals technology and applications: Wolf Vielstich, Arnold Lamm, Hubert A. Gasteiger (Eds.); John Wiley and Sons Ltd, Chichester, England, 2003, Vols 1–4, 449 pages (vol. 1), 783 pages (vol. 2), 1372 pages (vols 3 and 4), ISB," *Fuel*, vol. 83, no. 4, p. 623, 2004, doi: https://doi.org/10.1016/j.fuel.2003.09.012.

[40] J. W. Fergus, "Lanthanum chromite-based materials for solid oxide fuel cell interconnects," *Solid State Ionics*, vol. 171, no. 1, pp. 1–15, 2004, doi: https://doi.org/10.1016/j.ssi.2004.04.010.

[41] Z. Yang, K. S. Weil, D. M. Paxton, and J. W. Stevenson, "Selection and Evaluation of Heat-Resistant Alloys for SOFC Interconnect Applications," *J. Electrochem. Soc.*, vol. 150, no. 9, p. A1188, 2003, doi: 10.1149/1.1595659.

[42] *Superalloys II / ed. by Chester T. Sims, Norman S. Stoloff, William C. Hagel*. New York: Wiley, 1987.

[43] P. Kofstad and R. Bredesen, "High temperature corrosion in SOFC environments," *Solid State Ionics*, vol. 52, no. 1, pp. 69–75, 1992, doi: https://doi.org/10.1016/0167-2738(92)90092-4.

[44] A. Holt and P. Kofstad, "Electrical conductivity and defect structure of Cr2O3. I. High temperatures (>∼1000°C)," *Solid State Ionics*, vol. 69, no. 2, pp. 127–136, 1994, doi: https://doi.org/10.1016/0167-2738(94)90401-4.

[45] F. Smeacetto, "Glass ceramics for energy conversion devices." "Ceramici avanzati" Course of study, Politecnico di Torino, 2018.

[46] W. J. Quadakkers, H. Greiner, M. Hänsel, A. Pattanaik, A. S. Khanna, and W. Malléner, "Compatibility of perovskite contact layers between cathode and metallic interconnector plates of SOFCs," *Solid State Ionics*, vol. 91, no. 1, pp. 55–67, 1996, doi: https://doi.org/10.1016/S0167-2738(96)00425-0.

[47] S. Taniguchi *et al.*, "Degradation phenomena in the cathode of a solid oxide fuel cell with an alloy separator," *J. Power Sources*, vol. 55, no. 1, pp. 73–79, 1995, doi: 10.1016/0378-7753(94)02172-Y.

[48] Y. Larring and T. Norby, "Spinel and Perovskite Functional Layers Between Plansee Metallic Interconnect (Cr-5 wt {\%} Fe-1 wt {\%} Y[sub 2]O[sub 3]) and Ceramic (La[sub 0.85]Sr[sub 0.15])[sub 0.91]{MnO}[sub 3] Cathode Materials for Solid Oxide Fuel Cells," *J. Electrochem. Soc.*, vol. 147, no. 9, p. 3251, 2000, doi: 10.1149/1.1393891.

[49] X. Chen, P. Y. Hou, C. P. Jacobson, S. J. Visco, and L. C. De Jonghe, "Protective coating on stainless steel interconnect for SOFCs: oxidation kinetics and electrical properties," *Solid State Ionics*, vol. 176, no. 5, pp. 425–433, 2005, doi: https://doi.org/10.1016/j.ssi.2004.10.004.

[50] Z. Yang, G.-G. Xia, G. D. Maupin, and J. W. Stevenson, "Conductive protection layers on oxidation resistant alloys for SOFC interconnect applications," *Surf. Coatings Technol.*, vol. 201, no. 7, pp. 4476–4483, 2006, doi: https://doi.org/10.1016/j.surfcoat.2006.08.082.

[51] R. N. Singh, "Sealing Technology for Solid Oxide Fuel Cells (SOFC)," *Int. J. Appl. Ceram. Technol.*, vol. 4, no. 2, pp. 134–144, 2007, doi: https://doi.org/10.1111/j.1744-7402.2007.02128.x.

[52] Y.-S. Chou and J. Stevenson, "Novel Silver/Mica Multilayer Compressive Seals for Solid-Oxide Fuel Cells: The Effect of Thermal Cycling and Material Degradation on Leak Behavior," *J. Mater. Res.*, vol. 18, pp. 2243–2250, 2003, doi: 10.1557/JMR.2003.0313.

[53] Y. Chou, J. W. Stevenson, and L. A. Chick, "Novel Compressive Mica Seals with Metallic Interlayers for Solid Oxide Fuel Cell Applications," *J. Am. Ceram. Soc.*, vol. 86, no. 6, pp. 1003–1007, 2003.

[54] Y. Chou and J. W. Stevenson, "Thermal cycling and degradation mechanisms of compressive mica-based seals for solid oxide fuel cells," *J. Power Sources*, vol. 112, no. 2, pp. 376–383, 2002, doi: https://doi.org/10.1016/S0378-7753(02)00444-5.

[55] J. W. Fergus, "Sealants for solid oxide fuel cells," *J. Power Sources*, vol. 147, no. 1, pp. 46–57, 2005, doi: https://doi.org/10.1016/j.jpowsour.2005.05.002.

[56] N. Minh and T. T. Takahashi, "Science and Technology of Ceramic Fuel Cell," *Amsterdam: Elsevier*, vol. 9, 1995, doi: 10.1016/B978-044489568-4/50002-5.

[57] M. C. Tucker, "Progress in metal-supported solid oxide fuel cells: A review," *J. Power Sources*, vol. 195, no. 15, pp. 4570–4582, 2010, doi: 10.1016/j.jpowsour.2010.02.035.

[58] D. Udomsilp *et al.*, "Metal-Supported Solid Oxide Fuel Cells with Exceptionally High Power Density for Range Extender Systems," *Cell Reports Phys. Sci.*, vol. 1, no. 6, 2020, doi: 10.1016/j.xcrp.2020.100072.

[59] A. HOLT and P. KOFSTAD, "Electrical conductivity and defect structure of Cr2O3. II: Reduced temperatures (< ~ 1000°C)," *Solid state ionics*, vol. 69, no. 2, pp. 137–143, 1994, doi: 10.1016/0167-2738(94)90402-2.

[60] Y.-W. Ju, H. Eto, T. Inagaki, and T. Ishihara, "High Power SOFC Using LSGM Film on NiFe Porous Bi-metal Substrate," in *ECS transactions*, 2019, vol. 25, no. 2, pp. 719–726.

[61] H. Kurokawa, K. Kawamura, and T. Maruyama, "Oxidation Behavior of Fe-16Cr Alloy Interconnect for SOFC Under Hydrogen Potential Gradient," *Solid State Ionics*, vol. 168, pp. 13–21, Mar. 2004, doi: 10.1016/j.ssi.2004.02.008.

[62] V. V. Krishnan, "Recent developments in metal-supported solid oxide fuel cells," *Wiley Interdiscip. Rev. Energy Environ.*, vol. 6, no. 5, 2017, doi: 10.1002/wene.246.

[63] P. Bance, N. P. Brandon, B. Girvan, P. Holbeche, S. O'Dea, and B. C. H. Steele, "Spinning-out a fuel cell company from a UK University—2 years of progress at Ceres Power," *J. Power Sources*, vol. 131, pp. 86–90, May 2004, doi: 10.1016/j.jpowsour.2003.11.077.

[64] M. C. Tucker, "Durability of symmetric-structured metal-supported solid oxide fuel cells," *J. Power Sources*, vol. 369, pp. 6–12, 2017, doi: 10.1016/j.jpowsour.2017.09.075.

[65] S. M. Gross, T. Koppitz, J. Remmel, J. B. Bouche, and U. Reisgen, "Joining properties of a

composite glass-ceramic sealant," *Fuel Cells Bull.*, vol. 2006, no. 9, pp. 12–15, 2006, doi: 10.1016/S1464-2859(06)71320-7.

[66] W. Zhu, J. Chen, C. Jiang, C. Hao, and J. Zhang, "Joining of porous alumina with a CaO-Al2O3-SiO 2 glass-ceramic," *J. Am. Ceram. Soc.*, vol. 96, no. 6, pp. 1738–1744, 2013, doi: 10.1111/jace.12310.

[67] L. Li, L. Sun, C. Liu, X. Wang, X. Wang, and J. Zhang, "Microstructure and properties of porous Si3N4/dense Si3N4 joints bonded using RE–Si–Al–O–N (RE = Y or Yb) glasses," *Metals (Basel).*, vol. 7, no. 11, pp. 3–11, 2017, doi: 10.3390/met7110500.

[68] L. Sun, C. Liu, S. Guo, J. Fang, D. Wang, and J. Zhang, "Wetting and joining of porous Si3N4 and dense Si3N4 ceramics with in-situ formed β-spodumene/spinel glass-ceramic interlayer," *Appl. Surf. Sci.*, vol. 517, no. 92, p. 146178, 2020, doi: 10.1016/j.apsusc.2020.146178.

[69] J. Fang, L. Sun, Q. Qi, J. Zhang, and C. Liu, "Microstructure evolution and mechanical properties of porous Si3N4 and dense Si3N4 joints bonded using CaO–Li2O-Al2O3–SiO2 glass-ceramic," *J. Eur. Ceram. Soc.*, vol. 39, no. 15, pp. 4545–4553, 2019, doi: 10.1016/j.jeurceramsoc.2019.07.006.

[70] D. Koszelow, M. G. Makowska, F. Marone, J. Karczewski, P. Jasinski, and S. Molin, "Corrosion Science High temperature corrosion evaluation and lifetime prediction of porous Fe22Cr stainless steel in air in temperature range 700-900 ° C."

[71] N. J. Magdefrau, L. Chen, E. Y. Sun, and M. Aindow, "Effects of alloy heat treatment on oxidation kinetics and scale morphology for crofer 22 APU," *J. Power Sources*, vol. 241, pp. 756–767, 2013, doi: 10.1016/j.jpowsour.2013.03.181.

[72] A. G. Sabato *et al.*, "Effect of electric load and dual atmosphere on the properties of an alkali containing diopside-based glass sealant for solid oxide cells," *J. Power Sources*, vol. 415, no. October 2018, pp. 15–24, 2019, doi: 10.1016/j.jpowsour.2019.01.051.

[73] M. Ferraris *et al.*, "Torsional shear strength behavior of advanced glass-ceramic sealants for SOFC/SOEC applications," *J. Eur. Ceram. Soc.*, vol. 40, no. 12, pp. 4067–4075, 2020, doi: 10.1016/j.jeurceramsoc.2020.04.034.

[74] F. Baino and C. Vitale-Brovarone, "Wollastonite-containing bioceramic coatings on alumina substrates: Design considerations and mechanical modelling," *Ceram. Int.*, vol. 41, no. 9, pp. 11464–11470, 2015, doi: 10.1016/j.ceramint.2015.05.111.

[75] S. Tecnica, "Araldite ® 2015," no. April 2007, pp. 1–6, 2015.

[76] G. Molino, "Laboratorio ingegneria dei materiali microtomografia computerizzata." 2020.

[77] A. P. Tomsia, Z. Feipeng, and J. A. Pask, "Reactions and Bonding of Sodium Disilicate Glass with Chromium," Berkeley, California 94720, 1985.

[78] L. D. Haws, D. P. Kramer, W. E. Moddeman, G. W. Wooten, and M. Research Corporation, "High Strength Glass-Ceramic to Metal Seals," MOUND Miannisbung, Ohio ^45342, 1986.

[79] C. W. P. T. PISTORIUS and M. C. PISTORIUS, "Lattice constants and thermal-expansion properties of the Chromates and selenates of lead, strontium and barium:," *Zeitschrift für Krist. - Cryst. Mater.*, vol. 117, no. 1–6, pp. 259–272, 1962, doi: doi:10.1524/zkri.1962.117.16.259.

[80] B. Cela Greven *et al.*, "Torsional shear strength of novel glass-ceramic composite sealants for solid oxide fuel cell stacks," *Int. J. Appl. Ceram. Technol.*, vol. 15, no. 2, pp. 286–295, 2018, doi: 10.1111/ijac.12819.